AFWAL-TR-80-4003

ADA086852

LEVEL

⑥

VIBRATIONS OF A COMPRESSOR BLADE WITH SLIP
AT THE ROOT.

⑩

David I. G. Jones

Metals Behavior Branch
Metals and Ceramics Division

DTIC
SELECTE D
JUL 1 8 1980
C

⑫ 144

⑪ April 80

⑭

TECHNICAL REPORT AFWAL-TR-80-4003

⑨ Final Report, Nov 75 - Jun 79

Approved for public release; distribution unlimited.

⑯ 2418 ⑰ 03

MATERIALS LABORATORY
AIR FORCE WRIGHT AERONAUTICAL LABORATORIES
AIR FORCE SYSTEMS COMMAND
WRIGHT-PATTERSON AIR FORCE BASE, OHIO 45433

392662

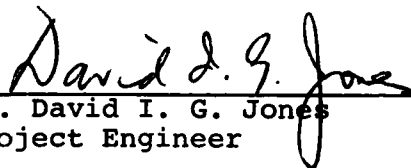80 7 16 037
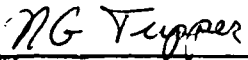
This technical report has been reviewed and is approved for publication.

Dr. David I. G. Jones
Project Engineer

FOR THE COMMANDER

NATHAN G. TUPPER
Chief, Metals Behavior Branch
Metals and Ceramics Division

REPORT DOCUMENTATION PAGE	READ INSTRUCTIONS BEFORE COMPLETING FORM
1. REPORT NUMBER AFWAL-TR-80-4003	2. GOVT ACCESSION NO. *AD-A086 852*	3. RECIPIENT'S CATALOG NUMBER N.A.

4. TITLE (and Subtitle) VIBRATIONS OF A COMPRESSOR BLADE WITH SLIP AT THE ROOT	5. TYPE OF REPORT & PERIOD COVERED TR Nov 1975 - June 1979
	6. PERFORMING ORG. REPORT NUMBER

7. AUTHOR(s) DAVID I. G. JONES	8. CONTRACT OR GRANT NUMBER(s)

9. PERFORMING ORGANIZATION NAME AND ADDRESS Materials Laboratory (AFML/LLN) Air Force Wright Aeronautical Laboratories Air Force Systems Command Wright-Patterson AFB, Ohio 45433	10. PROGRAM ELEMENT, PROJECT, TASK AREA & WORK UNIT NUMBERS 62102F 2418 24180302

11. CONTROLLING OFFICE NAME AND ADDRESS Materials Laboratory Air Force Systems Command Wright-Patterson AFB, Ohio 45433	12. REPORT DATE April 1980
	13. NUMBER OF PAGES 144

14. MONITORING AGENCY NAME & ADDRESS(if different from Controlling Office)	15. SECURITY CLASS. (of this report) Unclassified
	15a. DECLASSIFICATION DOWNGRADING SCHEDULE

16. DISTRIBUTION STATEMENT (of this Report)

Approved for public release; distribution unlimited.

17. DISTRIBUTION STATEMENT (of the abstract entered in Block 20, if different from Report)

18. SUPPLEMENTARY NOTES

19. KEY WORDS (Continue on reverse side if necessary and identify by block number)

Turbine blades	Damping
Compressor blades	Vibrations
Modelization	
Slip	

20. ABSTRACT (Continue on reverse side if necessary and identify by block number)

A simple discrete analytical model is developed to represent the vibration response behavior of a jet engine compressor or turbine blade, primarily in the fundamental mode, allowing for slip at the root. The analysis is compared with experiment, and agreement is found to be satisfactory, indicating that some of the phenomena involved can be modeled in a simple way.

DD FORM 1473 1 JAN 73   EDITION OF 1 NOV 65 IS OBSOLETE

FOREWORD

This report was prepared by the Metals and Ceramics Division, Materials Laboratory, Air Force Wright Aeronautical Laboratories, Air Force Systems Command, under Project No. 2418, "Metallic Materials," Task No. 241803, "Behavior of Metals". The research was conducted by Dr. David I. G. Jones, Materials Laboratory (AFWAL/MLLN) and Dr. hab. Agnieszka Muszyńska, Institute of Fundamental Technological Research, Polish Academy of Sciences, Warsaw, Poland, in part while both authors were at Institut National des Sciences Appliquees, Lyon, France, during the period November 1975 to August 1976. The subject of turbine and compressor blade vibration prediction and control is of great importance to the United States Air Force, and it is for this reason that a complete review of the work accomplished has been prepared. The report was typed by Judy Mann and Kathy Lee Fox.

This report covers work conducted during the period November 1975 to June 1979.

TABLE OF CONTENTS

TABLE OF CONTENTS (CONCLUDED)

LIST OF ILLUSTRATIONS

LIST OF ILLUSTRATIONS (CONTINUED)

LIST OF ILLUSTRATIONS (CONTINUED)

LIST OF ILLUSTRATIONS (CONTINUED)

LIST OF ILLUSTRATIONS (CONTINUED)

LIST OF ILLUSTRATIONS (CONCLUDED)

LIST OF TABLES

NOMENCLATURE

A	Amplitude of the response
A	Amplitude of response of mass m_2
A_{II}	Amplitude of response of mass m_3
A_D	Cross section area of blade between root mating surfaces and platform
a_m	m th Fourier coefficient of excitation force
b_p	Breadth of platform
$C(A)$, $C^*(A)$	Functions of gap
$\cos \alpha$	Direction cosine
D, D_{II}	Amplitude of response of mass m_1 (tip of blade)
D^*, D^*_{II}	Amplitude of response of mass m_1 (no slip)
exp	Exponential function
E	Young's modulus of blade material
f	Frequency (Hz)
F_1	Normal force at root
F_2	Frictional force at root
f_i	i th resonant frequency
h_p	Thickness of platform
h	Gap between transducer and blade
i	$\sqrt{-1}$
I_1, I_2	Moments of inertia
K_1	Modal stiffness in first mode
k_1, k_2	Stiffness
k	Effective stiffness
L	Length of blade
ℓ_D	Length of blade section between root mating surfaces and sub-platform
ℓ_P	Length of sub-platform
m_1, m_2, m_3	Masses
M_1, M_2	Masses
M	Moment
$M_1 M_2 R/k_1 =$	M
M_o	Mass at moving element of impedance head
m	Integer ($m = 1, 2, \ldots$)
n	Number of fixed vanes or mode number

NOMENCLATURE, continued

$\bar{N}$	Net normal load at dovetail mating surfaces
N_1	Net normal load at platform
R, R_1	Nondimensional coefficients
R_o	Radius of dovetail sliding surfaces relative to root rotation center
R_D	Radius of blade relative to disk axis
R	Distance between bodies M_1 and M_2
$S(t)$	Applied force vector as function of time
S	Amplitude of S
S_1, S_2	Force amplitudes
$S \cos (\omega t - \gamma)$	Exciting force
t	Time
V_s	Voltage from impedance head
V	Oscillator voltage
x, y	Coordinates in plane of blade
x_1, y_1	Point of application of $S(t)$
$x(t)$	Horizontal motion of body M_2
X_1	Displacement of mass 1. ($= \theta_1 L$)
X_2	($\theta_2 L$)
X_3	Displacement of mass m_3
$\ddot{X}$	Acceleration
α, α_1	Friction parameters
α'	Twist of blade tip relative to root ($\cos \alpha' = 0.724$)
α_h, α_{xh}	Hysteretic damping coefficients
α_x	Fluid pumping coefficient
β, β_1	Slip threshold coefficient
β_1	$4\mu\bar{N}R_o / \pi SL \cos\alpha \cos\psi$
β_2	$\mu\bar{N}R_o / LS \cos\alpha \cos\psi$
γ, γ_1	Phase angles
δ, δ_1, δ^*	Phase angles
Δ	Gap
ΔM	Added mass on impedance head
η	Loss factor
η_n, η'_n	Modal loss factor in n^{th} mode

NOMENCLATURE, continued

θ_1	X_1/L
θ_2	Rotation of blade root during slipping (X_2/L)
ϕ_1, ϕ_2	Modal functions
$\phi_1, \ldots, \phi_6$	Nondimensional parameters
ψ (t)	Deflection of body M_1
ψ	Angle of dovetail mating surfaces relative to base of root
μ	Coefficient of friction
ν	ω/ω_1 - nondimensional frequency parameter
ν_1	ω/ω_{11} - nondimensional frequency parameter
ω	Frequency (radians/sec)
ω_n	n^{th} natural frequency (radians/sec)
ω_1	Resonant frequency with
ω_{11}	Resonant frequency with no slip at m_3
Ω	Rotation speed (rpm)
Ω_o	Critical rotation speed

SECTION I

INTRODUCTION

The past several years have witnessed renewed interest in the effects of slip on dynamic response of turbine and compressor blades. This is partly because of a growing recognition that although energy dissipation mechanisms in blade-disc systems are still not well understood, this dissipation is one of the most important factors controlling the dynamic stresses, and partly because of greatly improved computational capabilities which have permitted linear analysis to reach a quite sophisticated state of development and hence made the gap in our knowledge very visible. Nonlinear analysis has not yet reached the same level of development (References 1-14).

The purpose of this report is to describe a combined analytical/ epxerimental investigation of a compressor blade having a simple dovetail root, with a view to clarifying the effect of gross slip at the root on the dynamic response behavior under harmonic excitation. The analytical part of the investigation examines the modelization of the blade in terms of a simple inertia-spring system with coulomb type frictional forces at the blade-disc interface. For simplicity, the disc is assumed to be infinitely rigid. Of course, this restriction must be relaxed before a complete blade-disc assembly is analyzed, but we are not at this point yet.

The equations of motion derived on the basis of this simple model are solved by a method of harmonic balance assuming, in effect, that under cyclic excitation the blade will exhibit cyclic response at the same frequency. The solution so obtained is examined numerically to determine regions of existence and nonexistence, i.e., to determine the frequency range over which slip occurs and that over which it does not occur (References 15-18). The agreement between analysis and experiment is found to be good for the fundamental mode of the blade, and reasonably good for the next two modes. The experiments were conducted on a blade in a simple, heavy, fixture with the normal load at the dovetail provided by two thin wires. ·

The outcome of the investigation is that one can predict with a measure of accuracy the dynamic response behavior of a simple dovetail blade, provided that the appropriate modal information is either measured or predicted by more detailed analytical procedures, such as finite element methods. Extension of the analytical method to more complex blade-disc systems is a task for the future.

SECTION II

ANALYSIS OF RESPONSE OF A BLADE WITH SLIP AT THE DOVETAIL

1. MODELIZATION OF BLADE IN MODE 1

The type of blade being considered in the analysis is illustrated in Figure 1. We shall be concentrating attention on analysis of the fundamental mode vibration response, and it is assumed that the blade resonant frequencies are well separated. The blade, when vibrating in its fundamental mode, can be modelled in terms of the simple mass-spring system shown in Figure 2, where the inertias I_1 and I_2, and the spring K_1^* are chosen to reproduce the observed modal stiffness and inertia characteristics of each individual blade geometry. I_1, I_2, and K_1^* will vary slightly with the rotation speed of the blade, but this effect is neglected here. It can be allowed for in the case of any real blade, but would simply entail changing the parameters I_1, I_2, and K_1^* at each rotation speed for which calculations are carried out. The system is modelled in terms of rotational motion because the type of motion at the root, when slip is occurring, is most naturally expressed in such terms.

2. EQUATIONS OF MOTION

For the nonlinear case where slip of the blade root takes place, the boundary condition seen by the vibrating blade changes from an essentially clamped-free condition to an essentially pinned-free condition. For the fundamental mode of the blade, the system can be represented with some degree of accuracy by the model shown in Figure 2. The equations of motion of the system with slip are:

$$I_1\ddot{\theta}_1 + K_1 (1+i\eta_1)(\theta_1 - \theta_2) = SLe^{i(\omega t - \gamma)}\cos\alpha \qquad (1)$$

$$I_2\ddot{\theta}_2 + K_1 (1+i\eta_1)(\theta_2 - \theta_1) + (\mu\bar{N}R_o/\cos\psi)\text{sgn}\,\dot{\theta}_2 = 0 \qquad (2)$$
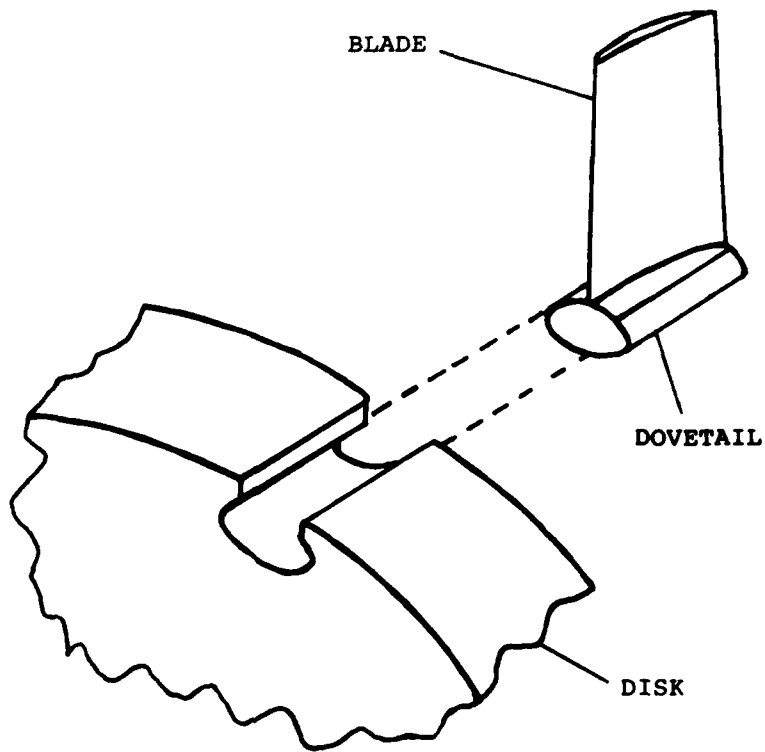
Figure 1. Sketch of Blade in Disc
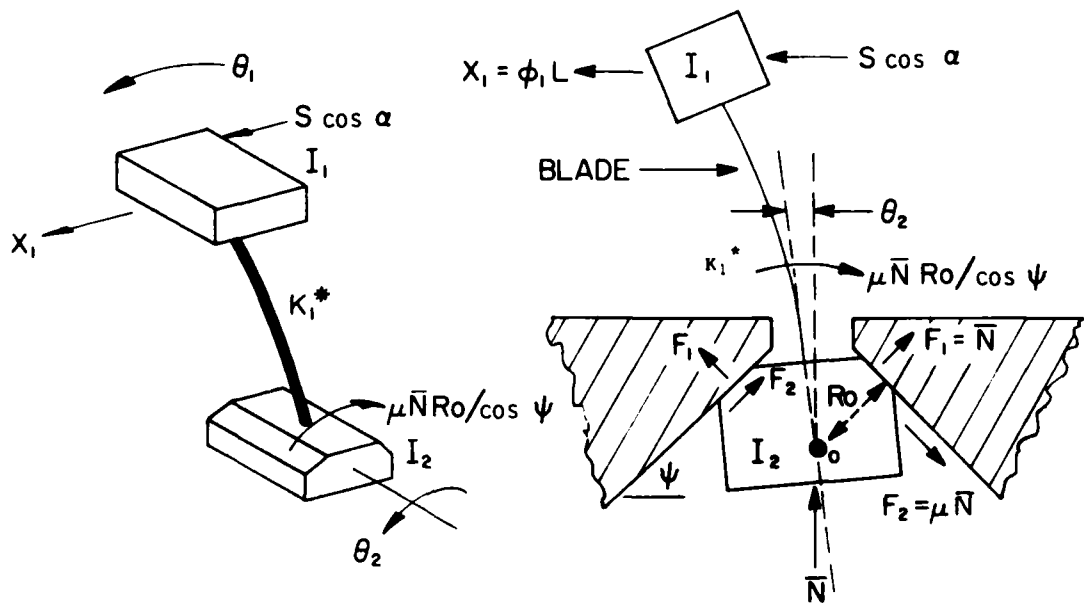
Figure 2. Discrete Mass Model of Blade (Modes 1 and 2)

The term $\mu\bar{N}R_0/\cos\psi$ is the frictional moment opposing the motion. Figure 2 shows the geometrical factors involved in this derivation. α is the angle between the blade direction at the tip leading edge (where S is applied) and the root axis as illustrated in Figure 1. From vertical equilibrium in Figure 2:

$$2F_1\cos\psi = \bar{N} \text{ i.e. } F_1 = \bar{N}/2\cos\psi$$

$$F_2 = \mu F_1 = \mu\bar{N}/2\cos\psi$$

$$\text{Moment} = 2F_2 R_0 = \mu\bar{N}R_0/\cos\psi \tag{3}$$

Equations 1 and 2 can be rewritten in the form:

$$I_1(\ddot{\theta}_1/S)+K_1(1+i\eta_1)\ (\theta_1/S-\theta_2/S) = e^{i(\omega t-\gamma)}L\cos\alpha$$

$$I_2(\ddot{\theta}_2/S)+K_1(1+i\eta_1)\ (\theta_2/S-\theta_1/S)+(\mu\bar{N}R_0/S\cos\psi)\text{sgn } \dot{\theta}_2 = 0$$

This shows that the mobility θ_1/S depends on $\mu\bar{N}/S$, so that the analysis within its limits is valid for low or high values of S or of $\mu\bar{N}$; it is the ratio of these two quantities which is important.

3.   SOLUTIONS FOR STEADY STATE MOTION

   a.   Solution for Non-Slip Condition

      If $S/\mu\bar{N}$ is sufficiently small, slip cannot occur and Equations 1 and 2 reduce to:

$$I_1\ddot{\theta}_1+K_1(1+i\eta_1)\ (\theta_1) = Se^{i(\omega t-\gamma)}L\cos\alpha \tag{4}$$

the solution of which is:

$$X_1 = \theta_1 L = SL^2\cos\alpha e^{i(\omega t-\gamma)}/[-I_1\omega^2+K_1(1+i\eta_1)] \tag{5}$$

5

The values of I_1, K_1, and n_1 needed to model a specific system are now determined by comparing the response X_1 with the measured response for low values of $S/\mu\bar{N}$. The measured resonant frequency ω_1 gives one such relationship

$$I_1\omega_1^2 = K_1 \tag{6}$$

The measured response at resonance gives another:

$$\left|\frac{\ddot{X}_1}{S}\right| = \frac{\omega_1^2 L^2 \cos\alpha}{K_1 n_1} = \frac{L^2 \cos\alpha}{I_1 n_1}$$

$$\therefore \quad I_1 = SL^2\cos\alpha/n_1|\ddot{X}_1| \tag{7}$$

and the measured damping n_1 is given by:

$$n_1 \approx \frac{\Delta\omega_1}{\omega_1} \tag{8}$$

Where $\Delta\omega_1$ is the difference between the two frequencies at which the response is 3 db below the peak response (3.01 actually!).

For example, in the case of the blade used in the experimental investigations, such calculations are summarized in Section V and the average parameters were determined to be:

$$I_1 = 1.04 \times 10^{-3} \text{ kg m}^2$$

$$K_1 = 635 \text{ Nm/radian}$$

$$n_1 = 0.010$$

$$\omega_1 = 124.2 \text{ Hz}$$

for the fundamental mode.

b. Solution with Slip

For simplicity, we let $n_1 = 0$ in Equations 1 and 2; for the purposes of this part of the analysis it is sufficient. If we seek a steady state solution of these equations, then to the first order we assume that:

$$\theta_2 = \theta_2 \sin \omega t$$
$$\theta_1 = \theta_{11} \sin \omega t + \theta_{12} \cos \omega t \tag{9}$$
$$S = S_1 \sin \omega t + S_2 \cos \omega t$$

Furthermore, we consider only the first term in the expansion of sgn $(\dot{\theta}_2)$ $\{\equiv$ sgn $(\cos \omega t)\}$ in ascending terms of $\sin(n\omega t)$ and $\cos(n\omega t)$, so that:

$$\text{sgn } (\cos \omega t) \doteqdot \frac{4}{\pi} \cos \omega t \tag{10}$$

Then, introducing these equations into Equations 1 and 2, and comparing terms in $\sin \omega t$ and $\cos \omega t$, we have the four algebraic equations for X_{11}, X_{12}, S_1, and S_2:

$$(K_1 - I_1\omega^2)\theta_{11} - K_1\theta_2 = S_1 L\cos\alpha$$
$$(K_1 - I_1\omega^2)\theta_{12} = S_2 L\cos\alpha \tag{11}$$
$$(-I_2\omega^2 + K_1)\theta_2 - K_1\theta_{11} = 0$$
$$-K_1\theta_{12} = 4\mu\bar{N}R_0/\pi\cos\psi$$

The solution of this equation is readily obtained. From the values of θ_{11}, θ_{12}, S_1, and S_2 so determined, we then can write the solution for θ_1 and S in this form:

$$\theta_1 = \frac{-S_1 (K_1 - I_2\omega^2)L\cos\alpha\sin \omega t}{\omega^2[(I_1 + I_2)K_1 - I_1 I_2\omega^2]} - \left(\frac{4\mu\bar{N}R_0}{\cos\psi\pi K_1}\right) \cos \omega t \tag{12}$$

$$SL\cos\alpha = S_1 L\cos\alpha\sin\omega t - (K_1 - I_1\omega^2)(4\mu\bar{N}R_0/\pi K_1\cos\psi)\cos\omega t \tag{13}$$

7

Clearly, we can eliminate S_1 in these two equations. This is most simply done for our present purposes by first calculating $|\theta_1|$ and $|S|$, since these are the quantities we would ordinarily measure. Then:

$$|\theta_1|^2 = \frac{S_1^2(K_1-I_2\omega^2)^2 L^2\cos^2\alpha}{\omega^4\left[(I_1+I_2)K_1-I_1I_2\omega^2\right]^2} + \left(\frac{4\mu\bar{N}R_0}{\cos\psi\pi K_1}\right)^2 \tag{14}$$

$$L^2\cos^2\alpha|S|^2 = S_1^2 L\cos^2\alpha+(K_1-I_1\omega^2)^2(4\mu\bar{N}R_0/\pi K_1\cos\psi)^2 \tag{15}$$

Eliminating S_1 and simplifying gives:

$$\left|\frac{X_1}{S}\right|^2 = \frac{L^4\cos^2\alpha\left[1-\beta_1^2(1-I_1\omega^2/K_1)^2\right]\left[1-\frac{I_2}{I_1}\left(\frac{I_1\omega^2}{K_1}\right)\right]^2}{K_1^2(I_1\omega^2/K_1)^2\left[(1+I_2/I_1)-(I_2/I_1)(I_1\omega^2/K_1)\right]^2} + \frac{\beta_1^2 L^4\cos^2\alpha}{K_1^2} \tag{16}$$

$$\left|\frac{X_2}{S}\right|^2 = \frac{L^4\cos^2\alpha[1-\beta_1^2(1-I_1\omega^2/K_1)^2]}{K_1^2(I_1\omega^2/K_1)^2[1+I_2/I_1-(I_2/I_1)(I_1\omega^2/K_1)]^2} \tag{17}$$

where

$$\beta_1 = 4\mu\bar{N}R_0/\pi SL\cos\psi\cos\alpha = (4/\pi)\beta_2 \tag{18}$$

$$\beta_2 = \mu\bar{N}R_0/SL\cos\psi\cos\alpha$$

If $\beta_1 = 0$, as for a freely pinned blade or for S very large, then $|X_1|$ has an infinite amplitude at the frequency where:

$$\left(\frac{I_1\omega^2}{K_1}\right)^2 = (1 + \frac{I_2}{I_1})\frac{I_1}{I_2} = \frac{I_1}{I_2} + 1 \tag{19}$$

8

This allows us to estimate I_2, since the pinned-free mode of the particular blade used was determined experimentally to be 429 Hz.

$$\therefore \frac{I_1}{I_2} + 1 = \frac{(429)^2}{(124.2)^2} = 11.93$$

$$I_2 = 9.51 \times 10^{-5} \text{ kg m}^2$$

for the particular blade used in the experimental investigation. A calculator program to determine $|X_2/S|$ and $|X_1/S|$ is given in Table 1. It is seen from Equation 17 that $|X_2/S|$ can exist only over a narrow range of frequencies, and it is only within this band that slip can occur. Outside this range, although $|X_1/S|$ as given by Equation 16 may exist, the original assumption that $|X_2/S|$ exists is violated and hence we must return to the linear solution given by Equation 5. Figures 3 to 10 show the calculated values of $|X_1/S|$ and $|X_2/S|$ versus frequency for $B_2 = 50$, 20, 10, 5, 2, 1, $\pi/4$, 0.3 and for the aforementioned values of I_1, I_2, K_1, and η_1. Figure 11 shows a summary of the solution for several values of B_2. These analytical results will be compared with experiment in Section V.

    c. Graphical Solution for Slip Motion and Hysteretic Damping

The equation of motion of the system with slip and hysteretic stiffness can be written in the more general form:

$$I_1\ddot{\theta}_1 + \frac{k_1\eta_1}{\omega}\dot{\theta}_1 + k_1\theta_1 - \frac{1}{2}\left(\frac{k_1\eta_1}{\omega}\dot{\theta}_2 + k_1\theta_2\right)(1+\text{sgn }\beta) = S_1\cos\omega t \qquad (20)$$

$$\left[I_2\ddot{\theta}_2 + \mu\bar{N}R\text{ sgn }\dot{\theta}_2 - \frac{k_1\eta_1}{\omega}(\dot{\theta}_1-\dot{\theta}_2) - k_1\theta_1\right]\frac{1}{2}(1+\text{sgn }\beta) + k_1\theta_2 = 0$$

where

$$S_1 = S\cos\alpha$$

9

TABLE 1

HP67 CALCULATOR PROGRAM TO CALCULATE RESPONSE

<u>Input:</u> put ω in x register (Hz)

Manual storage: Storage location 0 - K_1(635 Nm/rad)

               "   "   1 - ω_1(120 Hz)

               "   "   2 - I_2/I_1(.0915)

               "   "   3 - β_2(10)

               "   "   4 - η_1(.01)

               "   "   5 - L(.20)

               "   "   6 - $\cos\alpha$(.724)

Output: Label A - $|X_1/S|$ linear (Equation 5)

         Label B - $|X_1/S|$ slip   (Equation 16)

         Label C - $|X_2/S|$ slip (Equation 17)

         Note: Label A, B, and C must be operated in sequence.

<u>Internal storage</u>

         Storage location A - ω^2 rad^2/sec^2

            "   "   B - I_1

fcl PRGM	STO C	RCL A	gx^2	gx^2
fLBLA	RCL o	x	$\div$	RCL D
2	RCL 4	STO C	RCL C	x
x	x	1	gx^2	STO E
h π	gx^2	$-$	$\div$	RCL 3
x	RCL C	RCL 3	STO D	4
gx^2	$+$	x	RCL C	x
STOA	f$\sqrt{x}$	4	RCL 2	hπ
RCL 1	h$\frac{1}{x}$	x	x	$\div$
2		hπ	CHS	RCL o
x	RCL 5	$\div$	1	$\div$
h π	gx^2	gx^2	$+$	RCL 5
x	x	CHS	RCL 2	gx^2
gx^2	RCL 6	1	$+$	x
h$\frac{1}{x}$	x	$+$	gx^2	RCL 6
RCL o	hRTN	STO D	h$\frac{1}{x}$	x
x	fLBL B	RCL 5	RCL D	gx^2
STOB	RCL1	4	x	RCL E
RCL A	2	hy^x	STO D	$+$
x	x	RCL D	RCL C	f$\sqrt{x}$
RCL o	hπ	x	RCL 2	h RTN
$-$	x	RCL 6	x	fLBLC
gx^2	gx^2	gx^2	1	RCLD
	h$\frac{1}{x}$	x	$-$	f$\sqrt{x}$
		RCL o		h RTN

Figure 3.   Predicted Response of
            Blade in Mode 1 for β_2 = .50
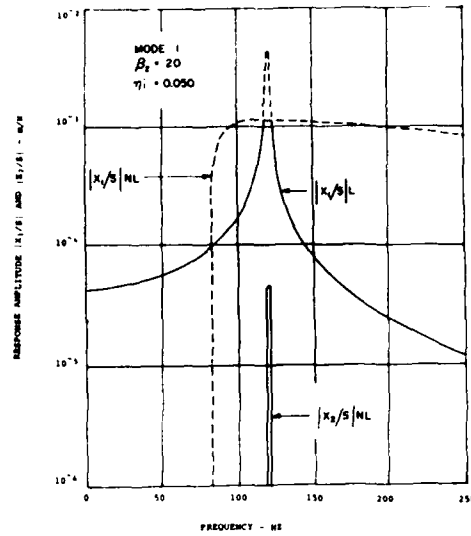
Figure 4.   Predicted Response of
            Blade in Mode 1 for β_2 = 20
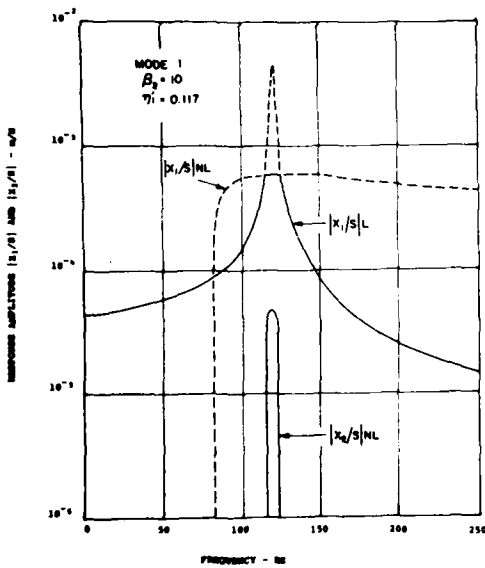
Figure 5.   Predicted Response of
            Blade in Mode 1 for β_2 = 10
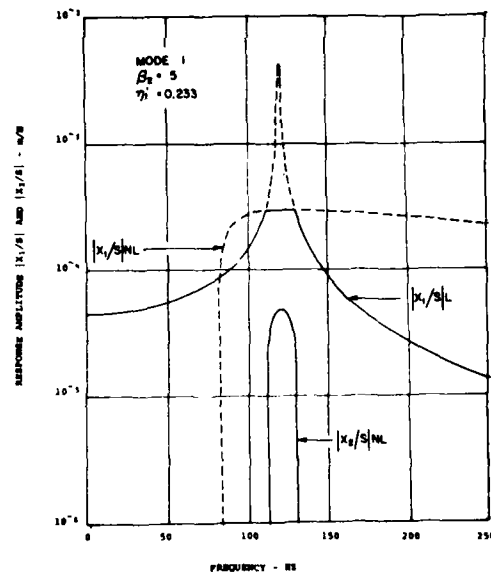
Figure 6.   Predicted Response of
            Blade in Mode 1 for β_2 = 5
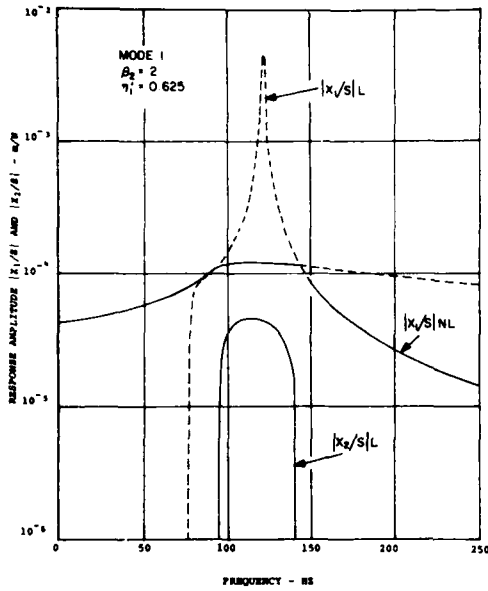
Figure 7. Predicted Response of Blade in Mode 1 for $\beta_2 = 2$
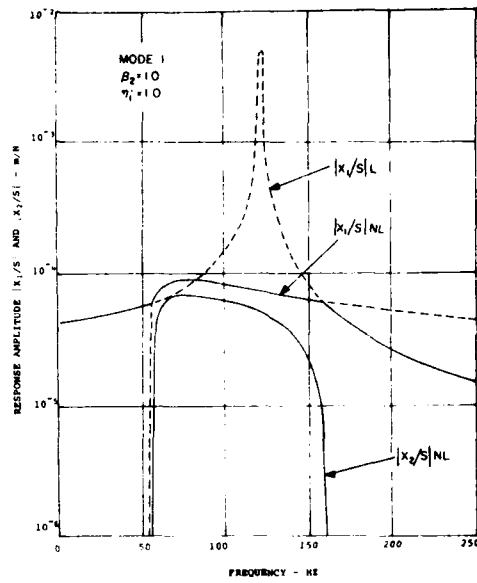
Figure 8. Predicted Response of Blade in Mode 1 for $\beta_2 = 1$
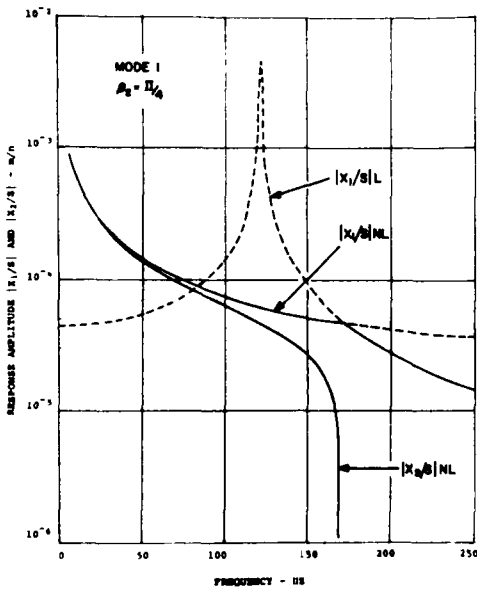
Figure 9. Predicted Response of Blade in Mode 1 for $\beta_2 = \pi/4$
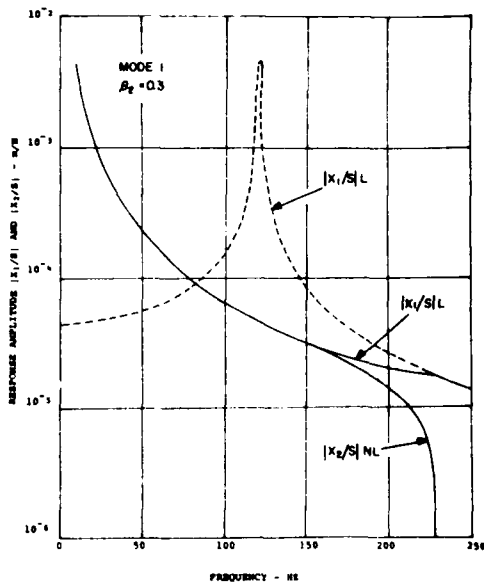
Figure 10. Predicted Response of Blade in Mode 1 for $\beta_2 = 0.3$

12
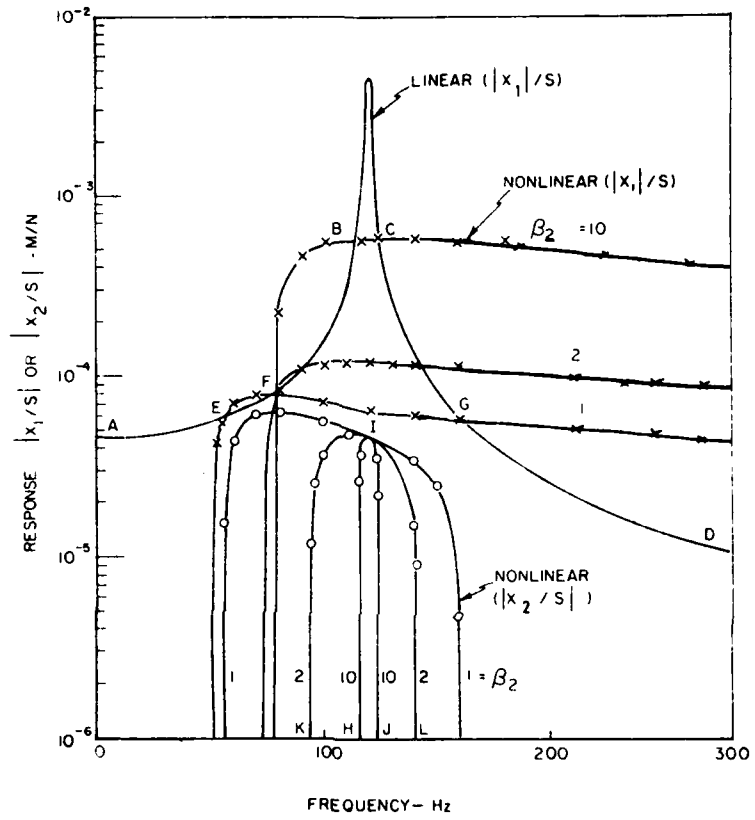
Figure 11.   Graphs of $|X_1/S|$ and $|X_2/S|$ versus Frequency (Summary)

For $\beta < 0$: $\theta_2 = 0$ – one degree of freedom

For $\beta > 0$: two degrees of freedom

$\beta = 0$ is the condition of the threshold of slip (it will be defined later)

R – geometrical parameter $(R_0/\cos\psi)$

η_1– hysteretic damping coefficient

The solution of Equation 20 is:

$$\theta_2(t) = A \cos(\omega t + \gamma) \tag{21}$$

put into Equation 1 and expanding the function sign $[-A\omega\sin(\omega t + \gamma)]$ in the Fourier series and leaving only the first term we reduce the problem to solving the linearized system

$$\begin{cases} I_1\ddot{\theta}_1 + \dfrac{k_1\eta_1}{\omega}(\dot{\theta}_1-\dot{\theta}_2) + k_1(\theta_1-\theta_2) = S_1\cos\omega t \\[3mm] I_2\ddot{\theta}_2 + \dfrac{k_1\eta_1}{\omega}(\dot{\theta}_2-\dot{\theta}_1) + k_1(\theta_2-\theta_1) = \dfrac{4\mu\bar{N}R}{\pi}\,\text{sgn}A \end{cases} \tag{22}$$

looking for the solution in the form

$$\begin{cases} \theta_1(t) = D \cos(\omega t + \gamma-\delta) \\[3mm] \theta_2(t) = A \cos(\omega t + \gamma) \end{cases} \tag{23}$$

if the condition $\beta > 0$ is satisfied. If we have $\beta \leq 0$ we look for the solution

$$\theta_1(t) = D^* \cos(\omega t-\gamma^*) \tag{24}$$

of the equation

$$I_1\ddot{\theta}_1 + \dfrac{k_1\eta_1}{\omega}\dot{\theta}_1 + k_1\theta_1 = S_1\cos\omega t \tag{25}$$

14

The last one gives

$$D^* = \frac{S_1}{k_1 \sqrt{(1-\frac{I_1\omega^2}{k_1})^2 + \eta_1^2}} \quad , \quad \delta^* = \arctan \frac{k_1\eta_1}{k_1 - I_1\omega^2} \qquad (26)$$

Putting Equation 23 into Equation 22 we get

$$A^2\omega^4\phi_1 - 2A\omega^2\alpha_1 (\text{sgn } A)\phi_2 + \alpha_1^2[(\eta_1\nu)^2 + (\nu-1)^2] = S_1^2 \qquad (27)$$

$$\phi_1 = [I_2(\nu-1)-I_1] + (\eta_1\nu I_2)$$

$$\phi_2 = \eta_1\nu[2I_2(\nu-1)-I_1]$$

$$\phi_3 = \{(\nu-1)[I_2(\nu-1)-I_1] - I_2(\eta_1\nu)^2\}^2$$

$$\nu = \frac{I_1\omega^2}{k_1(1+\eta_1^2)}$$

$$\alpha_1 = \frac{4\mu\bar{N}R}{\pi}$$

From Equation 27 we set the amplitude A:

$\frac{S_1}{\alpha_1} > \sqrt{(\nu-1)^2 + (\eta_1\nu)^2}$	$\sqrt{\frac{\phi_3}{\phi_1}} \leq \frac{S_1}{\alpha_1} \leq \sqrt{(\nu-1)^2 + (\eta_1\nu)^2}$		$\frac{S_1}{\alpha_1} < \sqrt{\frac{\phi_3}{\phi_1}}$
A=	$\omega^2 \geq \bar{\omega}^2$	$\omega^2 < \bar{\omega}^2$	
$\frac{\pm \alpha_1\phi_2 + \sqrt{S_1^2\phi_1 - \alpha_1^2\phi_3}}{\omega^2\phi_1}$	$A = \frac{\pm\alpha_1\phi_2 \pm \sqrt{S_1^2\phi_1 - \alpha_1^2\phi_3}}{\omega^2\phi_1}$	amplitude does not exist	

where:

$$\bar{\omega}^2 = k_1(1+\eta_1^2)\left[\frac{1}{2I_2} + \frac{1}{I_1}\right]$$

and the phase angle

$$\gamma = \arctan \frac{A\omega^2\eta_1 I_2\nu + (1-\nu)\alpha_1}{\alpha_1\eta_1\nu - A\omega^2[I_2(\nu-1)-I_1]}$$

The amplitude of the solution (Equation 23) is given in the table on the previous page. As one can see for some values of the parameters we have two values of A (one positive and one negative) or four values (real ones!) In some region the solution (Equation 23) does not exist; it is the domain of the solution (Equation 24) of the reduced system.

The coefficient of the threshold of slip "β" can be defined as shown in the above table:

$$\beta = \frac{S_1}{\alpha_1} - \sqrt{\frac{\phi_3}{\phi_1}} = \frac{\pi S_1}{4\mu\bar{N}R} - \frac{\left|(\nu-1)[I_2(\nu-1)-I_1]-I_1(n_1\nu)^2\right|}{\sqrt{[I_2(\nu-1)-I_1]^2 + (n_1\nu I_2)^2}} \tag{28}$$

The relationship between A and the amplitude D is

$$D = \frac{1}{\sqrt{1+n_1^2}} \sqrt{A^2\left(1-\frac{I_1\omega^2}{k_1}\right)^2 + \left(An_1+\frac{\alpha_1}{k_1}\right)^2} \tag{29}$$

$$\gamma = \arctan \frac{An_1I_2\omega^2 + \alpha_1}{AI_2\omega^2 - Ak_1(1+n_1^2) - n_1\alpha_1} \tag{30}$$

where A is calculated from Equation 27. (See table)

A(ω) curves are plotted graphically as in Figure 12

$$\omega_{1,2}^2 = \frac{k_1(1+n_1^2)}{2(1-n_1^2)}\left[\frac{1}{I_2} + \frac{2}{I_1} \pm \sqrt{\frac{1}{I_2^2} + \frac{4n_1^2}{I_1}\left(\frac{1}{I_1} + \frac{1}{I_2}\right)}\right]$$

$$\omega^* = \frac{1}{1+n_1^2}\sqrt{\frac{k_1}{I_1}}$$

Different levels of $\frac{S_1}{\alpha_1}$ give different shapes of the $|A|(\omega)$ curve

(qualitative shape!)

16
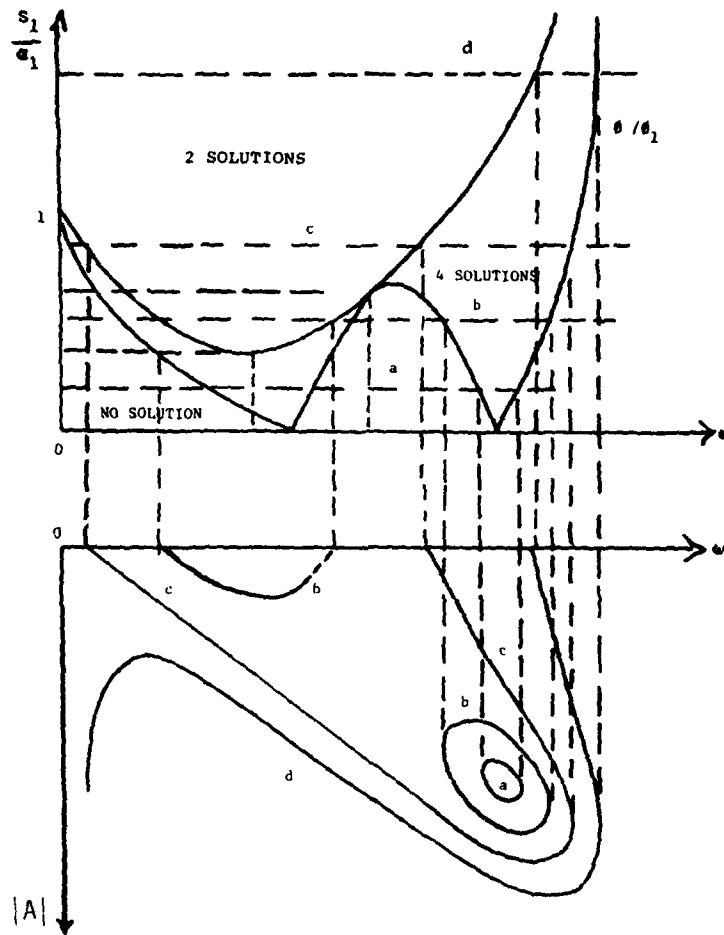
Figure 12.   Graphs of $|A|$ and S_1/α_1 versus ω

The case $\eta_1 = 0$ (Figure 13) gives:

$$A = \pm \frac{\sqrt{S_1^2 - \alpha_1^2 \left(\frac{I_1\omega^2}{k_1} - 1\right)^2}}{\omega^2 \left(\frac{I_1 I_1 \omega^2}{k_1} - I_1 - I_2\right)} \quad , \quad D = \sqrt{A^2 \left(1 - \frac{I_2\omega^2}{k_1}\right)^2 + \left(\frac{\alpha_1}{k_1}\right)^2} \qquad (31)$$

$$D^\ast = \frac{S_1}{k_1 - I_1\omega^2}$$

A method of connection of the solution D from A is given in Figure 14.

The curves are plotted in an acceleration scale for comparison with the experimental data. It is only a qualitative picture here.

4.   CALCULATION OF APPARENT DAMPING

As Figures 3 to 10 show, the response mobility $|X_1/S|$ of the blade does not have the classical damped single degree of freedom system shape but is sharply "cut-off" when slip occurs. Strictly speaking the system is not "classically" damped and cannot be assigned a true measure of modal damping. However the shape of $|X_1/S|$ as a function of frequency depends only on β_2, and for each value of β_2 this shape is unique. One may therefore define an "apparent modal damping" by the usual "half power bandwidth" definition, i.e., in Figures 3 to 10 we seek the frequencies f_1^+ and f_1^-, when the response is $1/\sqrt{2}$ times the peak amplitude (-3.01 db) and define the apparent damping as:

$$\eta_1' = \frac{f_1^+ - f_1^-}{f_1} \qquad (32)$$

On this basis, we can plot a graph of η_1' versus $1/\beta_2$ as in Figure 15. η_1' increases as $1/\beta_2$ increases, at least within the range of values examined here. For $1/\beta_2 \leq 0.01$, the value of η_1' remains at the non-slip value $\eta_1 \simeq 0.01$ observed in the tests.
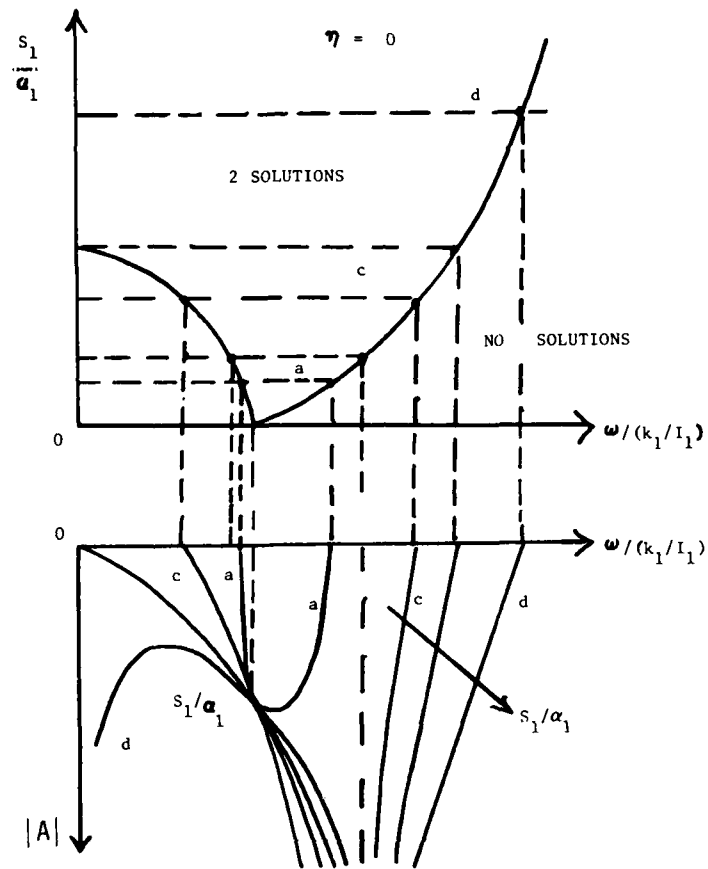
Figure 13. Graphs of $|A|$ and S_1/α_1 versus $\omega/\sqrt{(K_1/I_1)}$
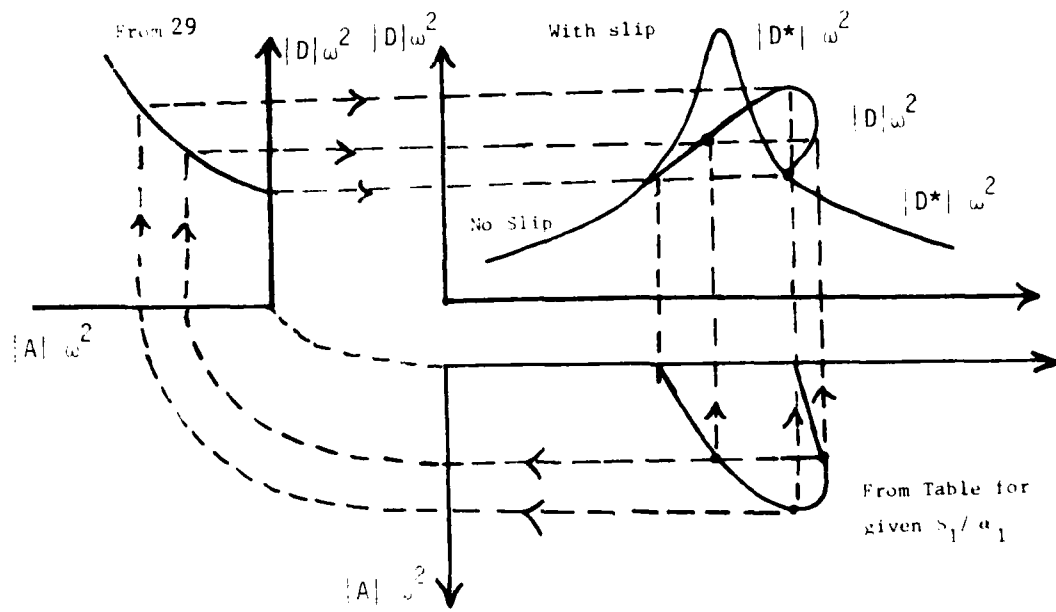
Figure 14. Graphical Method of Connecting $|D|$ and $|A|$
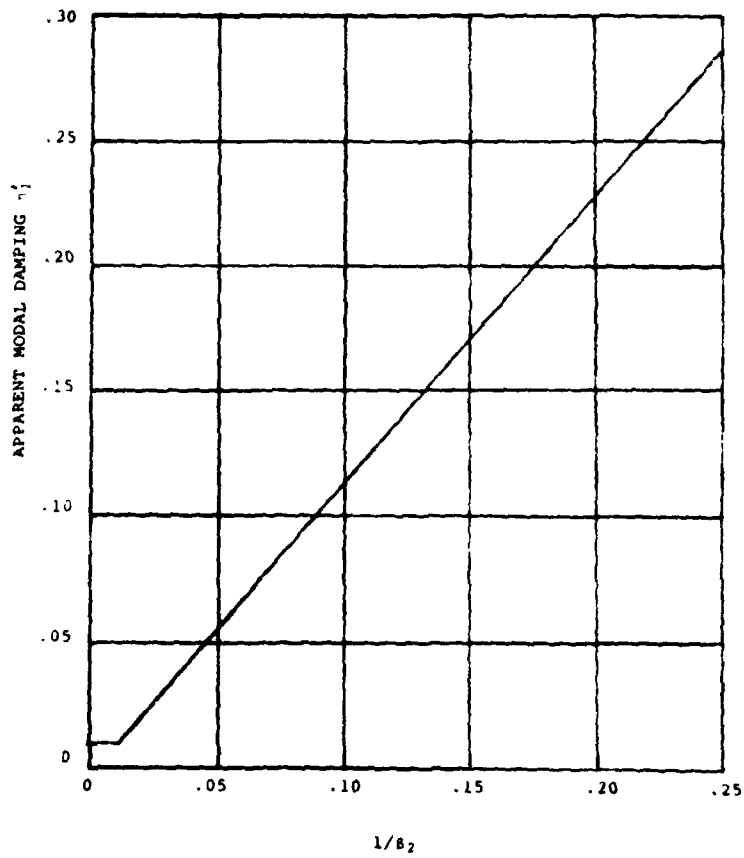
Figure 15. Graph of Predicted Apparent Damping η_1' versus $1/\beta_2$

One can also examine the bending moment at the root as a function of β_2. The value of M is given by:

$$M = K_1 \theta_1 = \frac{K_1 X_1}{L}$$

$$\left| \frac{M}{SL} \right| = \frac{K_1}{L^2} \left| \frac{X_1}{S} \right| \tag{33}$$

For a specific blade, one can determine the relationship between M and the maximum stress in the fundamental (or any other) mode, but at present it is sufficient to examine $|M/SL|$ as a function of β_2 as determined from Figures 3 to 10. The resulting graph of $|M/SL|$ versus β_2 is shown in Figure 16.

5. CALCULATION OF EFFECTS OF ROTATION SPEED ON APPARENT DAMPING

It is generally difficult to predict the response of a blade at high rotational speed because the exciting forces on a blade are not known a-priori. However, for a given blade geometry S will depend on the rotation speed Ω in the manner:

$$S = S_o \left(\frac{\Omega}{\Omega_o} \right)^n \tag{34}$$

where S_o is the force at some speed Ω_o and n is an exponent not necessarily equal to 2. S will be a maximum at the various multiples of the blade passage frequencies, so that the excitation force at any condition where a blade passage frequency is near to a natural frequency will be nearly harmonic.

The normal force N resulting from the rotation speed Ω is given, as a crude approximation, by a relationship of the type:

$$\overline{N} = MR \left(\frac{2 \pi \Omega}{60} \right)^2 \tag{35}$$
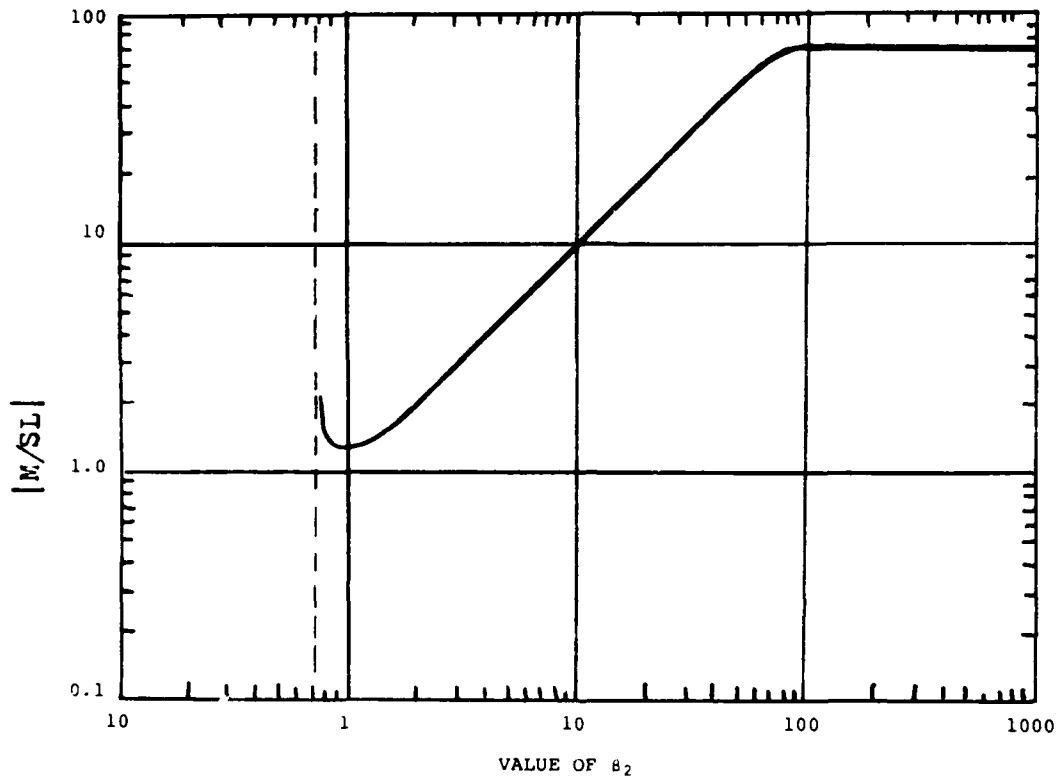
Figure 16. Graph of Predicted Value of $|M/SL|$ versus β_2 for Mode 1

where M is the blade mass, R an average radius and Ω the rotation speed in rpm. It is seen that if n = 2, β_2 is constant at all speeds and hence that the damping due to slip will be the same at all speeds, which is contrary to observation. Hence one must conclude that in most cases n < 2. For example, if we assume that n = 1.5:

$$\beta_2 = \frac{4\pi^2 \mu MRR_o \Omega^{0.5} \Omega_o^{1.5}}{S_o L \cos\psi \cos\alpha (60)^2} \tag{36}$$

As a hypothetical example, consider the cases where μ = 0.15, 0.1 and 0.05, M = 0.235 kg, R = 0.5m, R_o = 0.01m, Ω_o = 15000 rpm, S_o = 40N, L = 0.2m, $\cos\psi$ = 0.5, $\cos\alpha$ = 0.724. Then:

$$\beta_2 = 8.0\mu\, \Omega^{0.5} \tag{37}$$

For each value of μ and Ω, one can calculate β_2 and hence read the value of effective loss factor off Figure 15. Some predicted graphs of the *effective loss factor versus* Ω are plotted in Figure 17. It is seen that for μ = 0.15, the behavior is very similar to that observed in a test engine stage (Reference 2), but that as μ is decreased, the apparent modal damping increases rapidly. It is seen from Equation 36 that it is desirable to reduce μ,M,R and R_o, and increase S_o, L, $\cos\psi$ and $\cos\alpha$, as far as possible, to achieve high "damping".

6. MODELIZATION OF BLADE IN SECOND BENDING MODE

For the second bending mode of a blade, or for any mode in which the deformations are primarily bending, the model selected for the fundamental mode, illustrated in Figure 2, is directly applicable and only the value of I_1, I_2 and K_1^*, will be different. This means that Equations 1 and 2 and the solutions (Equations 16 and 17) are directly usable. From the low level tests described in Section V, the corresponding values of I_1, K_1, and η_1 are:

$$I_1 = 1.62 \times 10^{-3} \text{kg m}^2$$
$$K_1 = 11000 \text{ Nm/rad}$$
$$\eta_1 = 0.0067$$
$$\omega_1 = 415 \text{ Hz}$$
$$I_2/I_1 = 0.150$$

24
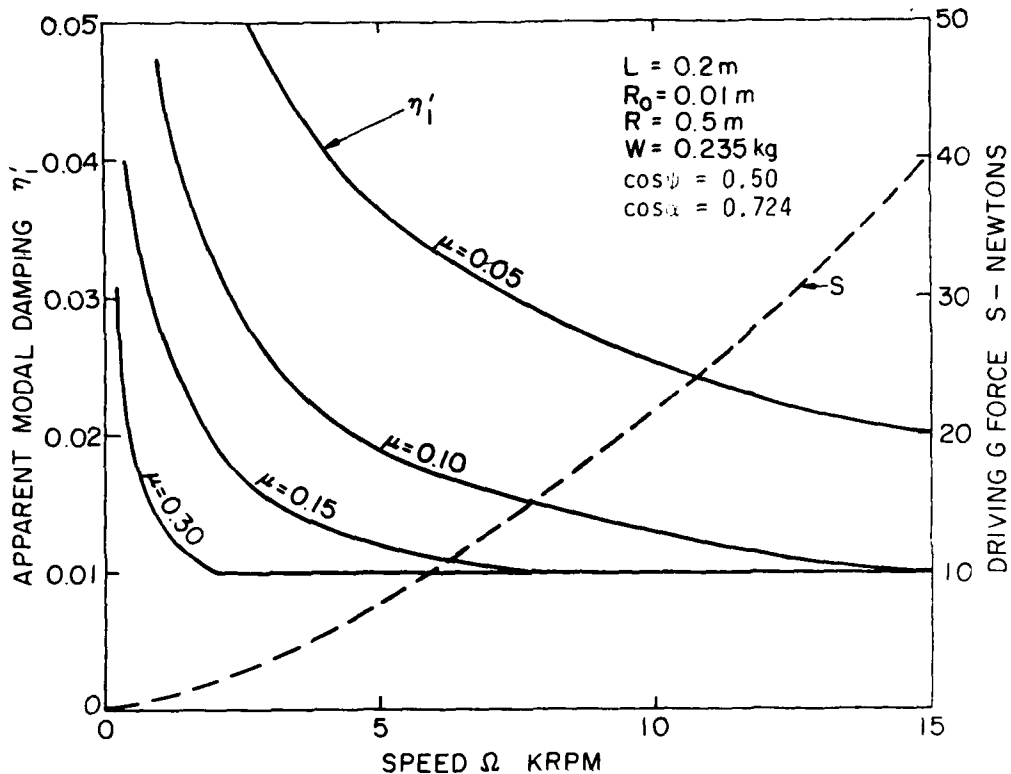
Figure 17. Typical Predicted Variation of η_1' with Ω

The corresponding solution for β_2, defined as before, equal to 50, 20, 10, 5, 2, 1, 4, and 0.3 are illustrated in Figures 18 to 25.

The difference between the second mode solution and the fundamental mode solution is seen to result only from the altered values of I_1, K_1, η_1, and ω_1. This will be true for all the essentially "bending-type" modes for which the moment at the root caused by the blade deformation is in one direction only, and is not a twisting type of moment, as for the torsional modes.

The value of I_2 is determined from the ratio of the second mode resonant frequencies in the clamped-free and pinned-free conditions. For this blade $I_2 = 2.43 \times 10^{-4}$ kg m^2.
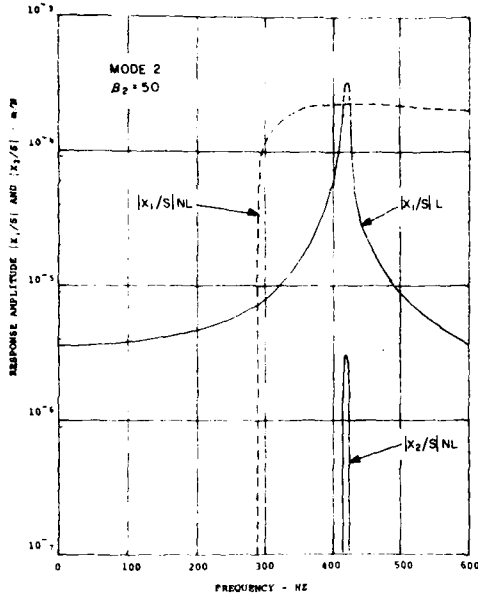
Figure 18. Predicted Response of
Blade in Mode 2 for β_2 = 50
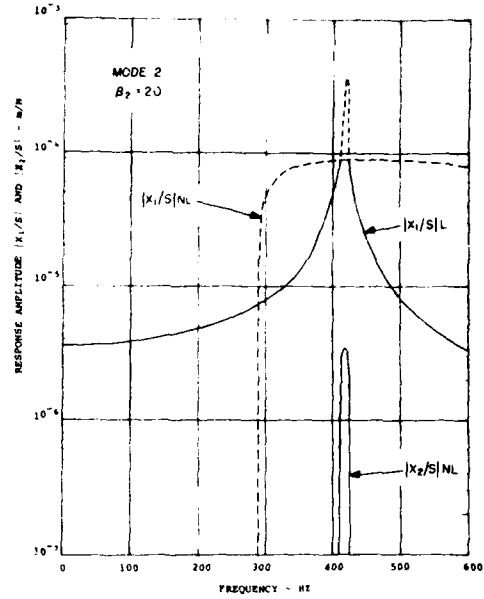
Figure 19. Predicted Response of
Blade in Mode 2 for β_2 = 20
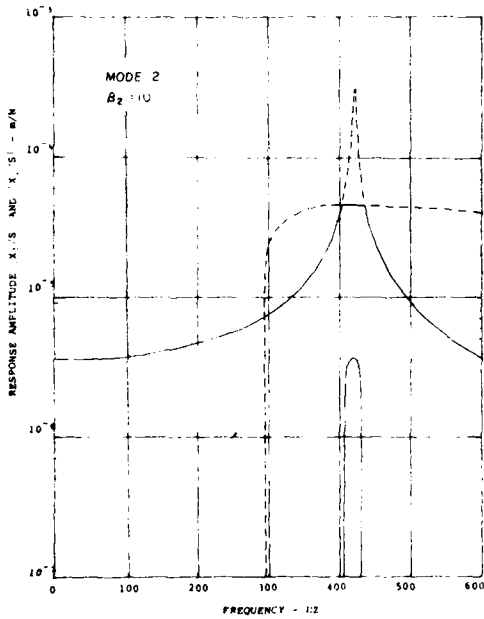
Figure 20. Predicted Response of
Blade in Mode 2 for β_2 = 10
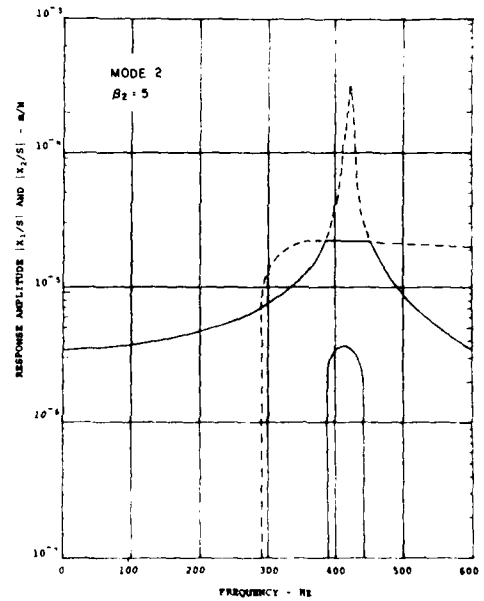
Figure 21. Predicted Response of
Blade in Mode 2 for β_2 = 5
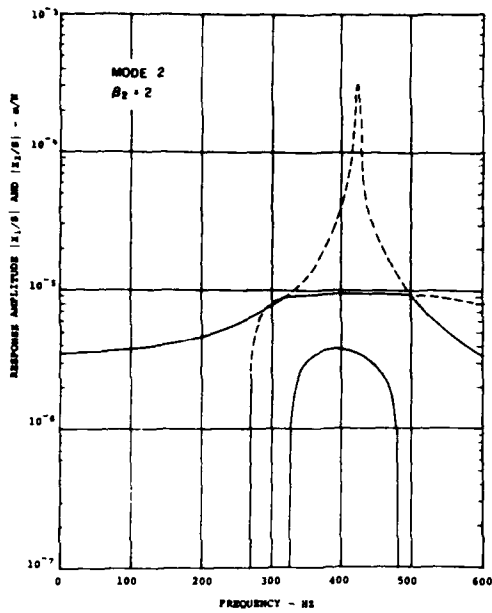
Figure 22.   Predicted Response of
            Blade in Mode 2 for β_2 = 2
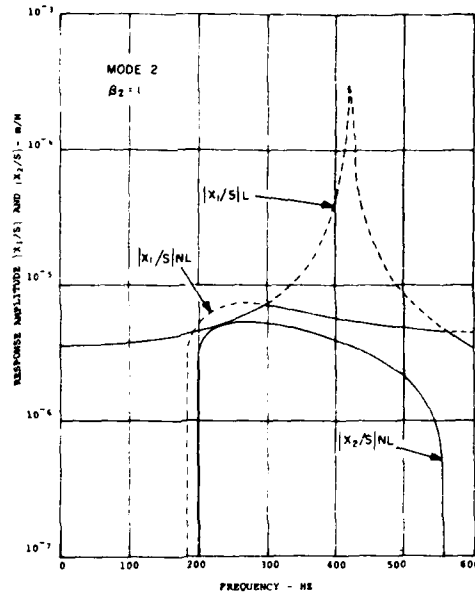
Figure 23.   Predicted Response of
            Blade in Mode 2 for β_2 = 1
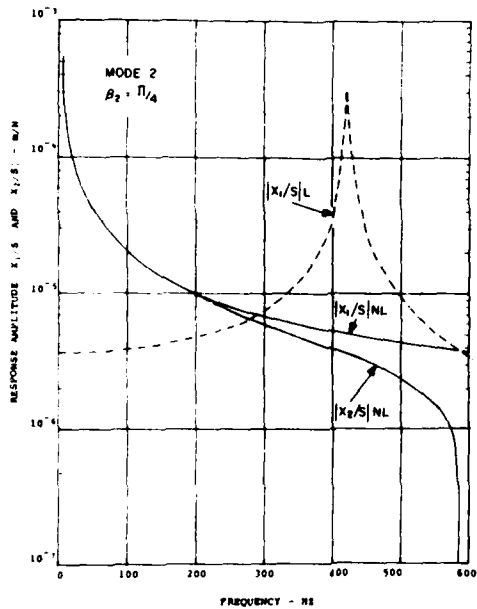
Figure 24.   Predicted Response of
            Blade in Mode 2 for β_2 = $\pi/4$
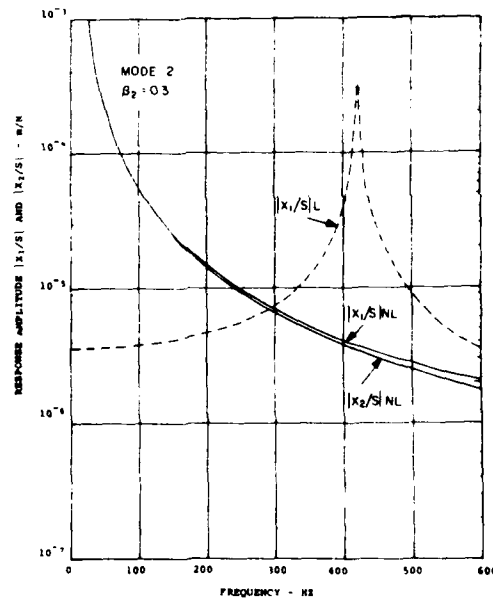
Figure 25.   Predicted Response of
            Blade in Mode 2 for β_2 = 0.3

27

7. MODELIZATION OF BLADE IN FIRST TORSIONAL MODE

The third mode observed in the response spectrum appears to be a torsional type. For this case, the moment at the root when slip occurs is of a twisting type, as illustrated in Figure 26. In this case I_1 becomes the torsional inertia of the blade, I_2 that of the root, and K_1 the torsional stiffness. The equation of the blade therefore becomes, in any predominantly torsional type of mode:

$$I_1\ddot{\theta}_1 + K_1 (1+in_1) (\theta_1 - \theta_2) = Sbe^{i(\omega t - \gamma)}\cos\alpha$$

$$I_2\ddot{\theta}_2 + K_1 (1+in_1) (\theta_2 - \theta_1) + (\mu\bar{N}b_o)sgn\dot{\theta}_2 = 0$$

when θ_1 and θ_2 are now the torsional deflection of the blade, i.e., for this type of mode $X_1 = \theta_1 b$ and $X_2 = \theta_2 b$.

$$I_1(\ddot{\theta}_1/S) + K_1 (1+in_1)(\theta_1/S - \theta_2/S) = b\cos\alpha\, e^{i(\omega t - \gamma)}$$

$$I_2(\ddot{\theta}_2/S) + K_1 (1+in_1)(\theta_2/S - \theta_1/S) = (\mu\bar{N}b_o/S)sgn\dot{\theta}_2$$

(38)

We therefore recover the fundamental mode solution of Equations 16 and 17 if we replace L by b and $\mu\bar{N}R_o/SL\cos\alpha\,\cos\psi$ by $\mu\bar{N}b_o/Sb\cos\alpha$. The corresponding values of I_1, I_2, K_1, n_1, and ω_i are given in Section 5. Figures 27 to 34 show some typical calculated results.

8. NORMAL MODE ANALYSIS OF BLADE RESPONSE WITHOUT SLIP

In order to establish the low amplitude level behavior of the blade, and to identify parameters in a preliminary fashion, it is essential to first consider the behavior of the blade with no slip at the root. In this case, in the fundamental mode, the blade behaves essentially as a clamped-free beam. Since the blade is twisted, it is necessary to define a coordinate system within the middle surface as illustrated in Figure 35.
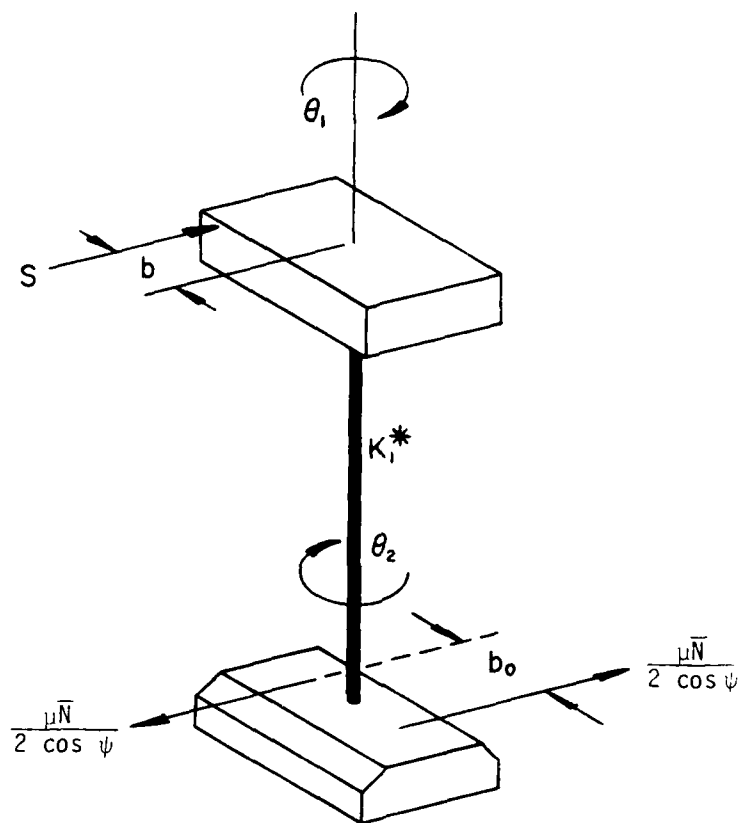
Figure 26.   Discrete Mass Model of Blade with Torsion - Mode 3
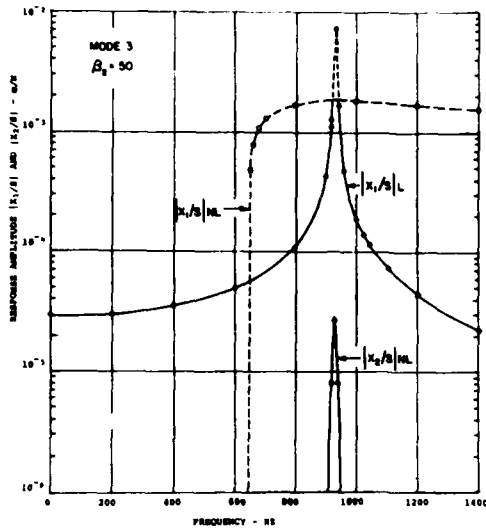
Figure 27. Predicted Response of
Blade in Mode 3 for β_2 = 50
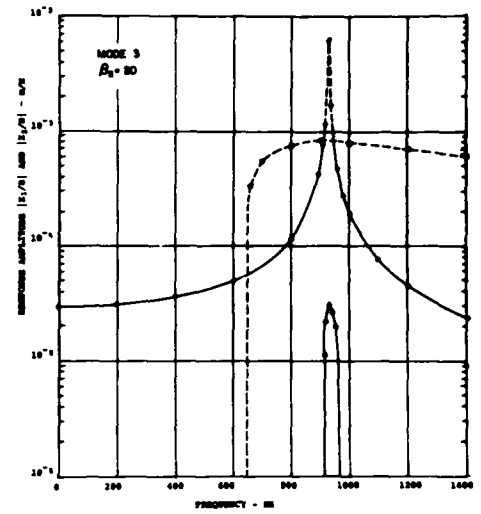
Figure 28. Predicted Response of
Blade in Mode 3 for β_2 = 20
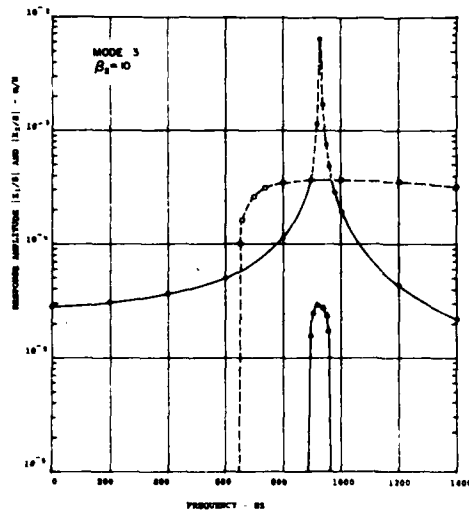
Figure 29. Predicted Response of
Blade in Mode 3 for β_2 = 10
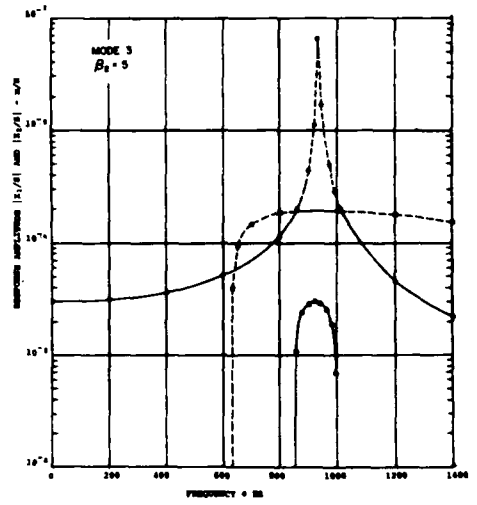
Figure 30. Predicted Response of
Blade in Mode 3 for β_2 = 5

30
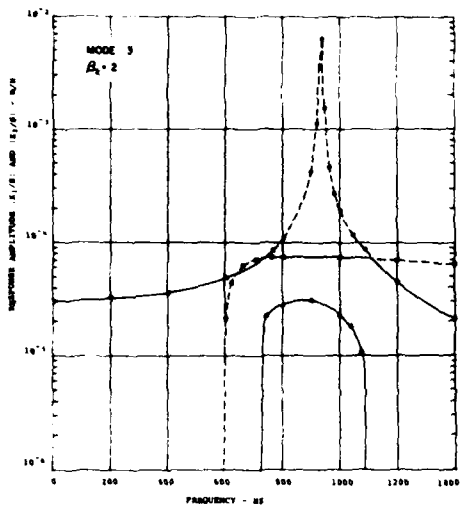
Figure 31. Predicted Response of Blade in Mode 3 for $\beta_2 = 2$
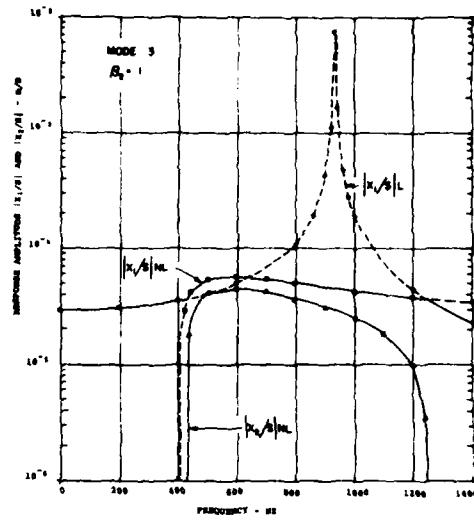
Figure 32. Predicted Response of Blade in Mode 3 for $\beta_2 = 1$
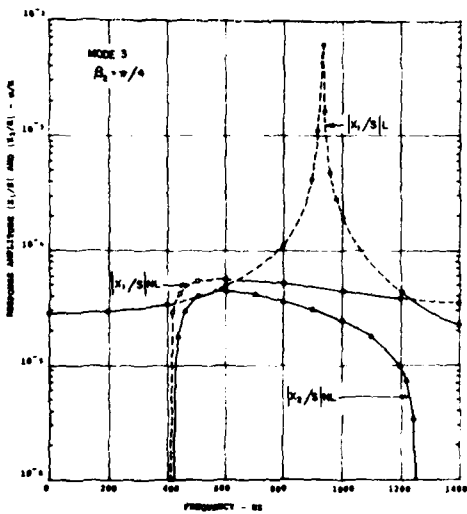
Figure 33. Predicted Response of Blade in Mode 3 for $\beta_2 = \pi/4$
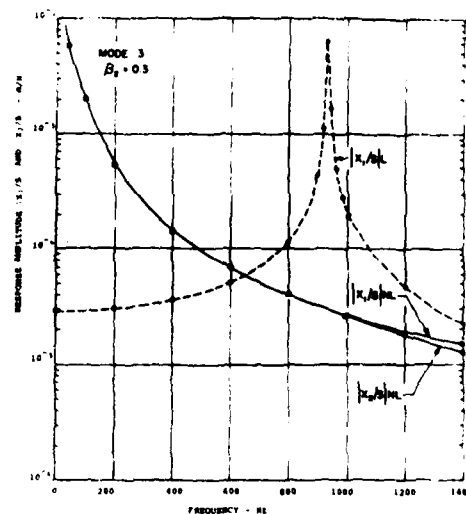
Figure 34. Predicted Response of Blade in Mode 3 for $\beta_2 = 0.3$
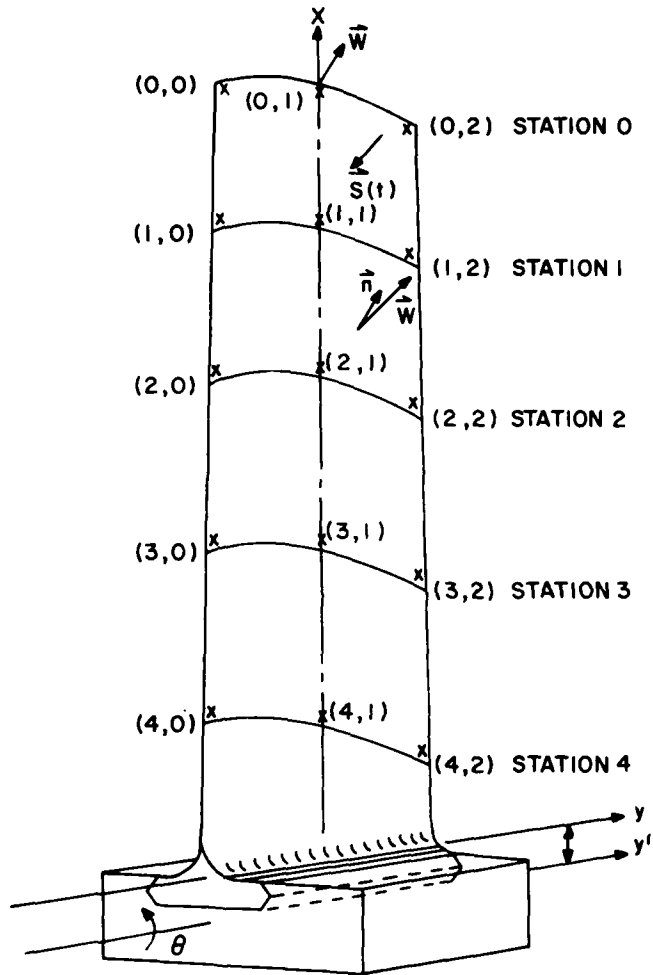
Figure 35.   Sketch of Blade Coordinate System

If the blade is then subjected to an exciting force $\vec{S}(t) = \vec{S}\delta(x-x_1)\,\delta(y-y_1)\sin \omega t$ normal to the middle surface at the point (x_1,y_1), then the equation of motion of the system can be written:

$$L^3 \Delta(K\star\vec{W}) + \mu(\partial^2\vec{W}/\partial t^2) = \vec{S}\delta(x-x_1)\,\delta(y-y_1)\sin \omega t \tag{39}$$

where $K\star$ is the complex stiffness of the blade, assuming hysteretic damping and Δ is a differential operator in the space variables x and y, and μ is the mass per unit area at the point x,y. Since the blade is usually very stiff in-plane and much more flexible normal to the middle surface, W is practically normal to the middle surface quite frequently. Now if the normal modes are known, from experiment or analysis, the displacement $\vec{W}$ can be expressed as a series of normal modes:

$$\vec{W} = \sum_{n=1}^{\infty} W_n \vec{\phi}_n (x,y) \tag{40}$$

where W_n is a scalar, depending on time, representing the amplitude of the nth normal mode and $\vec{\phi}_n$ is a vector representing the normalized displacement function in this mode. By definition, the normal modes are the set of discrete functions which satisfy the homogeneous equation:

$$\Delta(K\vec{\phi}_n) - (\mu\,\omega_n^2/L^3)\vec{\phi}_n = 0 \tag{41}$$

This classical relationship allows one to convert Equation 39 from a complex partial differential equation in the space variables to an infinite series (hopefully convergent) of algebraic equations: Putting Equations 40 and 41 into Equation 39 gives; in complex notation:

$$\sum_{n=1}^{\infty} [(1+i\eta)\mu\omega_n^2 W_n + \mu\ddot{W}_n]\vec{\phi}_n = \vec{S}\exp(i\omega t)\delta(x-x_1)\delta(y-y_1) \tag{42}$$

one must now make use of the orthogonal property of the normal modes:

$$\int_x \int_y \mu\vec{\phi}_n \cdot \vec{\phi}_m dxdy = \delta_{mn} \tag{43}$$

where $\delta_{mn} = 0$ for $m \neq n$ and $\delta_{mm} = 1$ for $m = n$. Therefore, the factoring Equation 42 by ϕ_1 and integrating over the surface gives:

$$[(1+i\eta)\omega_1^2 W_1 + \ddot{W}_1] \int_x \int_y \mu \vec{\phi}_1 \cdot \vec{\phi}_1 \, dxdy = \int_x \int_y \vec{S} \cdot \vec{\phi}_1 \delta(x-x_1)\delta(y-y_1)e^{i\omega t} \, dxdy$$

where $\vec{\phi}_1 \cdot \vec{\phi}_1$ is the scalar product of the vector $\vec{\phi}_1$ with itself. This equation can clearly be written:

$$m_1'[\omega_1^2(1+i\eta)-\omega^2]W_1 = \beta_1' S e^{i\omega t} \qquad (44)$$

where m_1' is the mass of the blade and β_1 is a nondimensional parameter:

$$m_1' = \int_x \int_y \mu \, dxdy \qquad (45)$$

$$\beta_1' = \frac{m_1' \int_x \int_y \vec{n} \cdot \vec{\phi}_1 \delta(x-x_1)\delta(y-y_1)dxdy}{\int_x \int_y \mu \vec{\phi}_1 \cdot \vec{\phi}_1 dxdy}$$

$$= \frac{m_1' \vec{n}(x_1,y_1) \cdot \vec{\phi}_1(x_1,y_1)}{\int_x \int_y \mu \vec{\phi}_1 \cdot \vec{\phi}_1 dxdy} \qquad (46)$$

where $\vec{n}$ is the unit vector normal to the middle surface of the blade and $S = S\vec{n}(x,y)$. If we let $m_1 = m_1'/\beta_1'$, this means that the behavior of the blade in the fundamental mode is equivalent to that of a single degree of freedom system of mass m_1, stiffness $K_1 = m_1\omega_1^2$, and loss factor η. Note that β_1' depends on the point x_1,y_1. We can define a parameter β_1 by letting $(x_1,y_1) \equiv (0,0)$, the tip of the blade at the leading edge. Then:

$$\beta_1' = \beta_1 \, \vec{n}(x_1,y_1) \cdot \vec{\phi}_1(x_1,y_1) \qquad (47)$$

34

provided that $|\phi_1(o,o)| = 1$, i.e., the modal function ϕ_1 is normalized. The solution of Equation 44 then becomes:

$$\vec{W} = \frac{S\vec{\phi}_1(x,y)e^{i\omega t}[\vec{n}(x_1,y_1)\cdot\vec{\phi}_1(x_1y_1)]}{m_1[\omega_1^2(1+i\eta)-\omega^2]} \tag{48}$$

For excitation at (o,o) and measurement of the response at (x,y), we then have at resonance:

$$|W| = \frac{S|\phi_1(x,y)|}{|i\eta m_1\omega_1^2|} \tag{49}$$

$$\therefore |\phi_1(x,y)| = (|\frac{\ddot{W}}{S}|\eta) \tag{50}$$

This means that we can measure the normal mode ϕ_1 (or any other mode) by determining $|\ddot{W}/S|$ for excitation at any fixed point and pickup at the point x,y and then multiplying by η. If η is not constant for all measurements (as a result of extraneous sources of hysteretic damping such as cables), then Equation 50 allows one to compensate for this source of error. Note that η can be measured by the "half-power bandwidth" method, so that one can actually determine m_1 directly from the peak value of $|\ddot{W}/S|$ at resonance, using Equation 49, if the measurement chain is properly calibrated.

SECTION III

ANALYSIS OF BLADE RESPONSE WITH SLIP AT A PLATFORM

1. INTRODUCTORY REMARKS

Compressor and turbine blade failures caused by excessive vibration can and often do arise in jet engines whenever high flow-induced excitation forces, high static stresses, and low modal damping levels occur at the same time. While blade/disk interactions will complicate the response behavior of each individual blade, and cause circumferentially changing peak stress levels around the disk, it is slip at the blade/disk interface which provides a major mechanical source of damping. in addition to the aerodynamic and material sources. Attempts to increase slip damping, by means of mid-span or tip shrouds, or by means of mechanical connections between adjacent blades, have not been very successful, perhaps because of the tendency for corresponding points on neighboring blades to vibrate with only relatively small amplitude and phase differences except where extreme efforts are made to mistune adjacent blades relative to each other, i.e., the effect is usually to stiffen rather than dissipate energy. Certainly, the analytical difficulties of predicting the response of complete blade/disk systems with slip at each blade/disk interface, or between each blade, are formidable (References 12, 19) and will not be addressed. We shall examine a configuration in which each blade will slip relative to the disk rather than relative to neighboring blades. With proper attention paid to the static and dynamic forces involved, such a configuration can lead to high slip damping even at high rotational speeds. The response behavior of such a system is highly nonlinear, so we shall assume that the compliance of the disk is infinite, as a first approximation, in order to make the analysis more tractable. Figure 35 shows such a blade concept, as compared with a simple dovetail root and a Christmas tree root. The gap between the outer step of the blade root and the disk is very important, since it must close only at the selected rotational speed above which some damping is required.

2. ANALYSIS OF DYNAMIC RESPONSE

In order to model the dynamic response behavior of the blade in a
single mode, usually the first, different physical models are required
depending on whether slip is or is not occurring at the root or at the
sub-platform. The blade is represented for purposes of analysis as shown
in Figure 36. The various physical models which represent the blade under
different conditions are shown in Figure 37. The parameter β defines
whether slip occurs at the lower dovetail or whether it is locked at this
point, whence $X_2 = 0$; and β_1 defines whether the mass m_3, representing the
sub-platform, is slipping against the disk or is locked in place by the
frictional forces, for which case $X_3 = 0$. The masses m_1, m_2, and m_3
and the stiffnesses k_1 and k_2 must be selected in accordance with the
blade geometry. The disk impedance is assumed to be much greater than
that of the blade, for simplicity.

By experimental or analytical (e.g. finite element) methods, one
can determine the ratio of the response at any point j to the force
applied at any point i, i.e., the compliance $G_{ij}(\omega)$, and this data is
then used either directly in a modal analysis or indirectly to determine
m_1, m_2, m_3, and k_1, k_2 for the discrete element model. Both methods
should give comparable results if the respective assumptions and
simplifications are consistent, but the discrete element model is the
easiest to analyze. For the model, in Figure 38 the equation of motion
can be represented for all cases by the equations:

$$m_1\ddot{X}_1 + k\left[X_1 + \frac{n}{\omega}\dot{X}_1 - \left(X_2 + \frac{n}{\omega}\dot{X}_2\right)\left(\frac{1 - \text{sgn}(\Omega - \Omega_0)}{2}\right)\right] +$$

$$+ k_1\left(\frac{\text{sgn}(\Omega - \Omega_0) + 1}{2}\right)\left[\frac{k}{k_2}\left(X_1 + \frac{n}{\omega}\dot{X}_1\right) - \left(X_3 + \frac{n}{\omega}\dot{X}_3\right)\right]$$

(51)

$$= S \cos \omega t$$
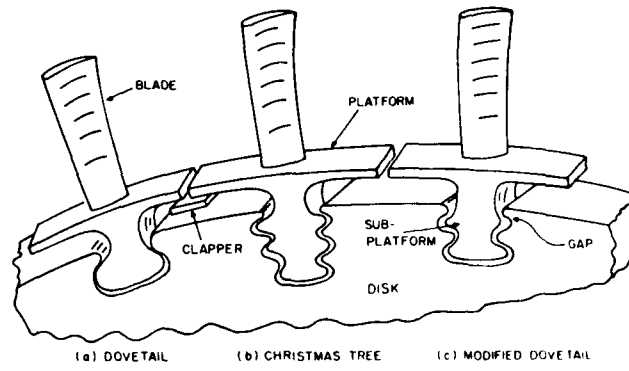
Figure 36. Some Blade Root Geometries
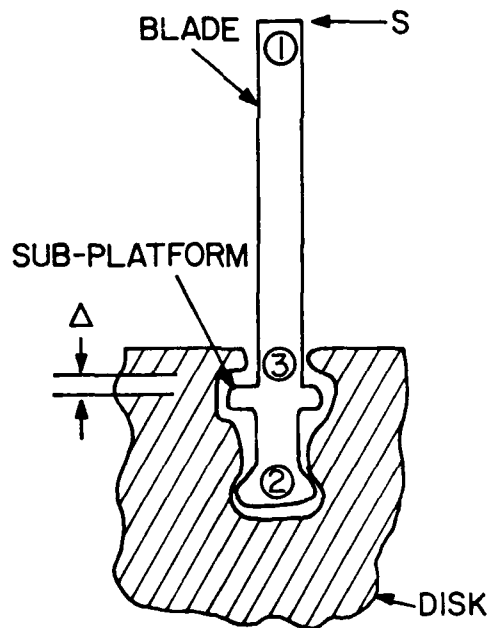
Figure 37. Blade Model

38
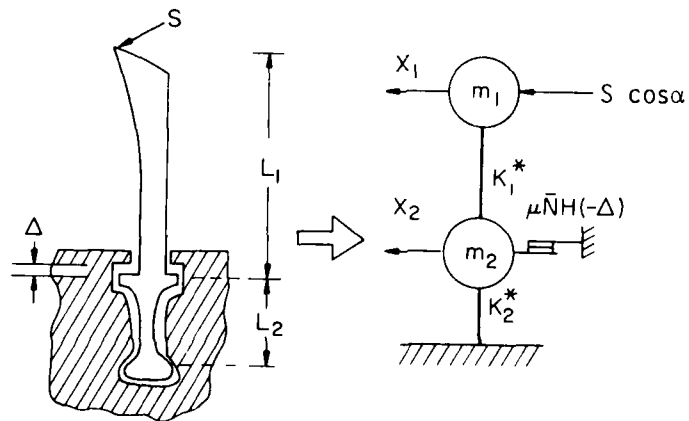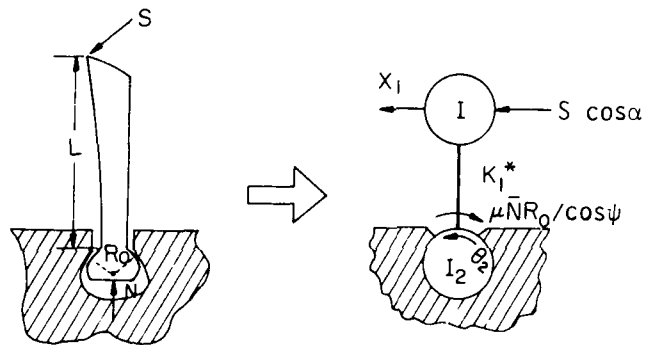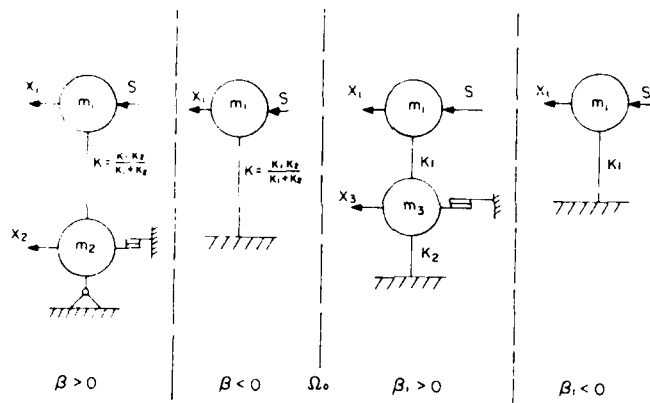
Figure 38. Blade Modelization

$$\left\{ m_2\ddot{X}_2 + \mu NR \text{ sgn } \dot{X}_2 + k \left[\frac{\eta}{\omega} (\dot{X}_2 - \dot{X}_1) - X_1 \right] \right\} (1 + \text{sgn } \beta) \cdot$$

$$\cdot \left(1 - \text{sgn } (\Omega - \Omega_0) \right) + 4k\ X_2 = 0 \qquad (52)$$

$$\left[\left\{ m_3\ddot{X}_3 + \mu N_1 R_1 \text{ sgn } \dot{X}_3 + k_1 \left[\frac{\eta}{\omega} (\dot{X}_3 - \dot{X}_1) - X_1 \right] + k_2 \frac{\eta}{\omega} \dot{X}_3 \right\} (1 + \text{sgn } \beta_1) \right.$$

$$\left. + 2(k_1 + k_2)\ X_3 \right] \left[1 + \text{sgn } (\Omega - \Omega_0) \right] = 0 \qquad (53)$$

where
$$k = k_1 k_2 / (k_1 + k_2) \qquad (54)$$

is the equivalent stiffness, m_1, m_2, and m_3 are masses, k_1 and k_2 are sub-stiffnesses, η is the blade loss factor, S and ω are the amplitude and frequency respectively of the exciting force, μ is the dry friction coefficient, N and N_1 are the normal loads between the blade root and the disk, R and R_1 are coefficients depending on the root geometry (References 17, 18) β, β_1 are coefficients of the slip thresholds. If we let Ω_0 be the rotational speed at which the gap $\Delta \rightarrow 0$, then different solutions occur, depending on whether $\Omega < \Omega_0$ or $\Omega \geq \Omega_0$.

a. Case 1, $\Omega < \Omega_0$, $\beta > 0$

The analysis is the same, essentially, as that for a blade with a simple dovetail root (Equations 17, 18).

Equations 51 to 53 reduce to:

$$m_1 X_1 + \frac{k\eta}{\omega} (\dot{X}_1 - \dot{X}_2) + k(X_1 - X_2) = S \cos \omega t \qquad (55)$$

$$m_2\ddot{X}_2 + \mu NR \text{ sgn } \dot{X}_2 + \frac{k\eta}{\omega} (\dot{X}_2 - \dot{X}_1) - kX_1 + 2kX_2 = 0 \qquad (56)$$

We look for an approximate steady state harmonic solution of the nonlinear Equations 55 and 56 in the form:

$$X_1(t) = D \cos (\omega t + \gamma - \delta) \text{ and } X_2(t) = A \cos (\omega t + \gamma) \qquad (57)$$

This is accomplished by expanding the function $\text{sgn}[-A\omega\sin(\omega t + \gamma)]$ in a Fourier series and retaining the first term only (Reference 16). The following results are obtained for the amplitude A and the phase γ.

$$A = \frac{-\alpha\phi_2 + \sqrt{\phi_1 \, S^2 + \alpha^2(\phi_2^2 - \phi_1\phi_3)}}{\phi_1} \tag{58}$$

$$D = \sqrt{[A^2(1 - \nu m_2/m_1)^2 + (A\eta + \alpha/k)^2]/(1 + \eta^2)} \tag{59}$$

$$\gamma = \arctan \frac{A\nu m_2\eta - \alpha(1 - \nu + \eta^2)}{A\omega^2[\nu m_2 - (1 + \eta^2)(m_1 + m_2)] - \eta\alpha\nu} \tag{60}$$

$$\delta = \arctan \frac{A\eta m_2\omega^2 + \alpha}{A m_2\omega^2 - Ak(1 + \eta^2) - \eta^2} \tag{61}$$

where: $\phi_1 = \omega^4[(m_1 + m_2 - \nu m_2)^2 + \eta^2(m_1 + m_2)^2]/(1 + \eta^2)$ (62)

$\phi_2 = \eta k\nu^2 /(1 + \eta^2)$ (63)

$\phi_3 = [(\nu - 1)^2 + \eta^2]/(1 + \eta^2)$ (64)

$\alpha = 4\mu N \, R/\pi$

$\nu = m_1\omega^2/k = (\omega/\omega_1)^2$

The solution (Equation 57) with amplitude A, expression (Equation 58), exists when $S/\alpha > \sqrt{\phi_3}$. From this we can define the coefficient of the slip threshold as:

$$\beta = S/\alpha - \sqrt{\phi_3} \tag{65}$$

When $\eta = 0$, the nonlinear equations (Equations 58 and 59) reduce further to the very simple form (Reference 17)

$$\left|\frac{A}{S}\right| = \frac{\sqrt{1 - (\alpha/S)^2 (1 - \nu)^2}}{k \ (\omega/\omega_1)^2 \left|1 + m_2/m_1 - \nu m_2/m_1\right|} \tag{66}$$

$$\left|\frac{D}{S}\right| = \frac{1}{k} \sqrt{\frac{1 - (\alpha/S)^2 (1 - \nu)^2 (1 - \nu m_2/m_1)^2}{(\omega/\omega_1)^4 (1 + m_2/m_1 - \nu m_2/m_1)^2} + \left(\frac{\alpha}{S}\right)^2} \tag{67}$$

In these equations R depends on the blade and root geometry. For example, in the earlier investigations for a twisted blade of length L, twist angle α' between root and tip, dovetail angle ψ and dovetail radius R_o, it was shown that:

$$R = R_o \cos \psi/L$$

and that S should be replaced by S cos α'.

b. Case 2, $\Omega < \Omega_o$, $\beta \leq 0$

In some range of the parameters, i.e., when $\beta \leq 0$, the solution (Equation 57) does not exist. This corresponds to the domain of existence of the linear solution for the one-mass system. In this case, Equations 51 to 53 become:

$$m_1 \ddot{X}_1 + K(X_1 + \frac{\eta}{\omega} \dot{X}_1) = S \cos \omega t \tag{68}$$

$$X_2 = 0 \tag{69}$$

The solution of Equation 68 is:

$$X(t) = D^* \cos (\omega t - \delta^*) \tag{70}$$

with

$$D^* = S/k\sqrt{(1 - \nu)^2 + \eta^2} \tag{71}$$

and

$$\delta^* = \arctan \eta/(1 - \nu) \tag{72}$$

42

c. Case 3, $\Omega < \Omega_o$, $\beta_1 > 0$

Slip now occurs at the mass m_3 and ceases to occur at the mass m_2, which becomes "locked" at high rotation speeds. The slip at the mass m_3 can contribute significant amounts of damping if the term $\mu N_1 R_1$ in Equation 53 can be made to remain relatively small through proper control of the blade root geometry.

The equations now take the form:

$$m_1 \ddot{X}_1 + K_1\left(\frac{\eta}{\omega} \dot{X}_1\right) + X_1 - K_1\left(\frac{\eta}{\omega} \dot{X}_3 + X_3\right) = S \cos_\omega t \tag{73}$$

$$m_3 \ddot{X}_3 + K_1\left[\frac{\eta}{\omega}(\dot{X}_3 - \dot{X}_1) + (X_3 - X_1)\right] +$$

$$+ K_2\left(\frac{\eta}{\omega} \dot{X}_3 + X_3\right) + \mu N R_1 \operatorname{sgn}\dot{X}_3 = 0 \tag{74}$$

The solution of these equations is written in the form:

$$X_1 = D_{II}\cos(\omega t + \gamma_{II} - \delta_{II}) \text{ and } X_3(t) = A_{II}\cos(\omega t + \gamma_{II}) \tag{75}$$

Then, again by the method of harmonic balance, it can be shown that:

$$A_{II} = \frac{-\alpha_1 \phi_5 + \sqrt{\phi_4 S^2 + \alpha_1^2(\phi_5^2 - \phi_4 \phi_5)}}{\phi_4} \tag{76}$$

$$D_{II} = \sqrt{\frac{A_{II}^2(1 + k_2/k_1)^2 + [A_{II}\eta(1 + k_2/k_1) + \alpha_1/k_1]^2}{(1 + \eta^2)}} - \nu_1 m_3/m_1 \tag{77}$$

$$\gamma_{II} = \arctan \frac{A_{II}\nu_1 m_3 \eta - \alpha_1(1 - \nu_1 + \eta^2)}{A_{II}\omega^2[\nu_1 m_3 - (1 + \eta^2)(m_1 + m_3) - \eta\alpha_1\nu_1]} \tag{78}$$

$$\delta_{II} = \arctan \frac{A_{II}\eta m_3 \omega^2 + \alpha_1}{A_{II}m_3\omega^2 - A_{II}K_1(1 + \eta^2) - \eta\alpha_1} \tag{79}$$

$$\phi_4 = \left(\frac{\nu_1 m_3 \omega^2}{1 + \eta^2} - k_2\right)^2 \eta^2 + \left[\frac{\nu_1 m_3 \omega^2}{1 + \eta^2} + k_2(1 - \nu_1) - \omega^2(m_1 + m_3)\right]^2 \quad (80)$$

$$\phi_5 = \eta[\nu_1^2 k_1 + k_2\{(1 - \nu_1)^2 + \eta^2\}]/(1 + \eta^2) \quad (81)$$

$$\phi_6 = [(\nu_1 - 1)^2 + \eta^2]/(1 + \eta^2) \quad (82)$$

$$\alpha_1 = 4\mu N_1 R_1/\pi \quad (83)$$

$$\nu_1 = m_1 \omega^2/k_1 = (\omega/\omega_{11})^2 \quad (84)$$

The solution (Equation 75) exists when $S/\alpha_1 > \sqrt{\phi_3}$. From this we define the appropriate coefficient β of the slip threshold by:

$$\beta = S/\alpha_1 - \sqrt{\phi_3} \quad (85)$$

d. Case 4, $\Omega > \Omega_0$, $\beta < 0$

In some range of parameters, i.e. $\beta \leq 0$, the solution (Equation 75) does not exist. It corresponds to the linear case, for which the relevant solution is:

$$X_1(t) = D_1^* \cos(\omega t - \delta_1^*) \quad (86)$$

with

$$D_1^* = S/k_1 \sqrt{(1 - \nu_1)^2 + \eta^2} \quad (87)$$

and

$$\delta_1^* = \arctan \eta/(1 - \nu_1) \quad (88)$$

Figure 39 illustrates a graphical method for constructing the solution from these equations, for the case $\eta = 0$. In this figure, note that:

$$\frac{\omega_{1,2}^*}{\omega_{11}} = \frac{1}{\sqrt{2}}\left\{\frac{m_1}{m_3}\left(1 + \frac{k_2}{k_1}\right) + 1 \pm \sqrt{\left[\frac{m_1}{m_3}\left(1 + \frac{k_2}{k_1}\right) + 1\right]^2 - 4\frac{m_1 k_2}{m_3 k_1}}\right\}^{1/2} \quad (89)$$

44
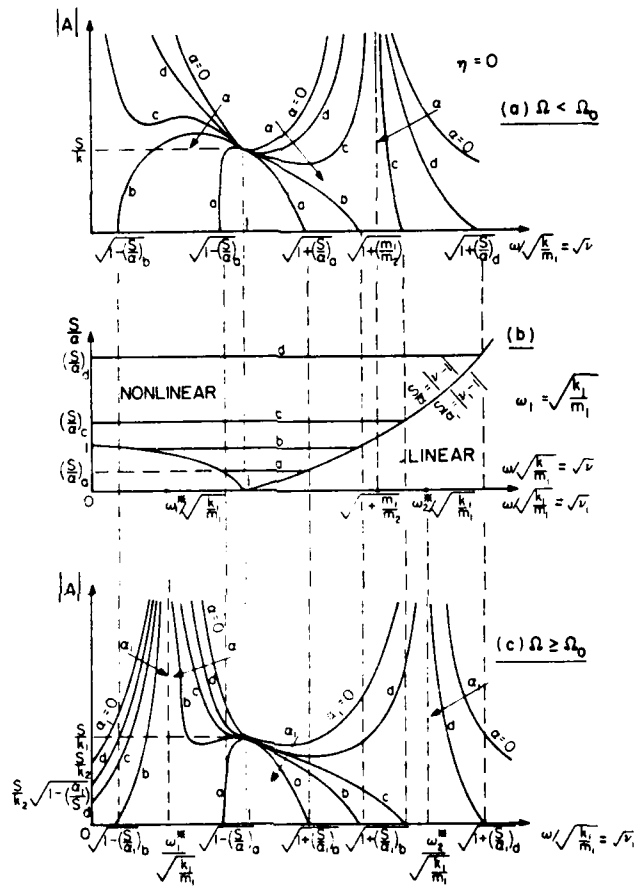
Figure 39.   Graphical Construction of
Response Solution

Figure 39 illustrates clearly the regions of existence of the nonlinear solutions ($|A| \neq 0$) for various values of S/α_1. When $\eta = 0$ and $m_3 = 0$, the solution further simplifies to:

$$\left|\frac{A_1}{S}\right| = \frac{\sqrt{1 - (\alpha_1/S)^2(1 - \nu_1)^2}}{(k_1 + k_2)\left|k/k_1 - \nu_1 - \nu_1(m_3/m_1)(k/k_2)(1 - \nu_1)\right|} \tag{90}$$

$$\left|\frac{D_1}{S}\right| = \frac{1}{k_1}\sqrt{\frac{[1 - \nu_1(k/k_2)(m_3/m_1)]^2[1 - (\alpha_1/S)^2(1 - \nu_1)^2]}{[k/k_1 - \nu_1 - \nu_1(m_3/m_1)(k/k_2)(1 - \nu_1)]^2} + \left(\frac{\alpha_1}{S}\right)^2} \tag{91}$$

where it is recognized that $\nu_1 = \omega^2/\omega_{11}^2$ and $\omega_{11} = \sqrt{k_1/m_1}$. For most practical cases $R_1 \ll 1$ in these equations and for a twisted blade, we replace S by S cos α'. We now have a formal solution for the cases $\Omega < \Omega_0$ and $\Omega \geq \Omega_0$, and a numerical example will be discussed after a review of the static blade behavior. Finally, note that the problem addressed here is quite similar to that discussed by Williams and Earles (Reference 3).

3. ANALYSIS OF QUASI-STATIC BEHAVIOR

Referring to Figure 40, the radial movement Y of the sub-platform under the action of the centrifugal load $WR_D\Omega^2$ due to the outboard part of the blade will be less than the gap Δ up to the speed Ω_0 where:

$$\Omega_0 = \sqrt{k_D\Delta/WR_D} \tag{92}$$

where R_D is the average radius of the blade relative to the rotation axis of the disk. When $\Omega > \Omega_0$, the springs k_p will come into play and provide the normal load N_1 on the mass m_3. It is easily seen on the basis of static equilibrium that:

$$N = \frac{WR_D(\Omega^2 - \Omega_0^2)}{1 + k_D/2 \, kp} \tag{93}$$

46

which means that k_D > kp if a significant reduction of the centrifugal loads on the blade is to occur, as is necessary. As an illustration, consider the blade for which the static extensional stiffness k_D of the root below m_3 is provided by a uniform segment of cross-sectional area A_D and length ℓ_D. Then:

$$k_D = E \ A_D/\ell_D \tag{94}$$

Similarly, if each spring k_p is considered to be represented, as an approximation, by a cantilever beam of length ℓ_p, thickness h_p and breadth b_p, then:

$$k_P = 3 \ E \ b_P h_P^3/12\ell_P^3 \tag{95}$$

For $\Omega < \Omega_0$, the normal load N on the mass m_2 is given by:

$$N = W \ R_D\Omega^2 \tag{96}$$

Table 2 gives a calculator program to predict the blade response with slip at the platform.
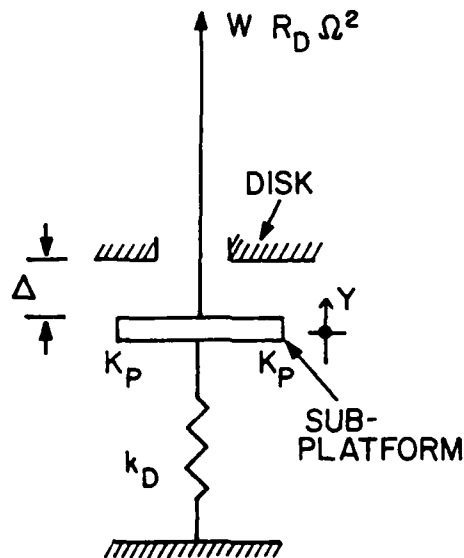
Figure 40. Quasi-Static Model

47

TABLE 2

HP 67 PROGRAM FOR BLADE WITH SLIP AT PLATFORM

<u>Input:</u> Put ω in X register (Hz); press A, B, C, D in sequence.

<u>Manual Storage:</u> Storage Location I - n_1
Storage Location 0 - m_1, (Kg)
Storage Location 1 - K_1, (N/m)
Storage Location 2 - K_2, (N/m)
Storage Location 4 - α_1/S
Storage Location 5 - S cos α

<u>Output:</u> Label A - $|X_1|$ linear ($\alpha_1/S = \infty$) (Equation 87)

Label B - $|X_1|$ linear ($\alpha_1/S = 0$) (Equation 71)

Label C - $|X_1|$ slip (Equation 90)

Label D - $|X_2|$ slip (Equation 91)

<u>Internal Storage:</u> Storage Location 6 ω^2 (rad/sec)
Storage Location 7   K
Storage Location 8 $(\omega/\omega_1)^2$
Storage Location A $1 - (\alpha_1/S)^2 (1-\omega^2/\omega_1^2)^2$

<u>Program:</u>

fCL PRGM	×	RCL 6	×	1	RCL 5
fLBLA	gx^2	RCL 0	hRTN	+	×
2	RCL E	×	fLBL C	STO A	RCL 1
×	+	CHS	RCL 1	RCL 7	÷
hπ	f$\sqrt{x}$	RCL 7	RCL 0	RCL 1	hRTN
×	h 1/x	+	÷	÷	fLBL D
gx^2	RCL 5	gx^2	h 1/x	RCL 8	RCL 7
STO 6	×	STO E	RCL 6	-	RCL 5
RCL 0	hRTN	RCL 1	×	gx^2	×
×	fLBL B	hRC I	STO 8	h 1/x	RCL 1
CHS	RCL 1	×	CHS	RCL A	÷
RCL 1	h 1/x	gx^2	1	×	RCL 2
+	RCL 2	RCL E	+	STO B	÷
gx^2	h 1/x	+	RCL 4	RCL 4	RCL B
STO E	+	f$\sqrt{x}$	×	gx^2	f$\sqrt{x}$
RCL 1	h 1/x	h 1/x	gx^2	+	×
hRC I	STO 7	RCL 5	CHS	f$\sqrt{x}$	hRTN

4. NUMERICAL ILLUSTRATION

The equations derived in this section permit one to predict the effects of rotational speed on the dynamic response of any blade provided that one knows the modal masses and stiffnesses, and the exciting forces. Unfortunately, this information is rarely available at the time it is needed. This is especially true of the exciting forces. As an example, the work of Hansen, Meyer and Manson (Reference 2) represents a very interesting early investigation of blade damping as a function of rotation speed. The blade geometry data (Reference 2) indicates that they used a rectangular section blade of length 50.8mm (2 inches), breadth 15.3mm (0.602 inches), width 1.83mm (0.072 inches) at the tip and 3.05mm (0.120 inches) at the root. The root was cylindrical, of diameter 7.87mm (0.310 inches). In the tests, the blade was attached, alone, in a 33 cm (13 inch) diameter disk and excited by impacting it with a falling steel ball. Although the results are very interesting and useful, it is diffi-cult to obtain accurate excitation force data from this source.

Ewins (Reference 20) recently described a test system in which air jets were used as a means of exciting the blades. The test results indi-cate good qualitative agreement between linear analysis and experiment for several tuned and untuned blades in a flexible disk, but no estimate of the exciting forces is given directly. Other investigators (References 14, 21) are equally uninformative as far as this aspect of the problem is con-cerned. References 22-24 do seem to address the question to some extent.

The cyclic forces acting on a rotating blade-disk system arise as the blades cut through a quasi-stationary airflow pattern generated by the fixed blades (vanes) ahead of them. The stationary pressure field along a circular path through the center of each stationary vane possesses a mini-mum between each vane and a maximum at each vane station, as illustrated in Figure 41. If the number of fixed vanes is n, then the rate of repe-tition of the pressure pulses crossing each rotating blade is $n\Omega/60$ Hz, if Ω is the rotation speed in rpm. A Fourier expansion of this repeating pulse then gives:

$$S(t) = S(V,\Omega) \sum_{m=1}^{\infty} a_m \cos(mn\Omega t/60) \qquad (97)$$
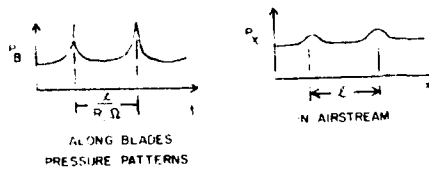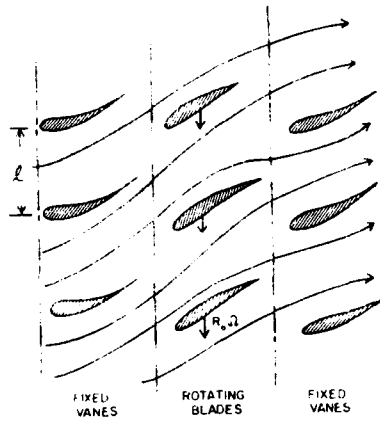
Figure 41. Flow Induced Loads

where $a_m \simeq 1$ if the pulses are sharp. The amplitude $S(V,\Omega)$ depends on the mean velocity V of the airflow through the stage, which in turn depends on the power setting of the engine, as well as the rotation speed Ω. It is not easy to determine $S(V,\Omega)$ analytically and little experimental data from industrial sources seem to have been published. So we shall consider only a few "typical" cases in this section in order to illustrate the effect of this important parameter on the blade response. Each term of Equation 47 gives rise to a possible excitation of a blade mode, and a typical Campbell diagram is constructed by plotting the frequencies $mn\Omega/60$ against Ω for various values of m, along with the blade resonant frequencies ($f_i = 1,2$) as a function of Ω, as illustrated in Figure 42. As is seen, the fundamental mode is excited by the blade passage excitation when Ω is such that $f_1 = 1\ n\Omega/60$ (nth engine order, point A), by the second harmonic (2nth engine order) when $f_1 = 2\ n\Omega/60$ (point B) and so on. The Campbell diagram is a useful means for estimating where the vibration problems are likely to occur, but it gives no clue as to excitation force magnitudes.

We shall now examine a specific blade geometry, considered in previous investigations (References 17, 18) and representing a typical low pressure compressor blade. The main dimensions of this blade are:

$$L = 20 \text{ cm}$$

$$W = 0.20 \text{ kg} \ (0.44 \text{ lb})$$

The other relevant magnitudes are given in the nomenclature, as specific numbers associated with the relevant symbols. From these numbers we see from Equations 94, 95, 92, 93, and 96 in succession that:

$$k_D = 2.10 \times 10^9 \text{N/m} \ (1.2 \times 10^7 \text{ lb/in})$$

$$k_p = 2.1 \times 10^7 \text{N/m} \ (1.2 \times 10^5 \text{ lb/in})$$

$$\Delta = 0.057 \text{ mm} \ (0.00225 \text{ ins})$$

$$N_1 = 1.856 \times 10^{-6} \ (\Omega^2 - \Omega_o^2) \text{ lbf}$$

$$N = 8.342 \times 10^{-4} \Omega^2 \text{Newton} (1.875 \times 10^{-4} \Omega^2 \text{ lbf})$$

with $\quad \Omega_o = 12000 \text{ rpm}$
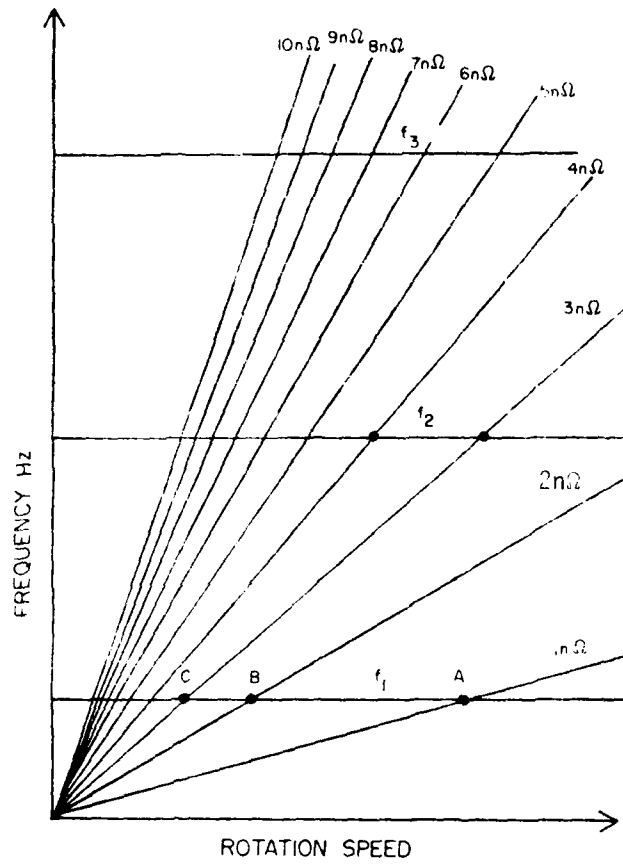
Figure 42.   Campbell Diagram

From Equations 68, 69, 90, and 91 we can then calculate the response of the blade for the cases $\Omega < \Omega_0$ and $\Omega \geq \Omega_0$. Some results are shown in Figures 43 to 46. From these we can then determine the apparent modal damping η_1', defined by the "half power bandwidth" method, and plot against α/S (for $\Omega < \Omega_0$) or α_1/S (for $\Omega \geq \Omega_0$). The results for this particular blade are shown in Figure 47. It is seen that, for $\Omega < \Omega_0$, η_1 increases rapidly as α/S falls and reaches a very high maximum value before finally falling to zero as $\alpha/S \to 0$, i.e. $\Omega \to 0$. On the other hand for $\Omega \geq \Omega_0$, the damping rapidly increases as α_1/S rises above a threshold level (below which a new peak occurs at lower frequency and with low damping), reaches a peak of about 0.20, and then drops more slowly as α_1/S increases further.

From the values of N and N_1 given earlier, we can then calculate α/S and α_1/S for any assumed values of S. We shall consider two cases namely (i) $S = 22.24$ N (5 lbf) and (ii) $S = 1.69 \times 10^{-6} \, \Omega^{3/2}$ $(= 3.8 \times 10^{-6} \, \Omega^{3/2}$ lbf), with Ω in rpm. The first represents a constant force, as in Hanson, Meyer and Manson's experiments (Reference 2) and the second represents a more likely situation in which S increases as Ω increases, e.g. $S = 22.24$ N (5 lbf) at 12000 rpm, 31.14 N (7.0 lbf) at 15000 rpm, and 5.96 N (1.34 lbf) at 5000 rpm. Tables 2 and 3 show typical calculated values of α/S, α_1/S, and η_1'. The appropriate expressions for α/S and α_1/S are:

(i) <u>$S = 22.2$ N(5 lbf)</u>

$$\frac{\alpha}{S} = \frac{4 \mu N \, R_0}{\pi S \, L \cos \alpha' \, \cos \psi} = \frac{4 \times 0.15 \times 1.875 \times 10^{-4} \Omega^2 \times 1}{20 \times \pi \times 5 \times 0.724 \times 0.5}$$

$$= 9.89 \times 10^{-7} \Omega^2$$

$$\frac{\alpha_1}{S} = \frac{4 \mu N_1}{\pi S \cos \psi} = \frac{4 \times 0.15 \times 1.856 \times 10^{-6} (\Omega^2 - \Omega_0^2)}{\pi \times 5 \times 0.724}$$

$$= 9.79 \times 10^{-8} (\Omega^2 - \Omega_0^2)$$

(ii) $\underline{S = 1.69 \times 10^{-5}\Omega^{3/2} \text{ Newton } (3.8 \times 10^{-6} \, \Omega^{3/2} \text{lbf})}$

$$\frac{\alpha}{S} = \frac{4\mu N \, R_o}{S\pi L \cos\alpha' \, \cos\psi} = \frac{4 \times 0.15 \times 1.875 \times 10^{-4}\Omega^2 \times 1}{20 \times \pi \times 3.8 \times 10^{-6} \, \Omega^{3/2} \times 0.724 \times 0.5}$$

$$= 1.301 \, \Omega^{1/2}$$

$$\frac{\alpha_1}{S} = \frac{4 \, \mu N_1}{\pi S \cos\alpha'} = \frac{4 \times 0.15 \times 1.856 \times 10^{-6} \, (\Omega^2 - \Omega_o^2)}{\pi \times 3.8 \times 10^{-6}\Omega^{3/2} \times 0.724}$$

$$= 0.1288 \, (\Omega^2 - \Omega_o^2) \, / \, \Omega^{3/2}$$
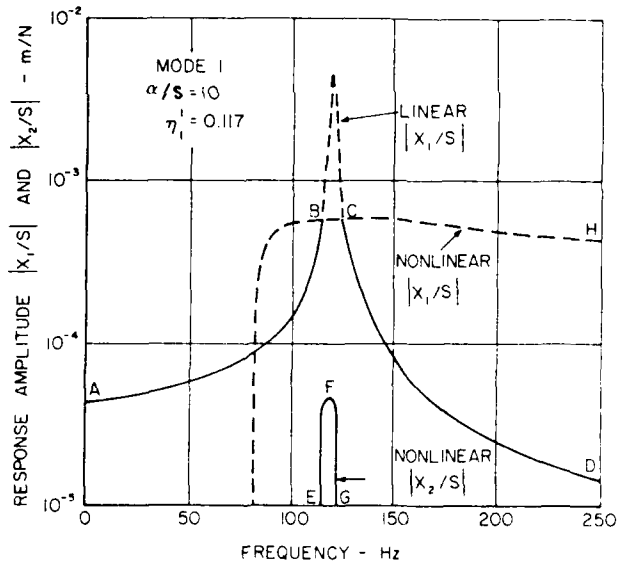
Figure 43.   Blade Response for $\Omega < \Omega_0$, $\beta > 0$

54
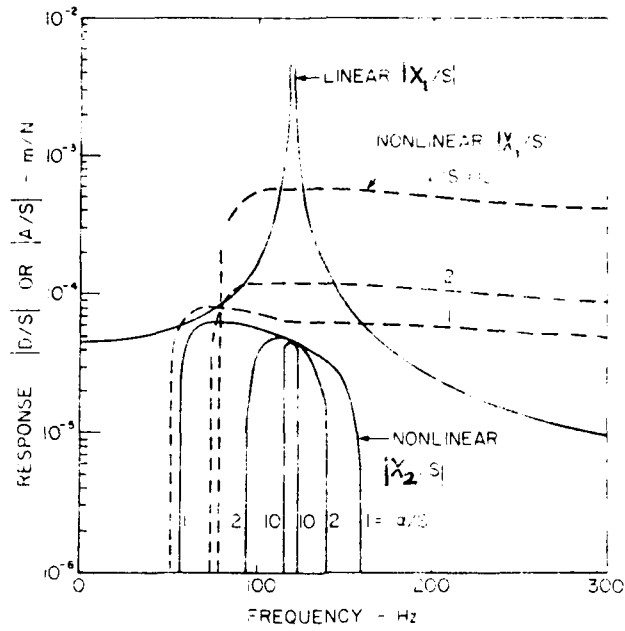
Figure 44. Blade Response for $\Omega < \Omega_0$, $\beta > 0$
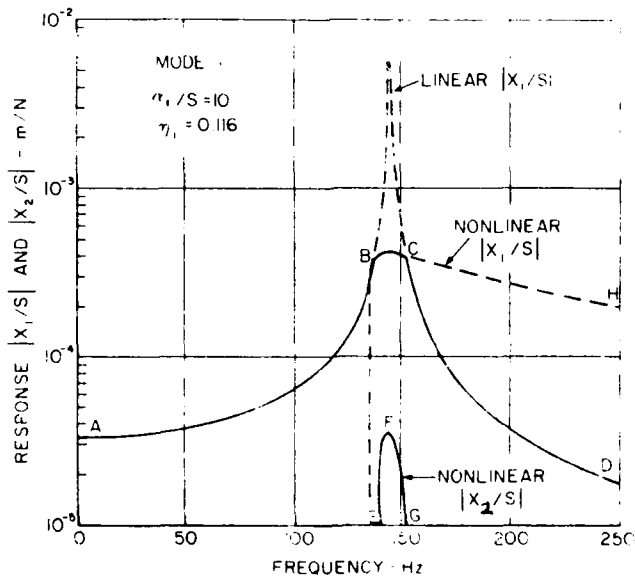
Figure 45. Blade Response for $\Omega > \Omega_0$, $\beta_1 > 0$
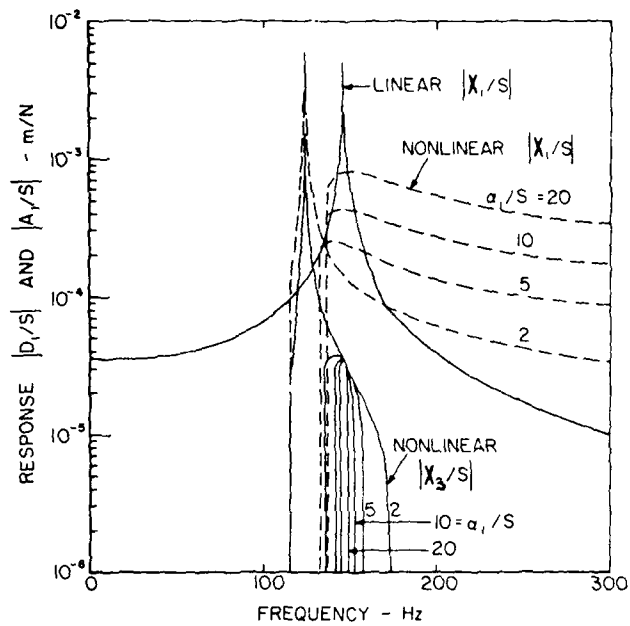
Figure 46.   Blade Response for $\Omega > \Omega_0$, $\beta_1 > 0$
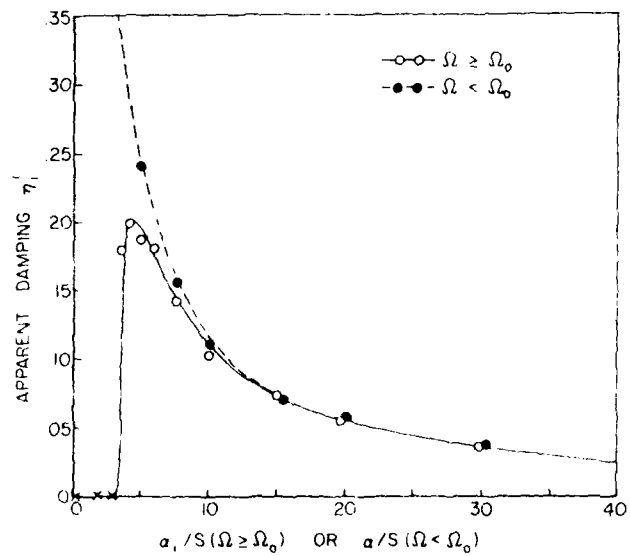
Figure 47.   Modal Damping versus α/S or α_1/S

TABLE 3

DAMPING VERSUS ROTATIONAL SPEED

DAMPING VERSUS Ω FOR S = 22.24N (5 LBF)

RPM	$\Omega < \Omega_o$		$\Omega \geq \Omega_o$	
	α/s	η_1'	α_1/s	η_1'
0	0	–	–	–
100	0.0099	–	–	–
500	0.247	–	–	–
1000	0.989	–	–	–
2000	3.96	0.295	–	–
3000	8.90	0.130	–	–
4000	15.83	0.070	–	–
5000	24.7	0.042	–	–
6000	35.6	0.028	–	–
7000	48.5	0.021	–	–
8000	63.2	0.016	–	–
9000	80.1	0.012	–	–
10000	98.9	0.010	–	–
12000	142.5	0.010	0	0
13000	–	–	2.45	0.010
14000	–	–	5.09	0.187
15000	–	–	7.93	0.140
16000	–	–	10.96	0.100
17000	–	–	14.2	0.076
18000	–	–	17.6	0.062
19000	–	–	21.2	0.050
20000	–	–	25.1	0.042

DAMPING VERSUS Ω FOR S = $1.69 \times 10^{-5} \, \Omega^{3/2}$ N

Ω RPM	$\Omega < \Omega_o$		$\Omega \geq \Omega_o$	
	α/s	η_1'	α_1/s	η_1'
0	0	–	–	–
100	13.0	0.086	–	–
500	29.1	0.034	–	–
1000	41.1	0.024	–	–
2000	58.1	0.017	–	–
3000	71.2	0.014	–	–
5000	91.9	0.011	–	–
10000	130	0.01	–	–
12000	–	–	0	0.01
13000	–	–	2.18	0.01
14000	–	–	4.04	0.20
15000	–	–	5.68	0.18
16000	–	–	7.13	0.155
17000	–	–	8.43	0.13
18000	–	–	9.60	0.112
19000	–	–	10.67	0.102
20000	–	–	11.66	0.095

Figure 48 shows the variation of n_1' with Ω for these cases. It is seen that high damping occurs at high speed, as expected. Obviously, the particular numerical values can be changed to represent other conditions, but the approach and general behavior remain the same. One other possibility can be examined, namely a blade of the type having a hinged root with mating surfaces now parallel to the plane of rotation of the root, and discussed also by Hanson, Meyer, and Manson (Reference 2). For this type of blade, N_1 remains just about constant at all speeds, while the force S changes, usually increasing as Ω increases. This would account for the high damping achieved by this type of blade, since α_1 would be nearly constant and α_1/S would change in such a way that n_1' would increase as Ω increases.
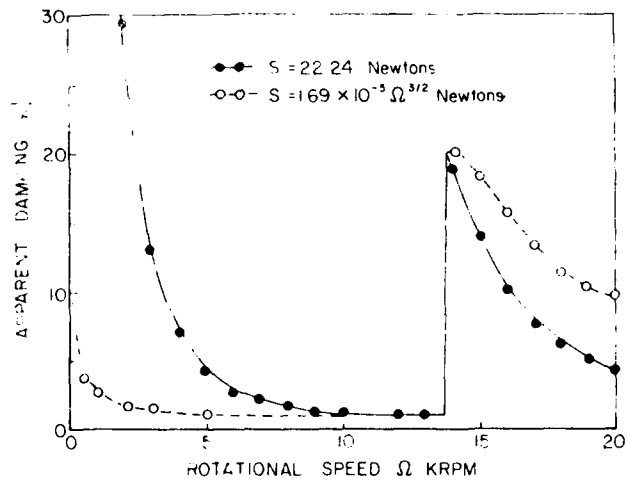
Figure 48. Modal Damping versus Rotational Speed

SECTION IV

HARMONIC RESPONSE OF A DAMPED TWO-DEGREE OF FREEDOM
SYSTEM WITH GAPS

1.   INTRODUCTORY REMARKS

In this section, a two mass mechanical system excited by an external
harmonic force is considered. One of the masses is assumed to move in
the space between two elastic non-inertial buffers. The gaps introduce
a high degree of nonlinearity into the system. The motion of the two
masses is damped by dry friction which also brings nonlinear effects and
hysteretic damping of the elastic members. An approximate steady state
solution is found for the harmonic response case. A graphical method
is adapted for construction of response (amplitude versus frequency)
curves. Numerical examples show the influence of various parameters,
such as amplitude of the exciting force, dry friction, hysteretic damping,
fluid pumping, and elasticity of the buffers on the amplitude of the
response. This section summarizes Reference 16.

It is generally very difficult to predict the dynamic behavior of a
mechanical assembly having gaps between the members, whether introduced
for specific reasons or resulting from wear. In fact, the motion of
systems with gaps is highly nonlinear and is very sensitive to the gap
dimensions and the values of the excitations (Reference 25).

The present section considers the response of a damped two degree
of freedom system with gaps, excited by a harmonically varying force.
The model of the system is based on a modelization of blades in a disc.
Damping in the system is introduced by dry friction between one of the
masses and the supporting environment, hysteretic damping accompanying
motion of the elastic members and fluid pumping in gaps.

A combined analytical-graphical method is adopted for determining
the response curves, the amplitude-frequency relationship. This allows
one to determine the steady state response of the system for various
values of the important parameters, particularly gaps, damping, friction,
and excitation.

2. MODEL OF THE SYSTEM

The idealized model of the system is illustrated in Figure 49. The system consists of two rigid bodies of mass M_1 and M_2 joined by a plane linear spring of rigidity k_1 and two linear buffer springs of rigidity k_2. Assumptions made in the analysis are: (i) the system is symmetric and plane, (ii) the masses of the buffers are negligible, and (iii) the body M_2 moves horizontally only, while the body M_1 performs plane motion. The external exciting force $S \cos (\omega t - \gamma)$ is applied to the body M_1. During the motion of the body M_2 a dry friction force arises, modelled by Coulomb's law ($F = \mu N$, where μ is the coefficient of friction and N the normal force). When the amplitude of motion of the body M_2 is greater than the gap Δ, the springs k_2 exert a force. The remaining damping terms in the system are linear. For small motions of the bodies, the equations of motion of the system are:

$$M_1 \; (R\ddot{\psi}+\ddot{X}) + \frac{\alpha_{\psi h}}{\omega} \; (\dot{\psi}+ \frac{\dot{X}}{R}) + k_1\psi = S \cos (\omega t-\gamma) \tag{98}$$

$$M_2\ddot{X} + \alpha_x\dot{X} + \left[\frac{\alpha_{xh}}{\omega} \dot{X} + k_2(x-\Delta) \right] \psi$$

$$-k_1\psi + \mu\bar{N} \; \text{sgn} \; (\dot{X}) = 0, \tag{99}$$

where

$$\psi = \frac{1}{2} \; [1+\text{sgn} \; (|X| - \Delta)]$$

α_x represents the viscous damping coefficient (e.g., fluid resistance), $\alpha_{\psi h}$, α_{xh} represent the hysteretic damping coefficients (e.g., internal friction in the springs). We will confine attention to the effects of gaps and damping on the response of the system.
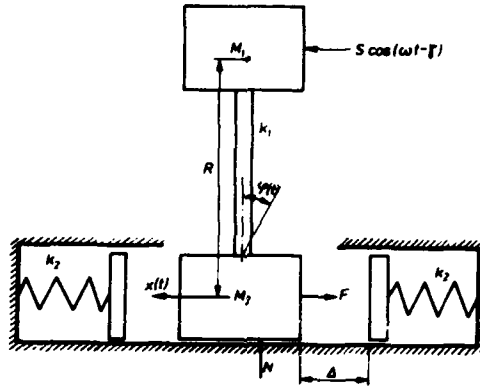
Figure 49. Model of the System

3. STEADY-STATE SOLUTION WITH SLIP

We shall analyze the excited motion only, i.e.:

$$X = A\cos\omega t, \tag{100}$$

where A represents the amplitude of the excited vibration. It depends on the frequency of the exciting force.

Putting Equation 100 into Equation 98 we obtain

$$M_1 R\ddot{\psi} + \frac{\alpha_{\psi h}}{\omega} \dot{\psi} + k_1\psi = S\cos(\omega t - \gamma) +$$

$$+ M_1 A\omega^2 \cos\omega t + \alpha_{\psi h} \frac{A}{R} \sin\omega t \tag{101}$$

The steady-state solution for Equation 101 is

$$\psi(t) = \frac{S}{k_1 \phi_*^2} \left[\left(1 - \frac{M_1 R}{k_1} \omega^2\right) \cos(\omega t - \gamma) + \frac{\alpha_{\psi h}}{k_1} \sin(\omega t - \gamma) \right]$$

$$+ \frac{A}{R\phi_*^2} \left[\left(1 - \frac{M_1 R}{k_1} \omega^2\right) \cos\omega t + \frac{\alpha_{\psi h}}{k_1} \sin\omega t \right] - \frac{A}{R} \cos\omega t \tag{102}$$

61

where

$$\phi_* = \sqrt{\left(1-\frac{M_1 R}{k_1}\,\omega^2\right)^2 + \left(\frac{\alpha_{\psi h}}{k_1}\right)^2}$$

Putting Equations 100 and 102 into Equation 99 we get:

$$A \cos\omega t \left[k_2 \psi^* - M_2 \omega^2 + \frac{k_1}{R} - \frac{k_1^2}{\phi_*^2}\left(\frac{k_1}{R} - \right.\right.$$

$$\left.\left. - M_1 \omega^2\right)\right] - A \sin\omega t \left[\alpha_x \omega + \alpha_{xh}\,\psi^* + \frac{k_1^2 \alpha_{\psi h}}{R\phi_*^2}\right] -$$

$$- k_2 \Delta\Psi^* - \mu\bar{N} \, \text{sgn} \, (A \sin\omega t)\Big] - \frac{S}{k_1 \phi_*^2} \left[(k_1 - \right.$$

$$- M_1 R\omega^2)\cos\,(\omega t - \gamma) + \alpha_{\psi h} \sin\,(\omega t - \gamma) \left.\right] = 0 \qquad (103)$$

where:

$$\psi^* = [1 - \text{sgn}(|A\cos\omega t| - \Delta)]/2 \qquad (104)$$

The values of the function ψ^* are given in Table 4.

We develop the function ψ^*, $\psi^* \cos\omega t$, $\psi^* \sin\omega t$ and sgn $(A \sin\omega t)$ in Fourier series. Limiting attention to the first approximation we have:

$$\psi^* = \frac{\omega}{\pi} \left[\cos\omega t \int_0^{\frac{2\pi}{\omega}} \psi^* \cos\omega t \, dt + \sin\omega t \int_0^{\frac{2\pi}{\omega}} \psi^* \sin\omega t \, dt\right] = 0 \qquad (105)$$

Note that when $\alpha_{\psi h} = 0$, $\phi_* = 1 - M_1 R\omega^2/k_1$.

TABLE 4

VALUES OF THE FUNCTION μ^*

$|A| \leq \Delta$	$|A| > \Delta$				
	$0 < t < t_1$	$t_1 < t < \frac{\pi}{\omega} - t_1$	$\frac{\pi}{\omega} - t_1 < t < \frac{\pi}{\omega} + t_1$	$\frac{\pi}{\omega} + t_1 < t < \frac{2\pi}{\omega} - t_1$	$\frac{2\pi}{\omega} - t_1 < t < \frac{2\pi}{\omega}$
0	1	0	1	0	1

$$t_1 = \frac{1}{\omega} \text{ arc cos } \frac{\Delta}{|A|}$$

63

$$\psi * \cos\omega t = \frac{\omega}{\pi} \left[\cos\omega t \int_{0}^{\frac{2\pi}{\omega}} \psi * \cos^2\omega t\, dt + \sin\omega t \int_{0}^{\frac{2\pi}{\omega}} \psi * \sin\omega t \cos\omega t\, dt \right]$$

$$= \frac{1}{\pi} (2\omega t_1 + \sin 2\omega t_1)\cos\omega t \equiv C(A)\cos\omega t \tag{106}$$

$$\psi * \sin\omega t = \frac{\omega}{\pi} \left[\cos\omega t \int_{0}^{\frac{2\pi}{\omega}} \psi * \sin\omega t \cos\omega t\, dt + \sin\omega t \int_{0}^{\frac{2\pi}{\omega}} \psi * \sin^2\omega t\, dt \right]$$

$$= \frac{1}{\pi} (2\omega t_1 - \sin 2\omega t_1)\sin\omega t \equiv C^*(A)\sin\omega t \tag{107}$$

$$\text{sgn}(A\sin\omega t) = \text{sgn}\, A \frac{\omega}{\pi} \left[\cos\omega t \int_{0}^{\frac{2\pi}{\omega}} \text{sgn}(\sin\omega t)\cos\omega t\, dt \right.$$

$$\left. + \sin\omega t \int_{0}^{\frac{2\pi}{\omega}} \text{sgn}(\sin\omega t)\sin\omega t\, dt \right]$$

$$= \frac{4}{\pi}\, \text{sgn}\, A\, \sin\omega t \tag{108}$$

Putting Equation 105 to Equation 108 into Equation 103 and comparing the coefficients of the trigonometric functions we obtain the basic equation for the resonance curve $A = A(\omega)$. (The same result is obtained if one assumes the solution in the form $x = A\cos\omega t$, $\psi = B\cos\omega t + D\sin\omega t$, where A, B, D are functions of ω).

$$A^2\phi_1(\omega) + [A\phi_2(\omega) + \beta S\phi_*(\omega)\, \text{sgn}\, A]^2 = S^2 \tag{109}$$

and the expression for the phase angle:

$$\gamma = \arctan \frac{\left(\frac{\beta}{M}S\phi_*\text{sgn}A + A\phi_2\right)(k_1 - M_1R\omega^2) + A\alpha_{\psi h}\sqrt{\phi_1}}{\left(\frac{\beta}{M}S\phi_*\text{sgn}A + A\phi_2\right)\alpha_{\psi h} - A(k_1 - M_1R\omega^2)\sqrt{\phi_2}} \qquad (110)$$

where

$$\phi_1(\omega) = \frac{1}{M^2}\left[\phi_*\left(k_2C - M_2\omega^2 + \frac{k_1}{R}\right) - \frac{1}{\phi_*}\left(\frac{k_1}{R} - M_1\omega^2\right)\right]^2 \qquad (111)$$

$$\phi_2(\omega) = \frac{1}{M}\left[\phi_*(\alpha_x\omega + \alpha_{xh}C^*) + \frac{\alpha_{\psi h}}{R\phi_*}\right] \qquad (112)$$

$$\beta = \frac{4\bar{N}}{\pi S}, \quad M = \frac{M_1 M_2 R}{k_1} \qquad (113)$$

The difficulty of the problem arises because the expression
(Equation 109) is nonlinear with regard to A, due to functions (sgn A)
and $t_1 = t_1$ (A). The last function, which is included in C (A) and C* (A),
depends also on the gap Δ (Equation 105). The functions $\sin 2\omega t_1 + 2\omega t_1$
and $2\omega t_1 - \sin 2\omega t_1$ are presented in Figure 50. As we see in Figure 50
the function ($\sin 2\omega t_1 + 2\omega t_1$) is practically constant for $A > 2\Delta$ and equals
about 3.1.

We shall seek for the explicit solution $A = A(\omega)$ of Equation 106
supposing that the functions C(A) and C*(A) (Equations 103 and 109) are
constant. Then we shall introduce the functional dependences C=C(A),
C*=C* (A), applying a graphical method.

If the C and C* are supposedly constant we obtain from Equation 62:

$$A(\omega) = \pm S \frac{\beta\phi_*\phi_2 - \sqrt{\phi_1 + \phi_2^2 - \beta^2\phi_*^2 \phi_1}}{M(\phi_1 + \phi_2^2)} \qquad (114)$$

which is valid for $\beta\phi_* < 1$.

65
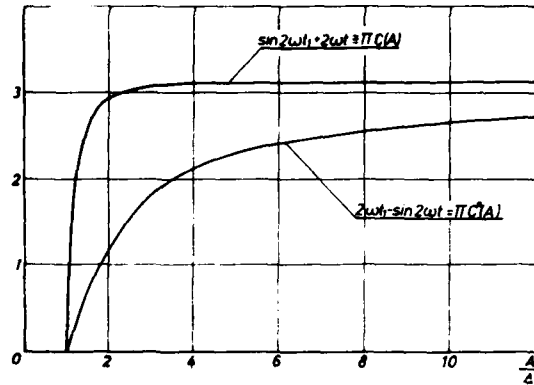
Figure 50. Graph of $t_1 = 1/\omega$ Arc Cos Δ/A

As we see, for large values of the excitation amplitude S, there exists one positive value for A and one negative of the same value. For small values of excitation, motion of this kind is not possible, and only $\psi(t)$ exists - linear motion of the mass M_1.

The expression (Equation 114) represents the relation $A=A(\omega)$, i.e., the relationship between the amplitude of the excited vibration and the frequency of the exciting force in the simplified case C=const, C*=const. A graphical method of solving Equation 109 with C and C* not constant will be explained for the particular case of a system with dry friction only in Section IV.5.

4. STEADY-STATE SOLUTION WITHOUT SLIP

Finally, for the case of small exciting force amplitude S, that is $S < 4\mu N\phi_*/\pi$, no slip of the mass M_2 occurs, unless $k_1\psi > \mu N$. Then the motion is linear and involves ψ alone, so that the equation of motion of the system becomes

$$M_1 R\ddot{\psi} + \frac{\alpha\psi h}{\omega}\dot{\psi} + k_1\psi = S\cos(\omega t - \gamma) \tag{115}$$

66

This can be solved directly for $\psi(t)$. The graph of ψ^* (where ψ^* is an amplitude of the response of ψ) versus ω is then a classical response curve up to the point where $\psi^* \geq \mu N/k_1$, at which point slip occurs, but a sustained solution with slip does not exist (because $S < 4\mu N\phi_*/\pi$). Therefore, the response under these conditions is "cut-off" at the level $\psi^* = \mu N/k_1$, i.e. amplitudes are limited. Only for $S > 4\mu N\phi_*/\pi$ can infinite amplitudes be sustained at resonance, as in Equation 114, for zero values of the other damping coefficients.

5.   SOME SPECIAL CASES

The case $\alpha_{\psi h} = \alpha_x = \alpha_{xh} = 0$ - Dry friction only. Let us consider the case without damping. The expression (Equation 114) has then the form:

$$A(\omega) = \frac{S}{M} \frac{\sqrt{1 - \beta^2 \phi_*^2}}{\sqrt{\phi_1}} \tag{116}$$

where

$$\sqrt{\phi_1} = \omega^4 - \omega^2 \left(\frac{M_1 + M_2}{M} + \frac{k_2 C}{M_2} \right) + \frac{k_2 C}{M}$$

$$\phi_* = 1 - \frac{M_1 R}{k_1} \omega^2$$

(we omit the sign minus in front of the expression (Equation 116); of course there are two solutions: positive and negative).

The function $A(\omega)$ exists only for

$$0 < \omega^2 \leq \frac{k_1}{M_1 R} \left(1 + \frac{1}{\beta} \right) \qquad \text{if } \beta \leq 1$$

$$\frac{k_1}{M_1 R} \left(1 - \frac{1}{\beta} \right) \leq \omega^2 \leq \frac{k_1}{M_1 R} \left(1 + \frac{1}{\beta} \right) \quad \text{if } \beta > 1$$

and if $\omega^2 = \frac{k_1}{M_1 R} \left(1 + \frac{1}{\beta} \right)$ then it takes the value zero.

The function $A(\omega)$, (Equation 116), tends to infinity when $\omega \to \omega_1$ or $\omega \to \omega_2$, where

$$\omega_i = \left\{ \frac{k_1}{2M_1 R}\left(\frac{M_1}{M_2} + 1\right) + \frac{Ck_2}{2M_2} + (-1)^i \sqrt{\left[\frac{k_1}{2M_1 R}\left(\frac{M_1}{M_2} - 1\right) + \frac{Ck_2}{2M_2}\right]^2 + \frac{k_1^2}{M_1 M_2 R}} \right\}^{1/2} \quad (117)$$

$$i = 1,2.$$

For $C=0$: $\omega_1^0 = 0$, $\omega_2^0 = \left\{\frac{k_1}{M_1 R}\left(\frac{M_1}{M_2} + 1\right)\right\}^{1/2}$

For $C=C_{max}$, where (Figure 50)

$$C_{max} = \frac{1}{\pi}(2\omega t_1 + \sin 2\omega t_1)_{max} = \frac{3.1}{\pi} = 0.987 \quad (118)$$

we have

$$\omega_i^m = \left\{ \frac{k_1}{2M_1 R}\left(\frac{M_1}{M_2} + 1\right) + \frac{C_{max}k2}{2M_2} + (-1)^i \sqrt{\left[\frac{k_1}{2M_1 R}\left(\frac{M_1}{M_2} - 1\right) - \frac{C_{max}k2}{2M_2}\right]^2 + \frac{k_1^2}{M_1 M_2 R^2}} \right\}^{1/2}$$

$$i=1,2$$

and $0 = \omega_1^0 < \omega_1 < \omega_1^m < \omega_2^0 < \omega_2 < \omega_2^m$.

For $\omega = 0$, $A(0) = S\sqrt{1-\beta^2}/k_2 C$ which $\to \infty$ if $C \to 0$.

Finally the function $A(\omega)$ (Equation 116) for some cases has shapes presented in Figures 51, 52, and 53.

As one sees, the presence of the dry friction does not eliminate the resonance peaks. The curves presented in Figures 51, 52, and 53 are plotted for the values C = const. In reality the value of C varies: $0 < C < C_{max} = 0.987$, when A varies in the range $\Delta < A < 2\Delta$. Then for $A < \Delta$ the curve $A(\omega)$ with $C = 0$ is applicable. For $A > 2\Delta$, the curve with

AFWAL-TR-80-4003
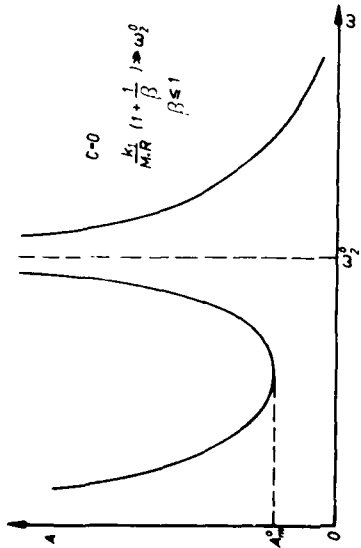
Figure 51. Response Curve (Case A ≤ A)
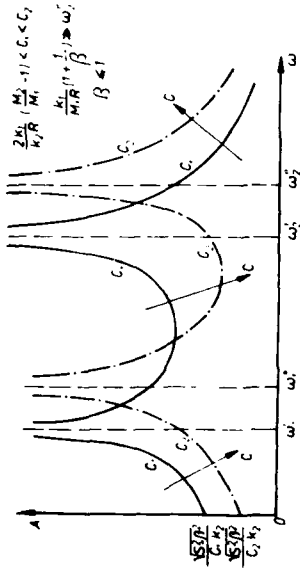
Figure 52. The Response Curves for C = C₁ = const, C = C₂ = const.
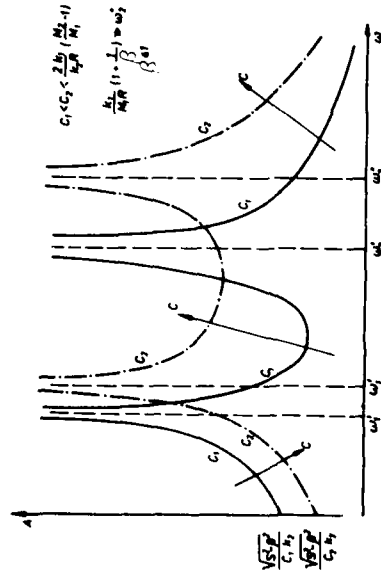
Figure 53. The Response Curves for C = C₁ = const, C = C₂ = const.
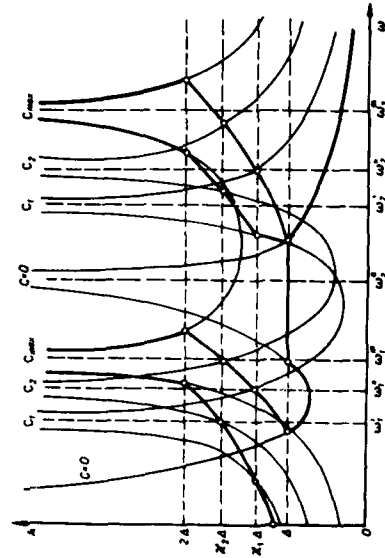
Figure 54. Graphical Method for Construction of Response Curve for the Nonlinear Case

69

$C = C_{max}$ is used. For $\Delta < A < 2\Delta$ one should plot a family of curves $A(\omega)$ with a parameter C varying $0 < C < C_{max}$ and find the corresponding points at intersections of those curves and lines $A = R_i\Delta$, $1 < R_i < 2$, $i = 1,2,3,...$, the values R_i being taken from Figure 50.

Figure 54 presents the method of plotting the real curve $A(\omega)$ (Equation 116). The shape of the $A(\omega)$ curve depends on the value of Δ. As can be seen in Figure 54, the resonance peaks of the $A(\omega)$ curve (the case without damping) always exist (two or one only). The dry friction does not cancel the resonance, it reduces only the amplitude A. The opposite effect is brought into play by the amplitude of the exciting force S. The existence of the gap Δ changes qualitatively the $A(\omega)$ curve. It brings a highly nonlinear effect. For limiting cases $\Delta = 0$ and $\Delta = \infty$, the response curves correspond to the cases $C = 0$, $C = 1$ (Figures 52 - 54) and then there is no nonlinear effect. In other cases, the nonlinear effect on $A(\omega)$ curves is more distinct if Δ is greater.

Numerical Example No. 1

Let us consider the example with the following data

$$M_1 = 1.827 \text{ kg}, \qquad M_2 = 15.3 \text{ kg}, \qquad (119)$$
$$k_1 = 14272.7 \text{ N/rad}, \qquad R = 9.09 \ 10^{-3}\text{m}.$$

Four values of β: $\beta = 0, 0.2, 1, 1.1$ and three values of k_2 were considered:

$$k_2 = 10^6\text{N/m}; \ 10^7\text{N/m}; \ 10^8\text{N/m}. \qquad (120)$$

The calculations were made on an SR 52 calculator.

The resonance curves (Equation 116) have been plotted in coordinates $(\omega, AM/S)$. In Figures 55-57 we have the family of curves (Equation 116) with different constant parameters $(C/0 \leq C \leq C_{max})$ for the case $\eta = 0$. They correspond to the values $A/\Delta = 1;1.1;1.2;\sqrt{2};2$. One can see the normal shape of the linear resonance curves for a two-degree of freedom system. For the cases $k_2 = 10^6\text{N/m}$ and $k_2 = 10^7\text{N/m}$ the first mode corresponds to the motion of the mass M_2. For the case $k_2 = 10^8\text{N/m}$ the first mode is that of the mass M_1. The second resonance zone in the cases

70
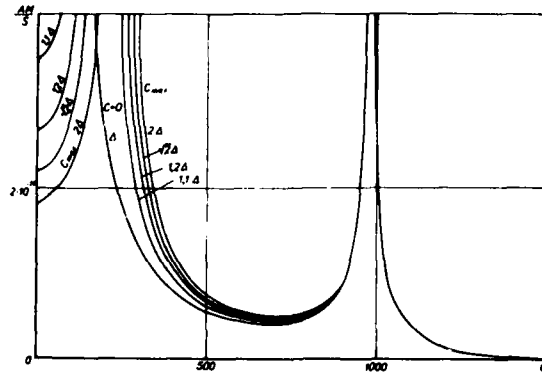
Figure 55.   Response Curves for C = const
$(k_2 = 10^6$ N/m, $\beta = 0)$
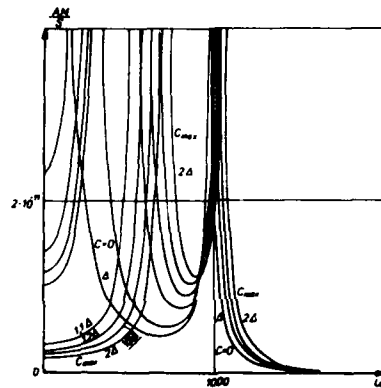
Figure 56.   Response Curves for C = const
$(k_2 = 10^7$ N/m, $\beta = 0)$
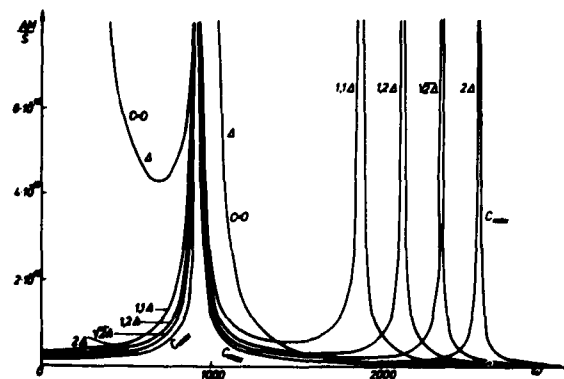
Figure 57.   Response Curves for C = const
$(k_2 = 10^8$ N/m, $\beta = 0)$

$k_2 = 10^6$ N/m and $k_2 = 10^7$ N/m for different C is nearly the same, so in this region the gap nonlinear effect will be small. Such low values of k_2 do not alter much the values ω_2 and ω_2^0 (Equation 117 and Figures 51 and 52).

Then the gap Δ is introduced and the curves corresponding to non-linear cases are plotted, applying the method explained previously. For every value of k_2 two cases of the values of the gap Δ were treated (Figures 58-60). To show the influence of the exciting amplitude the previous curves (Figures 58a - 60a) are plotted on the plane (ω, A) (Figures 58b - 60b), where the scale of A is expressed by the value of the gap Δ. As can be seen, a smaller value of S causes a reduction of the amplitude A and narrows the resonance zone. It cannot, however, cancel completely the resonance peak. For the smaller gaps (Equation 1) the nonlinear effect, which obviously has a "hard" character, is less exhibited. The gap's nonlinear effect lies in the appearance of non-uniqueness of the amplitude A for certain regions of ω. This effect is especially evident for large values of k_2 (Figure 60). One should expect that the middle value of the amplitude (dashed curve, Figures 58b - 60b) gives an unstable solution (Equation 100).

The comparison between Figures 58, 59, and 60 show the effect of the buffer's rigidity.

The curves for the case with small dry friction factor ($\beta = 0.2$) are similar to the undamped case (compare Figures 61 and 60a). The effect of the dry friction damping lies in limiting the curves on the frequency axis. For low and for high frequency excitation there is no motion (Equation 100) for the mass M_2 (Figures 62-65). For the higher dry friction some resonance zones are more narrow but the nonlinear effect of gaps are more exhibited (compare Figures 61 and 58a). If the dry friction is sufficiently high the first resonance zone can be cancelled and the effect of gap's nonlinearity disappears (Figure 62). This effect does not exist for the case $k_2 = 10^8$ N/m (Figures 63-65) It is obvious, because the first resonance in this case corresponds to the motion of the mass M_1 and there is no possibility to cancel it by the dry friction applied to the mass M.

72
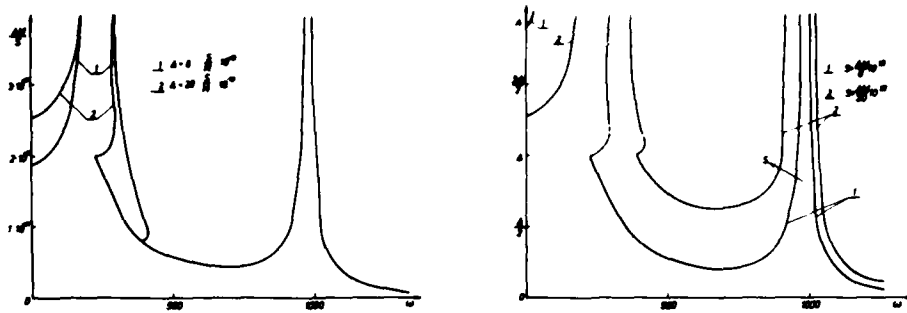
Figure 58. Response Curves for the Nonlinear Case (Undamped-
$k_2 = 10^6$ N/m) - (a) Influence of Gaps, (b) Influence
of Excitation
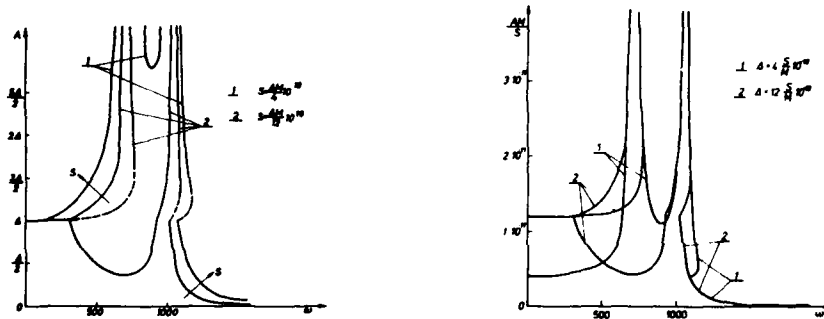
Figure 59. Response Curves for Undamped Nonlinear Case ($k_2 = 10^7$ N/m),
(a) Influence of Excitation, (b) Influence of Gaps
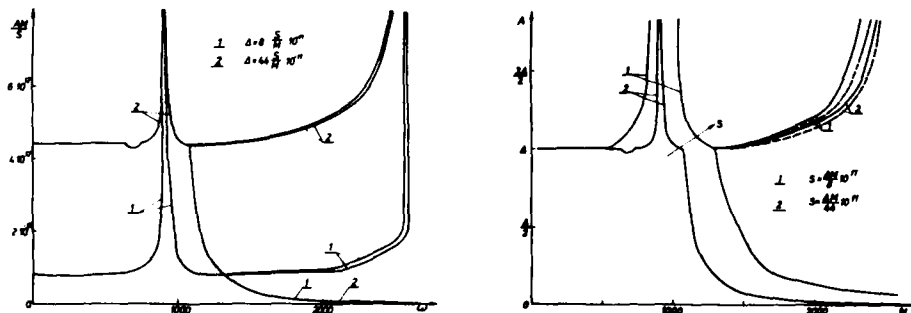
Figure 60. Response Curves for Undamped Nonlinear Case ($k_2 = 10^8$ N/m),
(a) Influence of Gaps, (b) Influence of Excitation

73
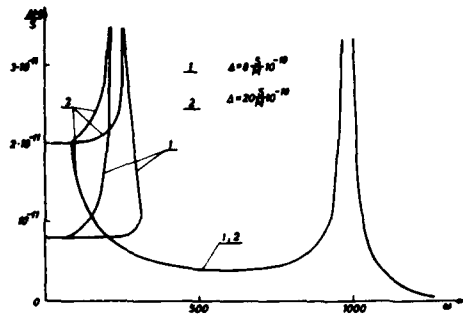
Figure 61. Response Curves for the Case with Dry Friction ($k_2 = 10^6$ N/m, $\beta = 1$)
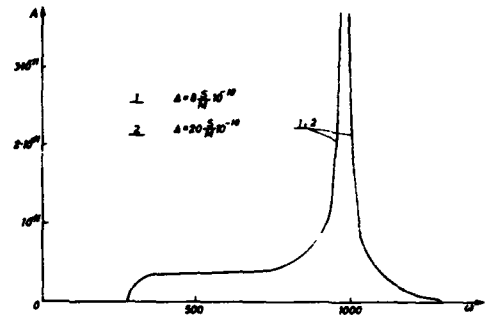
Figure 62. Response Curves for the Case with Dry Friction ($k_2 = 10^6$ N/m, $\beta = 1.1$)
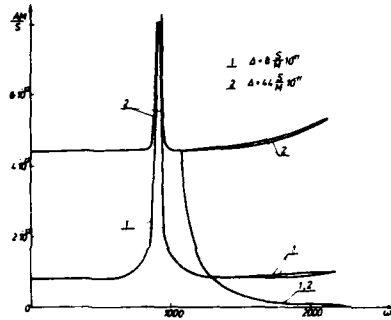
Figure 63. Response Curves for the Case with Dry Friction ($k_2 = 10^8$ N/m, $\beta = 0.2$)
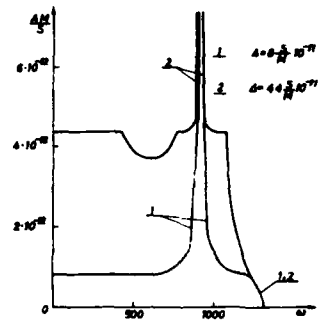
Figure 64. Response Curves for the Case with Dry Friction ($k_2 = 10^3$ N/m, $\beta = 1$)
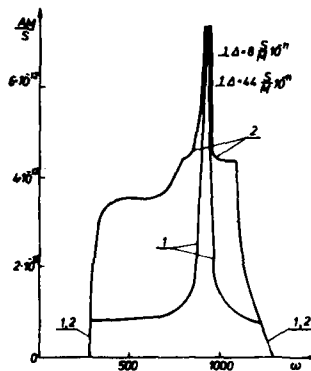
Figure 65. Response Curves for the Case with Dry Friction ($k_2 = 10^8$ N/m, $\beta = 1.1$)

<u>The Case $\mu N = \alpha_{\psi h} = \alpha_{xh} = 0$. Fluid pumping only</u>.

Let us consider the case without dry friction and without hysteretic damping. Only the dissipation by fluid pumping in gaps is present. The response curve is given by Equation 116 (for C = const) with $\eta = 0$ (we omit the sign minus, of course, there exists two solutions: a positive and a negative):

$$A(\omega) = \frac{S}{M} \frac{1}{\sqrt{\phi_1(\omega) + \phi_2^{\,2}(\omega)}} \tag{121}$$

where

$$\phi_1(\omega) = \left[\omega^4 - \omega^2 \left(\frac{M_1 + M_2}{M} + \frac{k_2 C}{M_2} \right) + \frac{k_2 C}{M} \right]^2 \tag{122}$$

$$\phi_2(\omega) = \frac{\omega \alpha_x}{M_2} \left(\frac{k_1}{M_1 R} - \omega^2 \right).$$

For small values of the damping coefficient α_x the response curve (Equation 121) has two maximum peaks (for ω near ω_1 and ω_2, Equation 70), Figure 66. The position of the peaks depends on the values of α_x and C as well. So the nonlinear effect of the gap can be reflected in the $A(\omega)$ curve in the same manner as previously, plotting a family of curves with C as a parameter and finding the intersection points with corresponding levels $A = R_i \Delta$, where $1 \leq R_i \leq 2$, $i = 1,2,\ldots$. For $A \leq \Delta$ the curve (Equation 121) with C = 0 is valid. For $A > 2\Delta$ the curve (Equation 121) with $C = C_{max}$ (Equation 118) is valid.
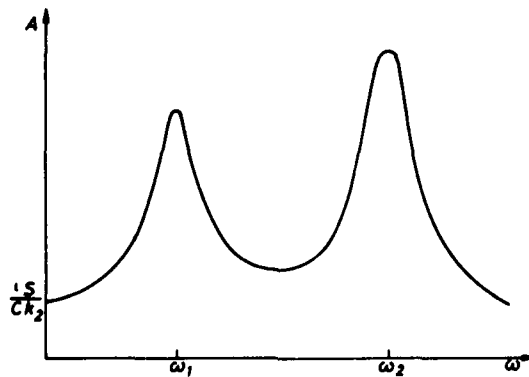
Figure 66. Response Curves for a Damped Case

75

Numerical Example No. 2

Let us consider the same example as previously, with $\eta = 0$, adding the fluid damping coefficient (four different values):

$$\alpha_x = 10^3 \text{Ns/m}; \quad 1500 \text{ Ns/m}; \quad 4000 \text{ Ns/m}; \quad 7000 \text{ Ns/m}. \tag{123}$$

The results of the calculations of the response curves (Equation 121) are presented in Figures 67-72. The curves obtained applying the same graphical method are plotted in the coordinates (ω, A), where A is expressed in terms of the gap's magnitude Δ. One can see the influence of the gap coefficient $M\Delta/S$ on the nonlinear behavior of the $A(\omega)$ curves. The curves show the influence of the amplitude of the exciting force S on the $A(\omega)$ relationship. The growing S causes an increase of A and some qualitative changes (appearance of new branches of $A(\omega)$). The influence of the damping coefficient α_x can be investigated by comparing the curves corresponding the same value of k_2 (Figures 68 - 72). The curves $A(\omega)$, for small values of α_x do not differ much from the curves for the previous case $\beta = 0$ (compare for instance Figures 59b and 68). The greater values of α_x cause the disappearance of some A branches (compare Figures 59 and 69 or 60 and 72), a reduction of the amplitude A and a disappearance of the resonance (compare Figures 58 and 67, 59 and 69, 60 and 71) and a "softening" of the response curve (compare Figures 69 and 70). The growing coefficient α_x changes a little the frequency ω_1, ω_2 of the greatest amplitude A (to smaller values of ω for $k_2 = 10^6 \text{N/m}$, brings closer both of them for $k_2 = 10^7 \text{N/m}$). The increasing coefficient α_x cancels more efficiently the first resonance (for $k_2 = 10^8 \text{N/m}$). The same value of α_x has more influence on the shape of the resonance curve if k_2 is smaller (compare Figures 58, 59, 67 and 69).
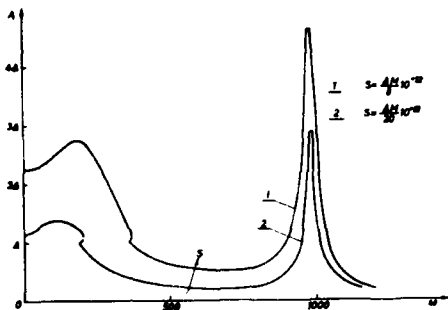
Figure 67. Response Curves ($k_2 = 10^6$ N/m,
$\beta = 0$, $\alpha_x = 4000$ Ns/m)
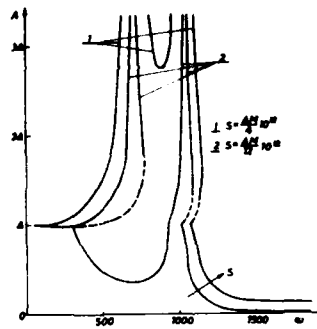
Figure 68. Response Curves ($k_2 = 10^7$ N/m,
$\beta = 0$, $\alpha_x = 1000$ Ns/m)
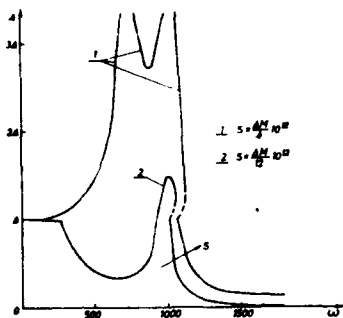
Figure 69. Response Curves ($k_2 = 10^7$ N/m,
$\beta = 0$, $\alpha_x = 4000$ Ns/m)
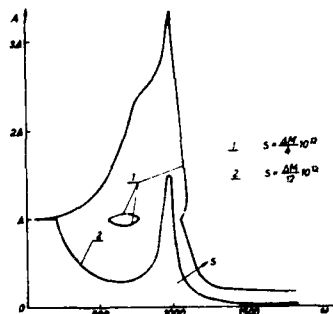
Figure 70. Response Curves ($k_2 = 10^8$ N/m,
$\beta = 0$, $\alpha_x = 7000$ Ns/m)
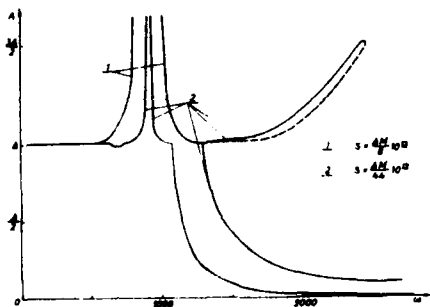
Figure 71. Response Curves ($k_2 = 10^8$ N/m,
$\beta = 0$, $\alpha_x = 1000$ Ns/m)
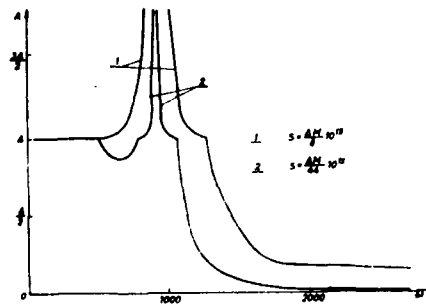
Figure 72. Response Curves ($k_2 = 10^8$ N/m,
$\beta = 0$, $\alpha_x = 7000$ Ns/m)

77

The Case $N = \alpha_x = \alpha_{\psi h} = 0$. Hysteretic damping in the buffer springs only

Let us consider the case without the dry friction and without the fluid pumping. Only dissipation by hysteretic damping in the buffers is present. The response curve is given by Equation 114 (for C = const, $C^* $ = const) with $\beta = 0$ (we omit the sign minus):

$$A(\omega) = \frac{S}{M} \frac{1}{\sqrt{\phi_1(\omega) + \phi_2^2(\omega)}} \tag{124}$$

where in this case ϕ_1 is the same as previous (Equation 122) and

$$\phi_2(\omega) = \frac{\alpha_{xh} C^*}{M} \left(1 - \frac{M_1 R}{k_1} \omega^2\right).$$

For small values of damping coefficient α_{xh} the response curve (Equation 124) has two maximum peaks (for ω being near ω_1 and ω_2, see Equation 117 and Figure 66).

Numerical Example No. 3

Let us consider example 2 (with $\beta = 0$), adding the hysteretic damping coefficient (three values):

$$\alpha_{xh} = 10^7 \text{N/m}; \ 10^8 \text{N/m}; \ 2 \ 10^{10} \text{N/m}.$$

The results of the calculations of the response curves (Equation 124) with different values of α_{xh} are presented in Figures 73-75. The curves are plotted in the same coordinates (ω, AM/S) as previously. There can be seen the influence of the magnitude of the gap coefficient $\Delta M/S$ on the nonlinear behavior of the $A(\omega)$ curves. The damping brought by the buffers has nearly the same influence on $A(\omega)$ relationship as the fluid pumping. However, the effect of damping contributed by the coefficient α_{xh} is much smaller than that of α_x (compare the magnitudes of α_{xh} and α_x which give nearly the same effect of damping - Figures 69 and 73, 70 and 74, 71 and 75). For sufficiently high damping, the amplitude A of vibration does not exceed the value of the gap Δ. The nonlinear
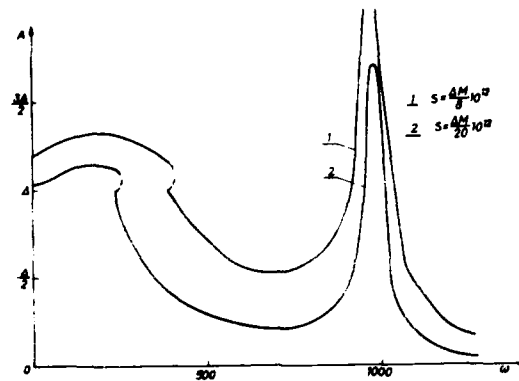
Figure 73. Response Curves (k_2 10^6 N/m, $\beta = 0$, $\alpha_x = 0$, $\alpha_{xh} = 2.10^{10}$ N/m)
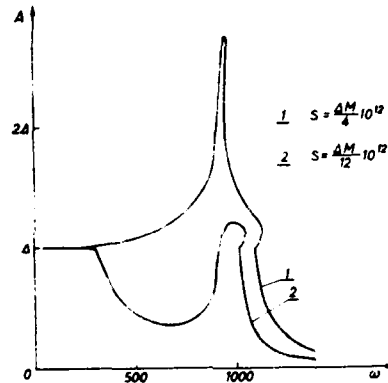
Figure 74. Response Curves ($k_2 = 10^7$ N/m, $\beta = 0$, $\alpha_x = 0$, $\alpha_{xh} = 10^8$ N/m)
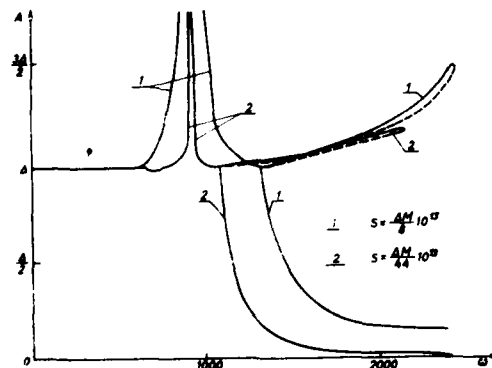
Figure 75. Response Curves ($k_2 = 10^8$ N/m, $\beta = 0$, $\alpha_x = 0$, $\alpha_{xh} = 10^7$ N/m)

effect due to the gap is present in all the cases (regions of frequency where three values of amplitude are present, with sudden non-smooth changes of amplitude values).

The Case $\alpha_{xh} = \alpha_{\psi h} = 0$. Dry friction and fluid pumping only

Let us consider the case without hysteretic damping. The dissipation is caused by dry friction and fluid pumping together.

The resonance curve is given by Equation 114 (for C = const and C* const):

$$A(\omega) = S \frac{-\beta \phi_2^2 \phi_* + \sqrt{\phi_1(1-\beta^2 \phi_*^2) + \phi_2^2}}{M(\phi_1 + \phi_2)} \qquad (125)$$

where ϕ_1 is given by Equation 122 and

$$\phi_* = 1 - \frac{M_1 R}{k_1} \omega^2, \quad \phi_2 = \frac{\alpha_x \omega \phi_*}{M} .$$

Numerical Example No. 4

We shall consider example 2 with the fluid pumping coefficient (two values):

$$\alpha_x = 2000 \text{ Ns/m}; \ 4000 \text{ Ns/m}.$$

The results of calculations can be seen in Figures 76 and 77. The common effect of the dry friction and the fluid damping reduces the resonance amplitude and limits the zone of frequency (compare Figures 61, 62 and 70, 77). The gap's effect has nearly disappeared.
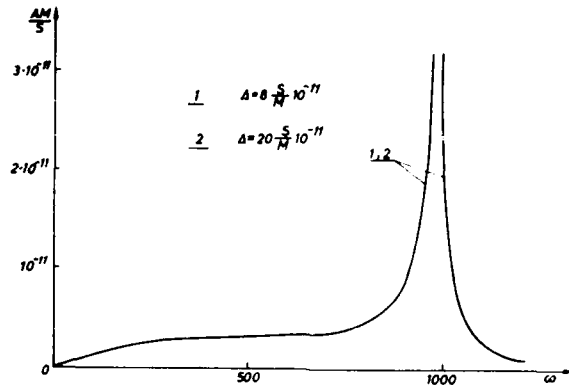
Figure 76.   Response Curves ($k_2 = 10^6$ N/m,
$\beta = 1$, $\alpha_x = 2000$ Ns/m, $\alpha_{xh} = 0$)
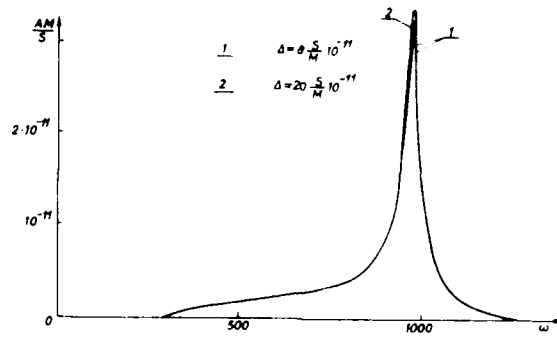
Figure 77.   Response Curves ($k_2 = 10^6$ N/m,
$\beta = 1.1$, $\alpha_x = 4000$ Ns/m,
$\alpha_{xh} = 0$)

6. TIME DEPENDENCE OF THE DEFLECTION ψ

After having found the value of the amplitude A of the solution for given parameters, and for every value of the frequency ω, it is possible to obtain the time dependence of the deflection $\psi(t)$. Putting Equation 100 into Equation 102 we obtain:

$$\psi(t) = \frac{A}{k_1} (k_2 \psi^* - M_2 \omega^2) \cos \omega t - \frac{A\omega}{k_1} (\alpha_x +$$

$$\frac{\alpha_{xh}}{\omega} \psi^*) \sin \omega t - \mu \bar{N} \text{ sign } (\sin \omega t). \tag{126}$$

Taking into account the values of ψ^* (Table 4) for every interval of time, we can plot the relation (Equation 126) in coordinates $(t, \psi(t))$. Figure 78 shows the graphical construction of the Equation 126 for small and great values of frequency. As it can be seen, due to the nonlinear effects, the time dependence of the deflection $\psi(t)$ represents a complicated curve. Practically, in real systems, it will be much more smooth - the modelization accepted here is quite idealized.
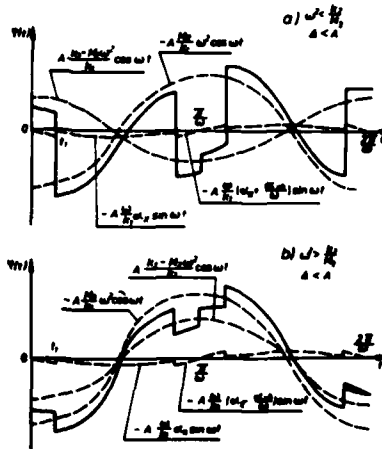
Figure 78. Time Dependence of the
Deflection of the Mass M_1

7. SUMMARY

The response of a mechanical system to a periodic excitation is strongly dependent upon the tolerance between parts. In this section it has been shown that the response (amplitude versus frequency) is very sensitive to the value of the gaps - the response curves change not only quantitatively but qualitatively as well with variation of the gap's magnitude. The presence of gaps introduces nonlinear effects. A change of the gap's magnitude may increase the amplitude of the response, which can cause premature damage or failure of the system.

Another nonlinear effect is caused by dry friction in the system. The dry friction reduces the response amplitudes, it cannot completely cancel the resonances. Both nonlinear effects cause the nonuniqueness of the amplitude of the response for certain regions of frequency. The external damping brings usual effects of amplitude reduction.

A graphical method was adapted for construction of the response curves for nonlinear systems. This method is valid for any nonlinearity in the system, but its advantages are especially clear for discontinuous functions.

SECTION V

EXPERIMENTAL INVESTIGATIONS

1. BLADE DESCRIPTION

The analytical part of this report describes the fundamental mode dynamic behavior of a typical jet engine compressor or turbine blade having a simple dovetail root, with allowance for slip at the root. The purpose of the test program was to verify, as far as possible, the results of the analysis. The blade selected for the initial tests was a relatively large twisted steel blade with a simple root geometry as shown in Figures 79 and 80. The blade was held in a heavy fixture having mating surfaces to match the contours of the blade root. The centrifugal load was represented by means of simple spring loaded wires applied at the root in such a way as to minimize interference with the blade root motion during slip. This arrangement, shown in Figure 80, is not ideal in so far as it does not allow for the effect of the centrifugal load in untwisting the blade, but it does represent the root conditions far more adequately than, for instance, clamping the root by means of a bolt, which would prevent slip and hence inhibit the very phenomenon being studied. The blade was about 20 cm long.

2. TEST SYSTEM

For determining the mode shapes of the blade, a digital test system illustrated in Figure 81 was used. The blade was solidly clamped at the dovetail and excited by a small shaker through a force gauge at the block. The acceleration response was measured at several points on the blade surface using a miniature accelerometer and transfer functions measured at several points on the blade.

For the harmonic vibration tests on the blade with slip, the analog test system illustrated in Figure 82 was used. The Bruel and Kjaer Model 1014 Beat Frequency Oscillator can generate a harmonically oscillating voltage of magnitude 0 to 120 volts at any selected frequency from 20 Hz to 20 KHz. The output impedance, measured in ohms, can be varied according to the type of excitation device used in order to match impedances as
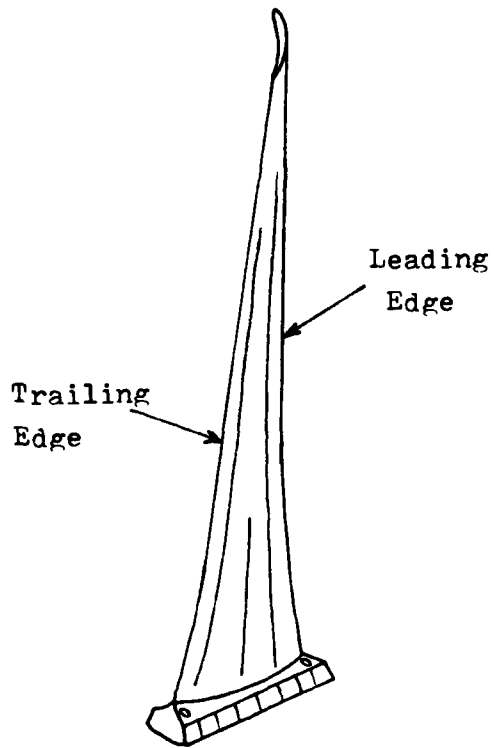
Figure 79.   Blade Geometry
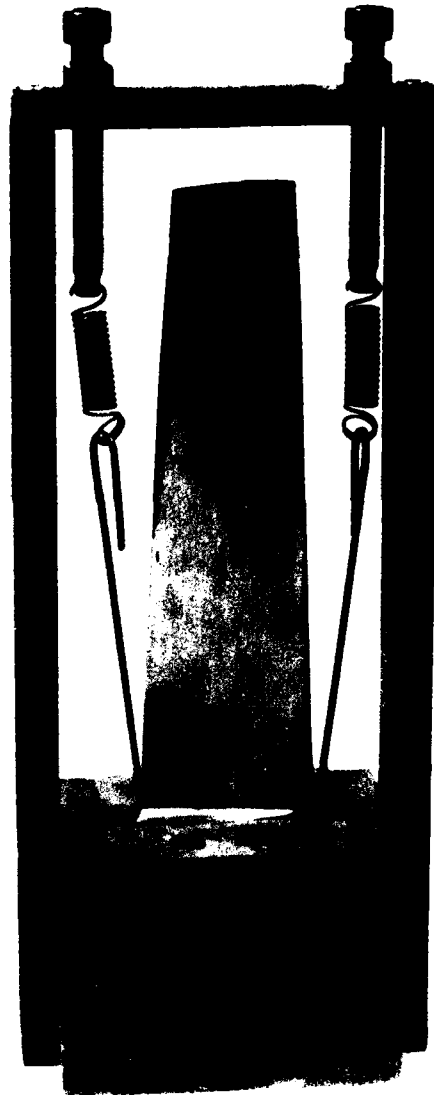
Figure 80.   Photograph of Blade in Fixture
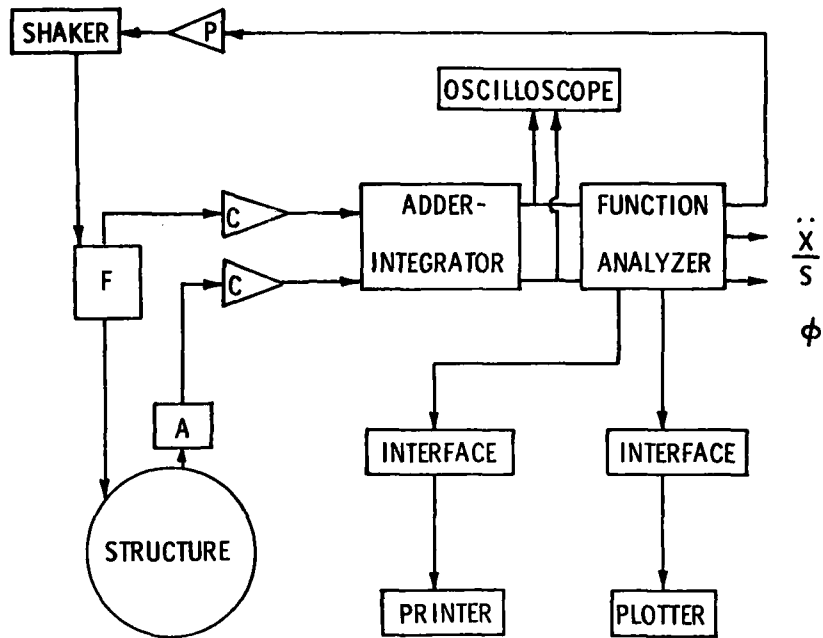
Figure 81.   Digital Test System
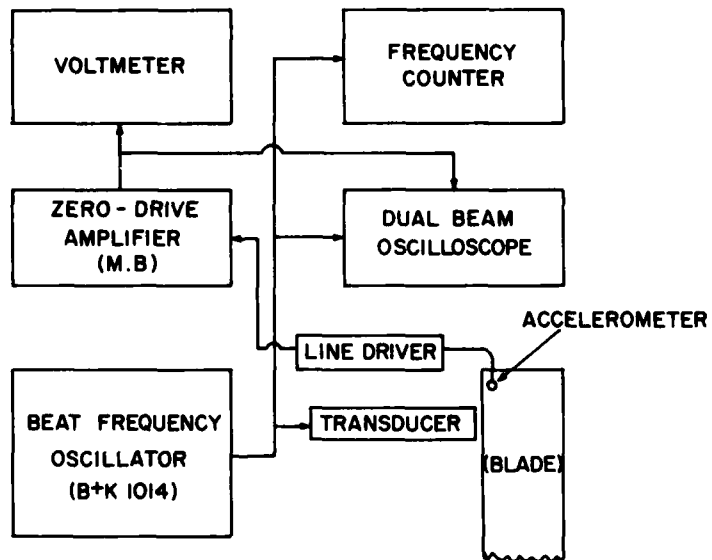
Figure 82.   Analog Test System

closely as possible. As the frequency is varied, the current through the output terminals to the exciter can be controlled by means of the "compressor". This is simply a feedback loop which measures the voltage across a fixed resistor in the output circuit, and uses it to control the output current. A meter gives the output voltage across the terminals.

The output current of the oscillator was fed directly to a magnetic transducer (Electro Model 3030-HTB). The impedance setting of the oscillator was set at 600 ohms in order to best match the impedance of the transducer, thereby minimizing distortion of the output signal. The transducer consists essentially of a magnetized iron rod with many coils of fine insulated wire surrounding it, through which the oscillating current flows. This current produces an oscillating magnetic field which modulates the steady magnetic field of the rod, and hence produces an oscillating harmonic force on any iron object placed nearby. The magnitude of this force depends on the amplitude of the oscillating on current and on the gap between the end of the magnetized rod and the object being excited. A typical transducer section is shown in Figure 83.

The waveform of the input signal to the transducer was monitored on a dual - beam oscilloscope (Ballantine Model 1066S). The frequency of the signal was measured by a digital frequency meter (Hewlett Packard Model 5216A). The pickup system used a miniature accelerometer (Endevco Type 22) weighing about 0.2 grams. The acceleration amplitude of the blade at the point where the accelerometer was attached, with cyano-acrylate adhesive, was detected by the quartz crystal in the accelero-meter, unlike the transducer, is an extremely high impedance device so that a special high input impedance amplifier (MB N-400 Zero Drive amplifier) had to be used to amplify the signal before it could be read off the Vacuum Tube Voltmeter (Hewlett Packard Model 3400A) and monitored on the other channel of the dual beam oscilloscope. A "line-driver" (MB Type 9402215) was used to reduce loss of signal in a relatively long cable. Because of the high system impedance, current levels in the cables were very low and care had to be taken to avoid excessive loss of signal or pickup of stray signals.
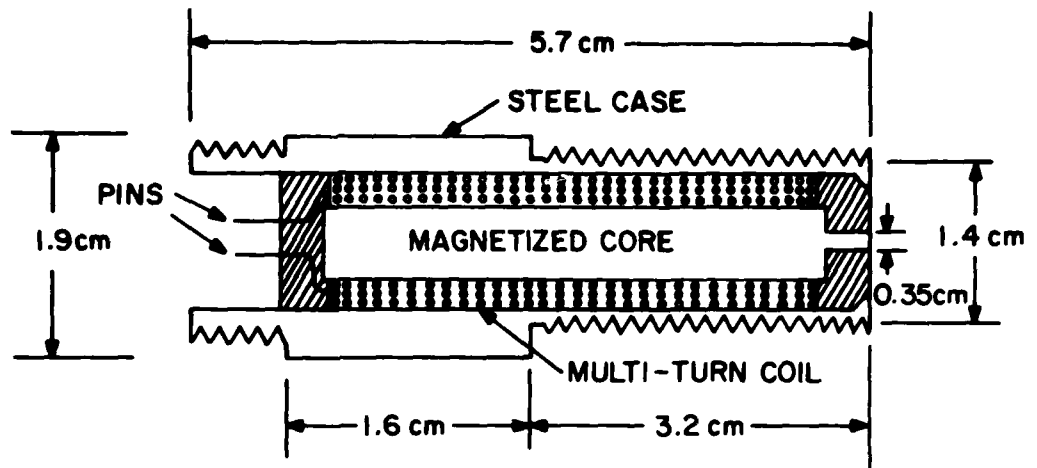
Figure 83. Transducer Section (Sketch)

3.   MEASUREMENT OF MODE SHAPES

For the first two modes of the compressor blade, the transfer functions $|\ddot{X}/S|$ were measured, as a function of frequency, using a small shaker acting through an impedance head for excitation and an accelerometer for pickup as in Figure 81. Results were plotted for points (0,0), (0,1) --- as illustrated in Figure 80. Figure 84 shows a typical response. Figures 85 to 89 show more detailed plots near each resonance. The system was not calibrated. The product $(\hat{\ddot{X}}/S)\eta_n$ was then calculated for each mode, as shown in these figures. Note that $(\ddot{X}/S)$ is drawn on a decibel scale, so that one must convert back to a linear scale in performing the calculation, as follows:

$$\left|\frac{\hat{\ddot{X}}}{S}\right| \text{ linear} = \log_{10}^{-1}\left(\frac{\hat{\ddot{X}} \text{ db}}{20S}\right)$$

For example, for point (0,0), mode 1, $\frac{\ddot{X}}{S} = 39\text{db}$ and $\eta_1 = 0.00287$.

$$\therefore \frac{\hat{\ddot{X}} \eta_1}{S} = \log_{10}^{-1}\left(\frac{39}{20}\right) \times 0.00287 = 0.256$$

The summarized modal data is given in Table 5. These modes are plotted in Figures 90 and 91. The modes can now be used to calculate the equivalent masses and stiffnesses of the discrete model of the blade.

88
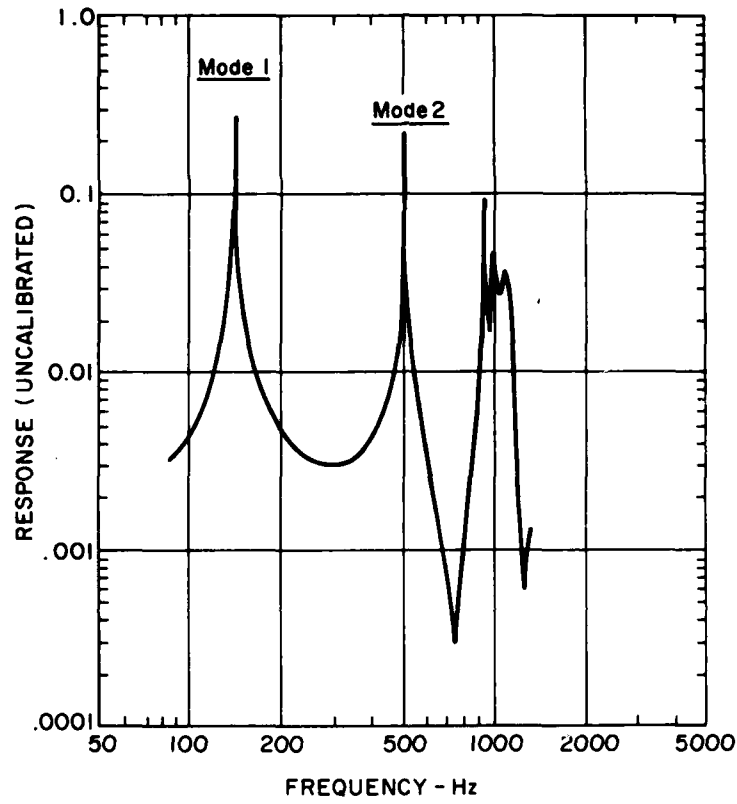
Figure 84. Typical Response Spectrum for Clamped Root
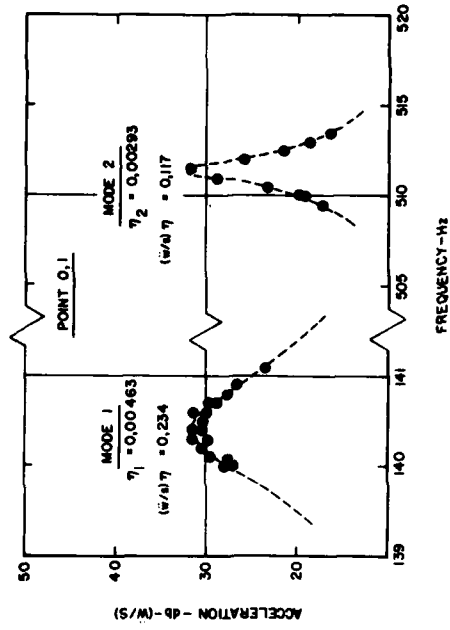
Figure 85. Resonance Peaks for Point 0,0
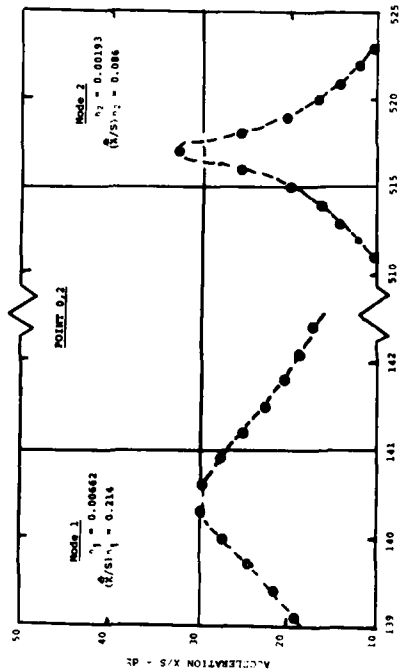
Figure 86. Resonance Peaks for Point 0,1
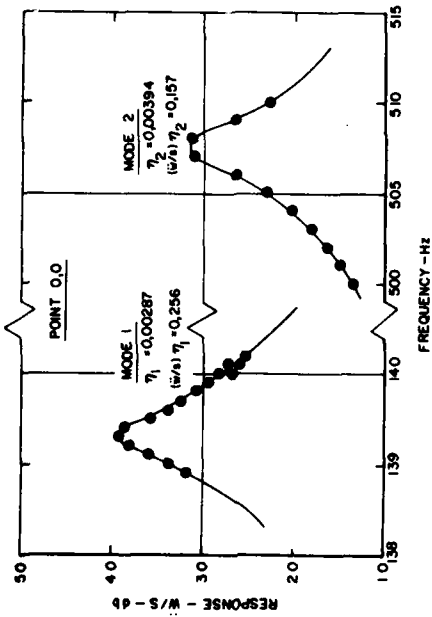
Figure 87. Resonance Peaks for Point 0,2
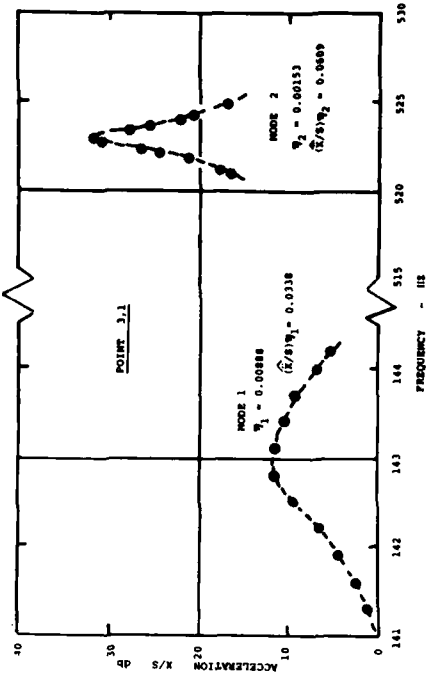
Figure 88. Resonance Peaks for Point 3,1

90
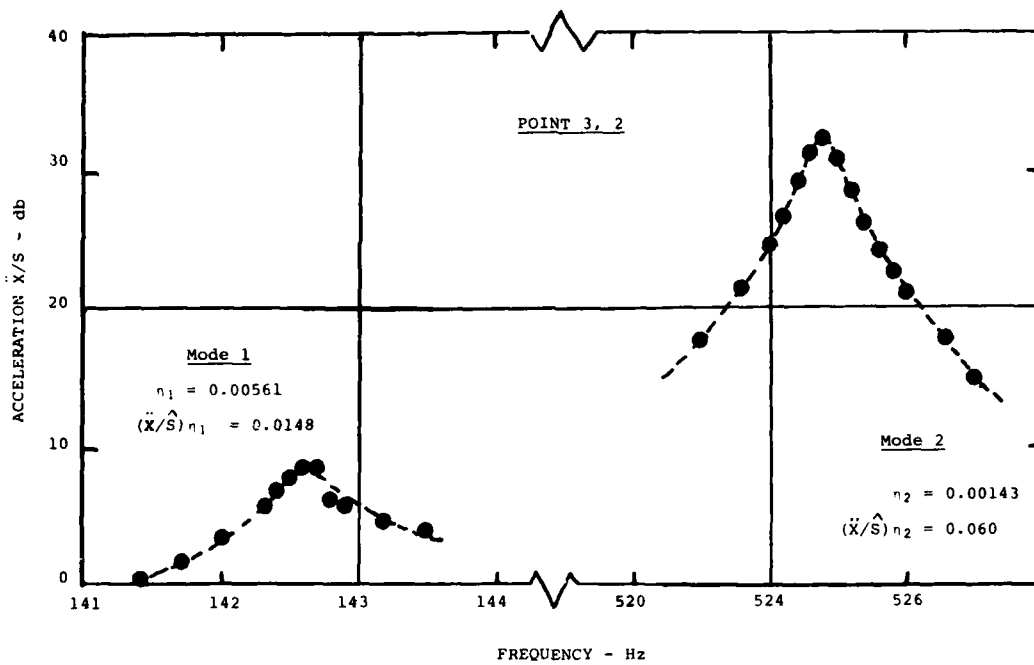
Figure 89. Resonance Peaks for Point 3,2

TABLE 5

MODE SHAPE DATA

Point	$(\ddot{X}/S)\eta_1$	$(\ddot{X}/S)\eta_2$	ϕ_1	ϕ_2
0,0	+0,256	+0,157	+1,000	+1,000
0,1	+0,234	+0,117	+0,914	+0,745
0,2	+0,214	+0,086	+0,836	+0,548
1,0	+0,189	+0,039	+0,738	+0,248
1,0	+0,148	+0,004	+0,578	+0,025
1,2	+0,147	-0,023	+0,574	-0,146
2,0	+0,107	-0,043	+0,418	-0,274
2,1	+0,087	-0,057	+0,340	-0,363
2,2	+0,070	-0,081	+0,273	-0,516
3,0	+0,043	--	+0,168	--
3,1	+0,034	-0,061	+0,131	-0,388
3,2	+0,015	-0,060	+0,058	-0,381

91
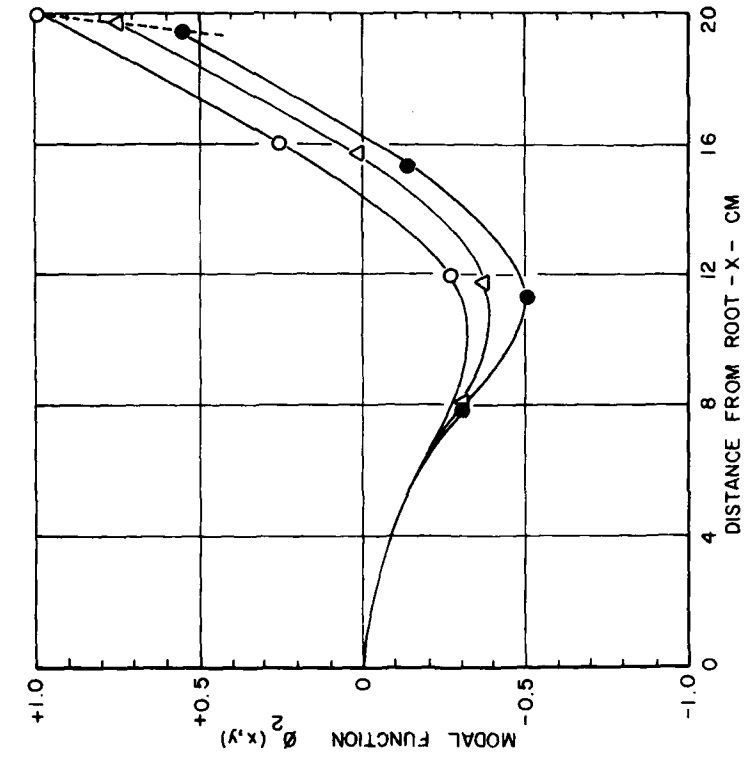
Figure 91.   Second Mode Shape
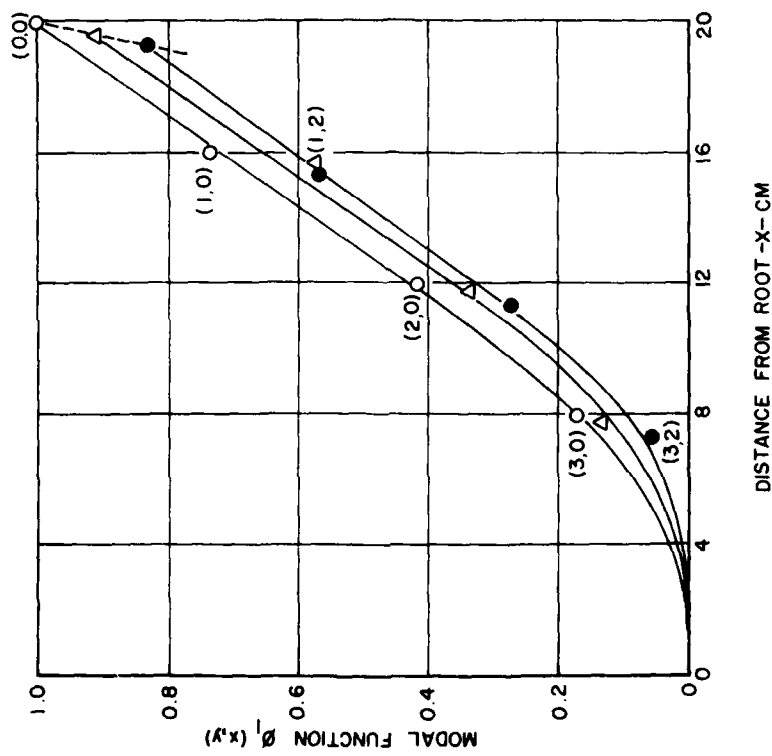
Figure 90.   Fundamental Mode Shape

Note that the frequency ω_n changes somewhat with the position of the measurement. This is due to mass loading by the accelerometer. The difference is sufficiently small to be insignificant, and is assumed to have only second-order effects on the mode shapes, in view of the wide separation of the resonant frequencies. Finally, note that $\vec{\phi}_n$ is a vector, assumed to be normal to the blade middle surface. The direction cosines relative to the major axis of the root were measured to be:

Station	Inclination α°	$\cos \alpha$
0	44°	0.724
1	36	0.808
2	31	0.861
3	20	0.938
4	13	0.972

4. CALCULATION OF MODAL INERTIA AND STIFFNESS FROM MODE SHAPES

The thickness of the blade was measured at several stations and across the chord. Figure 92 shows the distribution of thickness. The values of m_1 and β_1 were determined from Equations 45 and 46 using the modal data, the direction cosines, and the density of the blade material, assumed to be 0.27 lb/in^3. On this basis:

$$m_1' = \iint\limits_{xy} \rho h \; dxdy = 0.235 \text{ kg}$$

$$\beta_1' = \frac{m_1' \vec{n}(x_1, y_1) \cdot \vec{\phi}_1(x_1, y_1)}{\iint\limits_{xy} \rho h \; \vec{\phi}_1 \cdot \vec{\phi}_1 \; dxdy} = \frac{0.235 \times 1 \times 1}{0.0324} = 7.25$$

$$\therefore m_1 = \frac{0.235}{7.25} = 0.0324 \text{ kg}$$

$$\therefore I_1 = L^2 m_1 = 1.296 \times 10^{-3} \text{ kgm}^2$$

$$\therefore K_1' = m_1 \omega_1^2 = 0.0324 \, (2\pi \times 120)^2 = 18419 \text{ N/m}$$

$$K_1 = L^2 K_1' = 737 \text{ Nm/m}$$
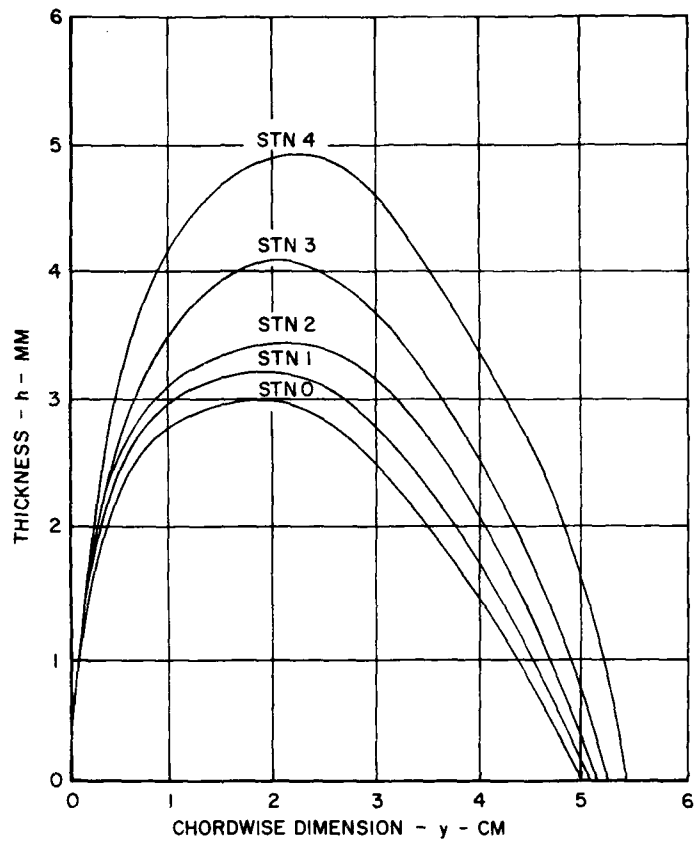
Figure 92.   Thickness Distribution of Blade

Note that the value of K_1' is measured in N/m because X_1 is the independent variable, not X_1/L, where L is the blade length.

5. MEASUREMENT OF RESPONSE WITH SLIP

The tests with slip were conducted using a magnetic transducer for excitation, with a pre-selected gap, (0.04 in., 1mm) at several different force levels ranging from 0.0064 Newtons to 0.125 Newtons, the maximum that could be generated with the transducer available. The net normal force provided by the two springs to the wires at the root of the blade was varied from 10 kg to 25 kg. As the excitation frequency was increased slowly, at low force levels, the classical shape of the response curve ($|X_1/S|$ versus frequency) was reproduced, but as the exciting force was increased the behavior became increasingly nonlinear. The results obtained for tests with air and water as the working fluid around the blade root mating surfaces are shown in Figures 93 to 100 for the first three modes. Test results are summarized in Tables 6 to 10.

Several significant facts may be noted from these figures. One is that as S is decreased, a point is reached at which slip never occurs and the behavior is then linear. In that case, the only significant remaining source of damping is hysteresis of the blade material itself. The second is the fact that as water is substituted for air as the working fluid at the root, slip occurs far more readily. This is accounted for by the fact that coefficient of friction is lower in this case. Figures 101 and 102 show some of the acceleration waveforms observed on the oscilloscope screen for various conditions. The upper curves represent the blade acceleration, and the lower curves the force, all at the point of maximum amplitude. In air, one can see significant deviations from a true sinusoidal shape. In water, the lower threshold of slip seems to allow high order harmonics to be present in the signal. The reason for this is not known.
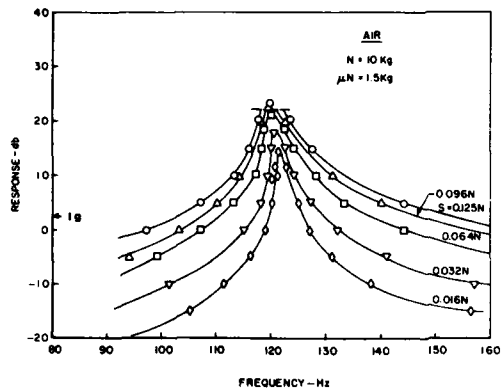
Figure 93.   Measured Response in Mode 1
(N̄ = 10 kg, Air)
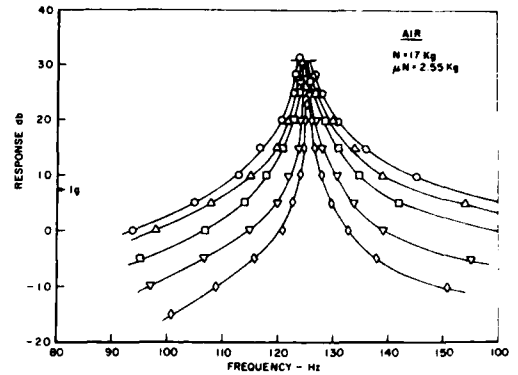
Figure 94.   Measured Response in Mode 1
(N̄ = 17 kg, Air)
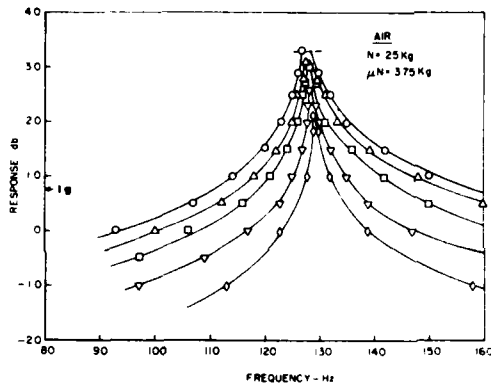
Figure 95.   Measured Response in Mode 1
(N̄ = 25 kg, Air)
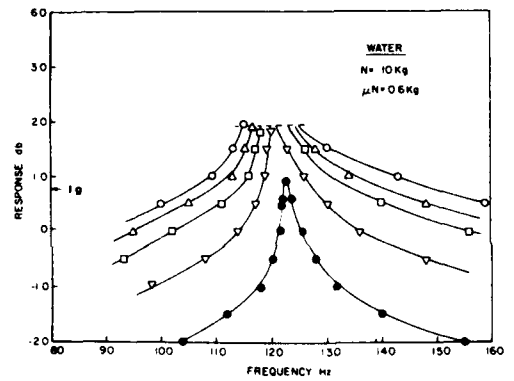
Figure 96.   Measured Response in Mode 1
(N̄ = 10 kg, Water)
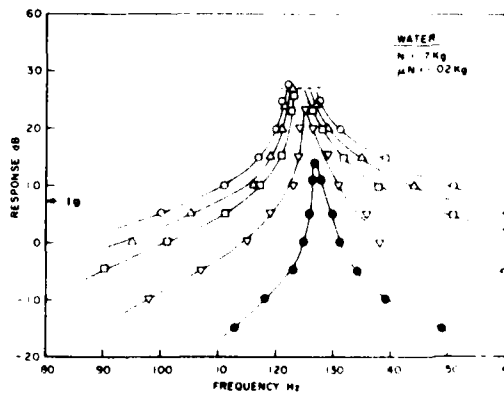
Figure 97.   Measured Response in Mode 1
(N = 17 kg, Water)
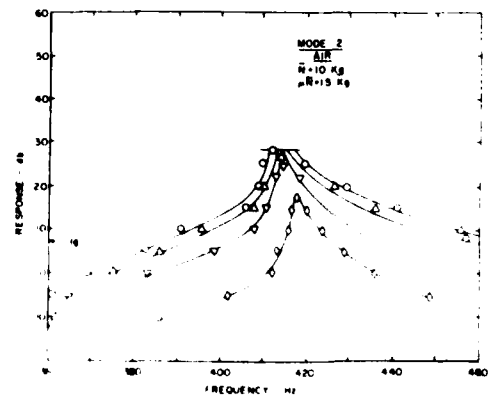
Figure 98.   Measured Response in Mode 2
(N = 10 kg, Air)
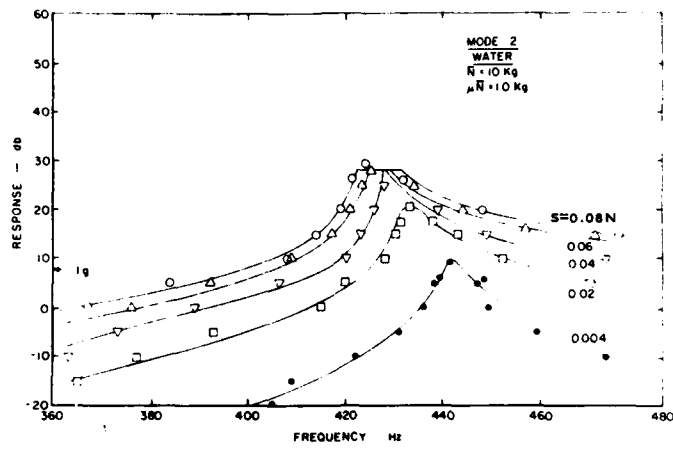
Figure 99. Measured Response in Mode 2
($\overline{N}$ = 10 kg, Water)
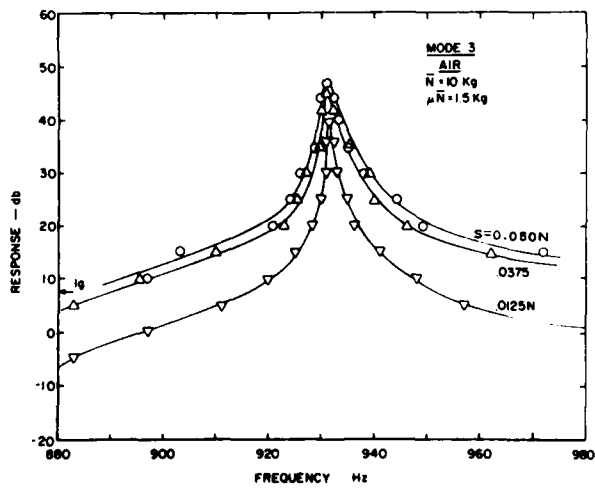
Figure 100. Measured Response in Mode 3
($\overline{N}$ = 10 kg, Air)

97

TABLE 6

TEST RESULTS FOR BLADE ROOT IN AIR $\bar{N}$ = 10 kg (22.0 lb),
CALIBRATION: 7.5 db ≅ 1 g SPRING TYPE 2, LENGTH = 63.5 mm
(2.5 INCHES)

Mode	Input (Volt)	Force S (Newtons)	A_2	Zero Drive	VTVM	Freq (Hz)	Output (db)	X/S (m/N)	η_n
1	30	0.096	21.2	10	3	119.3	23	1.08E-3	3.52E-2
						118.2	20	7.81E-4	
				3	3	122.4	20	7.29	
				1	3	118	20	7.84	
				1		114	10	2.66	
						110	5	1.60	
				1	1	103	-5	1.03	
					.3	94	-10	6.95E-5	
				1	.1	80	-20	5.39	
				1		54	-25	3.74	
						17	-20	2.12E-4	
				1	.3	38	-10	7.56E-5	
				10	3	59	23	9.92	
				3	3	119	15	1.09E-3	
						127	10	3.81E-4	
				1	3	131	0	2.01	
						140	-7	9.90E-5	
				1	1	161	-5	4.21	
						185	-5	1.79	
						208	0	1.13	
						213		1.35	
						218		2.30	
1	40	0.128	15.9	10	3	119.4	23.5	8.59E-4	5.11E-2
						117.3	20.5	6.30	
				3	3	123.4	20.5	5.69	
				3		116	15	3.42	
				1	1	113	10	2.03	
						107	5	1.27	
				1	1	97	0	8.70E-5	
						87	-5	6.08	
				1	3	75	-10	4.60	
				10	3	68	-10.5	5.29	
						127	15	2.85E-4	
				3	1	134	10	1.44	
						149	5	6.54E-5	
				1	1	171	0	2.80	
						203	-4	1.25	

Mode	Input Volts	Force S Newtons	β_2	Zero Drive	VTVM	Freq Hz	Output db	X/S m/N	η_n
1	20	0.064	31.8	10	3	119.7	21.5	1.36E-3	3.09E-2
						118.6	18.5	9.79E-4	
				3	3	122.3	18.5	9.21	
				3	1	118	15	6.61E-4	
						117	10	3.78	
				1	1	113	5	2.28	
						107	0	1.43	
				1	.3	99	-5	9.39E-5	
						87	-15	6.84	
						75	-18	5.18	
				3	3	66		4.73	
				1	3	124	15	5.99E-4	
						128	15	3.16	
						133	10	1.65	
				1	1	144	5	7.90E-5	
						164	0	3.42	
						194	-5	1.38	
						208	-10	1.07	
							-11		
1	10	0.032	63.5	3	3	120.3	18	1.80E-3	2.16E-2
						119.9	15	1.28	
				1	3	122.5	15	1.23	
				1	1	119.0	10	7.31E-4	
						118	5	4.18	
				1	.3	115	0	2.48	
						110	-5	1.52	
				1	.1	101	-10	1.02	
						90	-15	7.19E-5	
				1	3	77	-20	5.52	
				3	3	66	23	5.32	
				1		124	10	6.73E-4	
						127	0	3.61	
						132	-5	1.88	
				1	1	141	-10	9.26E-5	
						157	-15	4.20	
				1	.3	186	-18	.68	
						209		9.44E-6	

TABLE 6 (CONTINUED)

Mode 3

Mode	Input Volts	Force S Newtons	β₂	Zero Drive	VTVM	Freq Hz	Output db	X/S m/N	ηₙ
3	40	0.050	41	100	3	931	47	5.20E-4	2.15E-3
						932	44	3.68	
				100	3	930	44	3.69	
						930	47.5	5.53	
				30	3	929	40	2.33	
						926	35	1.31	
				10	3	924	30	7.43E-5	
						921	25	4.20	
				3	3	903	20	2.38	
						897	15	1.39	
				1		876	10	7.92E-6	
						866	5	4.67	
				100	3	933	0	2.69	
				30	3	935	40	2.31E-4	
						938	35	1.30	
				10	3	944	30	7.24E-5	
						949	25	4.02	
				3	3	972	20	2.24	
						995	15	1.20	
				1	3	1099	10	6.44E-6	
							0	1.67	
3	20	0.025	81	100	3	931	43.5	6.95E-4	1.50E-3
						932	40.5	4.91	
				100	3	931	40.5	4.93	
				30	3	932	43.5	6.94	
						930	35	2.62	
				10	3	929	30	1.48	
						927	25	8.34E-5	
						924	20	4.72	
3	10	0.0125	162	30	3	931	39	8.29E-4	1.18E-3
						932	36	5.86	
				30	3	931	36	5.87	
						931	39.5	8.78	
				10	3	930	30	2.94	
						931	25	1.66	
						928	20	9.36E-5	
				3	3	925	15	5.30	
						920	10	3.01	

Mode 2

Mode	Input Volts	Force S (Newtons)	β₂	Zero Drive	VTVM	Freq Hz	Output db	X/S m/N	ηₙ
2	30	0.063	32.3	10	3	414	27	1.93E-4	
				3	3	410	20	8.78E-5	
				1	3	408	15	4.99	
				1		396	10	2.99	
					1	386	5	1.76	
				1		375	0	1.05	
					.3	365	-5	6.23E-6	
						362	-10	3.56	
				10	3	354	-15	2.09	
				3	3	352	-20	1.19	
						426	20	8.13E-5	
						436	15	4.37	
						456	10	2.24	
2	40	0.084	24.2	10	3	412	28.5	1.73E-4	2.19E-2
						410	25.5	1.24	
						419	25.5	1.18	
				3	3	409	20	6.59E-5	
						406	10	3.76	
				1		391	10	2.28	
					1	383	0	1.34	
				1		369	-5	8.10E-6	
						361	-10	4.76	
				10	3	356		2.75	
				3	3	429	-20	5.99E-5	
						441	15	3.19	
						457	8	1.33	
2	20	0.042	48.4	10	3	415	25	2.25E-4	1.91E-2
						420	22	1.56	
						412	22	1.62	
				3	3	412	20	1.29	
						411	15	7.27E-5	
				1	3	408	10	4.15	
						394	5	2.50	
						383	0	1.49	
2	5	0.0105	194	3	3	418	18	3.97E-4	6.70E-3
						420	15	2.78	
				1		417	15	2.82	
				1	1	416	10	1.60	
						413	10	9.10E-5	
				3	3	412	0	5.14	
				1		402	-5	3.04	
						386	-10	1.85	
					1	424	10	1.54E-4	
						429	0	8.44E-5	
						436	-5	4.59	
						449		2.44	

TABLE 6 (CONCLUDED)

Mode	Input Volts	Force s (Newtons)	B₂	Zero Drive	VTVM	Freq Hz	Output db	X/S m/N	η_n
4	30	0.027	—	3	1	1314.6	8		
						1316	5		
						1322	10		
				10	1	1335	2:		
				10	3	1346.I	24.5		
						1344.6	21.5		2.90E-3
						1348.5	21.5		
				10	1	1350	20		
						1364	15		
				3	1	1382	10		
						1428	5		
				1	1	1516	0		
						1635	-5		
						1757	-10		
						1822	-15		
1	5	0.016	127	3	3	121.4	14.5	2.36E-3	1.57E-2
						120.7	11.5	1.69	
						122.6	11.5	1.64	
						120	10	1.44	
				1	3	120	5	8.09E-4	
				1		119	0	4.62	
				1	1	116	-5	2.74	
				1	.3	111	-10	1.68	
						105	-15	1.06	
				1	.1	93	-20	7.57E-5	
				3	3	75	-25	6.55	
				1	1	121	10	1.41E-3	
				1		125	5	7.45E-4	
						127	0	4.06	
				1	3	131	-5	2.15	
						138	-10	1.09	
						156	-15	4.79E-5	
						185	-20	1.91	

Mode	Input Volts	Force s (Newtons)	B₂	Zero Drive	VTVM	Freq Hz	Output db	X/S m/N	η_n
3	30	0.0375	—	100	3	931	45	5.51E-4	2.04E-3
						932	42	3.89	
				100	3	930	42	3.91	
						931	45	5.51	
				30	3	930	40	1.68	
						929	35	1.75	
				10	3	927	30	9.89E-5	
						925	25	5.58	
				3	3	923	20	3.15	
						910	15	1.82	
				1	1	903	10	1.06	
				1	1	896	5	6.13E-6	
				1	3	870	-5	3.55	
				100		862	-10	2.03	
				30		851	40	1.17	
						933	35	3.09	
				10	3	938	30	1.73	
						940	25	9.66E-5	
				3	3	946	20	5.41	
						962	15	3.00	
				1	3	995	10	1.63	
						1036	5	8.58E-6	
						1086	0	4.45	
								2.28	
3	10	0.0125	—	1	3	911	5	1.73E-5	
				1	1	897	0	1.00	
						883	-5	5.01E-6	
				30	3	876	-10	3.32	
				10	3	933	30	2.93E-4	
						935	25	1.64	
				3	3	936	20	9.20E-5	
				1		941	15	5.12	
				1	3	948	10	2.84	
				1	1	957	5	1.57	
				1	1	983	-5	8.34E-6	
						1030	-10	4.27	
						1087	-15	2.16	
						1103		1.18	
2	5	.0063	—	30	3	932	35	1.01E-3	1.07E-3
						933	32	7.37E-6	
						932	32	7.39	

TABLE 7

TEST RESULTS FOR BLADE ROOT IN AIR $\overline{N}$ = 17.0 kg (33.4 lb),
CALIBRATION: 7.5 db ≡ 1 g SPRING TYPE 2, LENGTH = 63.5 mm
(2.5 INCHES)

Mode	Input Volts	Force g (Newtons)	B_2	Zero Drive	VTVM	Freq Hz	Output db	X/g m/N	η_n
1	30	0.096	36.0	10	3	124.1	31	2.56E-3	2.42E-2
						123.6	28	1.81	
						126.6	28	1.73	
						123	25	1.30	
						122	20	7.41E-4	
				3	3	120	15	4.31	
				1	3	115	10	2.64	
				1	1	108	5	1.68	
						98	0	1.15	
						97	-5	8.19E-5	
						73	-10	6.55	
				10	3	127	25	1.22E-3	
						130	20	6.53E-4	
				3	3	134	15	3.45	
						139	10	1.81	
				1	1	154	5	8.27E-5	
				1		176	0	3.56	
						216	-2	1.49	
						229	-4	1.67	
						231	0	2.07	
				3	1	233	10	6.43	
1	5	0.016	216	1	1	109	-10	1.74E-4	
				1	3	101	-15	1.14	
						85	-20	9.06E-5	
				1	1	72	-24	7.97	
				3	3	127	15	2.28E-7	
						128	10	1.26	
				1	3	130	5	6.89E-4	
						133	0	3.70	
						138	-5	1.93	
				1		151	-10	9.08E-5	
						172	-15	3.94	
						209	-19	1.68	
						218	-20	1.38	

Mode	Input Volts	Force g (Newtons)	B_2	Zero Drive	VTVM	Freq Hz	Output db	X/g m/N	η_n
1	40	0.128	27.0	10	3	124.1	31.5	2.03E-3	2.02E-2
						123.2	28.5	1.46	
						126.7	28.5	1.38	
						123	25	9.78E-4	
						121	20	5.68	
				3	3	117	15	3.42	
						113	10	2.06	
				1	3	105	5	1.34	
					1	94	0	9.41E-5	
						81	-7	7.37	
						71		7.13	
				10	3	128	25	9.03E-4	
						131	20	4.85	
				3	3	136	15	2.53	
						145	10	1.25	
				1	1	163	0	5.59E-5	
						195	-1	2.19	
						212	5	1.65	
						229		2.82	
1	20	0.064	54.0	10	3	124.6	30	3.39E-3	1.61E-2
						124.0	27	2.42	
						126.0	27	2.35	
						124	26	1.92	
						123	20	1.10	
				3	3	121	15	6.39E-4	
						118	10	3.78	
				1	3	114	5	2.28	
						107	0	1.45	
				1	1	95	-5	1.04	
						81	-10	8.02E-5	
				1	.3	68	-14	7.18	
				10	3	127	25	1.83E-3	
						129	20	1.00	
				3	3	131	15	5.45E-4	

TABLE 7 (CONCLUDED)

Mode	Input Volts	Forces Newtons	δ₂	Zero Drive	VTVM	Freq Hz	Output db	X/S m/n	η_n
2	30	0.071	49	30	1	426.2	32	3.23E-4	1.08E-2
						429.6	29	2.25	
						425.0	29	2.30	
				30	1	427	32	3.22	
						424	25	1.46	
				10	1	421	20	8.33E-5	
						417	15	4.77	
				3	1	409	10	2.79	
						396	5	1.67	
				1	1	384	0	1.00	
						374	-5	5.93E-8	
						366	-10	3.48	
				30	1	432	25	1.41E-4	
						438	20	7.69E-5	
				10	1	445	15	4.19	
						457	10	2.23	
3	30	0.039	—	100	3	933.6	48		1.07E-3
						934.0	45		
						933.0	45		
						933.4	49		
				30	3	933	40		
						931	35		
				10	3	930	30		
						928	25		
				3	3	924	20		
						919	15		
				1	3	907	10		
						895	5		
				100	3	886	0		
				30		935	40		
						936	35		
				10	3	937	30		
						940	25		
				3	3	946	20		
						959	15		
				1	3	979	10		
						1022	5		
						1087	0		

Mode	Input Volts	Force δ (Newtons)	δ₂	Zero Drive	VTVM	Freq Hz	Output db	X/S m/n	η_n
1	20	0.064	54.0	3	3	135	10	2.89E-4	
				1	3	142	5	1.47	
				1	1	161	0	6.42E-5	
						187	-5	2.67	
						225	-9	1.17	
1	10	0.032	100	10	3	125.0	27	4.69E-3	1.04E-3
						124.8	24	3.33	
						126.1	24	3.26	
				3	3	124	20	2.13	
						124	15	1.20	
				1	3	122	10	6.96E-4	
						120	5	4.04	
				1	1	115	0	2.48	
						107	-5	1.61	
				1	3	97	-10	1.10	
						85	-15	8.06E-5	
						73	-19	6.89	
						69	-20	6.88	
				10	3	127	20	2.03E-3	
				3	3	128	15	1.12	
				1	3	131	10	6.03E-4	
						134	5	3.24	
				1	1	139	0	1.69	
						155	-5	7.66E-5	
						179	-10	3.23	
						210	-13	1.66	
						230	-16	9.81E-6	
1	5	0.016	216	10	3	125.8	23	5.85E-3	6.36E-3
						125.4	20	4.16	
				3	3	126.2	20	4.11	
						125	15	2.36	
				1	3	124	10	1.35	
						123	5	7.70E-6	
				1	1	121	0	4.47	
						116	-5	2.74	

TABLE 8

TEST RESULTS FOR BLADE ROOT IN AIR $\overline{N}$ = 25 kg (55.0 lb),
CALIBRATION: 7.5 db ≡ 1 g SPRING TYPE 1, LENGTH = 24.1 mm
(0.95 INCHES)

Mode	Input Volts	Force S (Newtons)	β_2	Zero Drive	VTVM	Freq Hz	Output db	X/S m/N	η_n
1	40	0.128	39.7	10	3	126.8	32.5	2.18E-3	2.68E-2
						126.2	29	1.47	
						129.6	29	1.40	
						125	25	9.46E-4	
				3	3	123	20	5.50	
						120	15	3.25	
				1	3	114	10	2.02	
						107	5	1.29	
				1	1	93	5	9.62E-5	
				10	3	81	0	7.13	
						132	-5	8.49E-4	
				3	1	135	25	4.56	
						142	20	2.32	
				1	1	150	15	1.17	
						173	10	4.96E-5	
						220	0	1.72	
1	20	0.064	79.4	10	3	127.8	30	3.22E-5	1.64E-2
						127.2	27	2.30	
						129.3	27	2.23	
						127	25	1.83	
				3	3	126	20	1.05	
						124	15	6.08E-4	
				1	3	121	10	3.59	
						116	5	2.20	
				1	1	106	5	1.48	
				10	3	97	-5	9.94E-5	
				3	3	81	-10	8.02	
						131	20	9.69E-4	
						176	15	5.06	
				1	3	142	10	2.61	
						150	5	1.31	
				1	1	170	0	5.76E-5	
						203	-5	2.27	

Mode	Input Volts	Force S (Newtons)	β_2	Zero Drive	VTVM	Freq Hz	Output db	X/S m/N	η_n
1	30	0.096	52.9	10	3	127.5	31	2.43E-3	1.96E-2
						127.2	28	1.73	
						129.7	28	1.66	
						126	25	1.25	
				3	3	125	20	7.13E-4	
						122	15	4.21	
				1	3	118	10	2.53	
						112	5	1.58	
				1		100	0	1.11	
						88	-5	8.09E-5	
				10	3	71	-9	7.85	
				3		131	25	1.16E-3	
					3	133	20	6.3E-4	
				1		139	15	3.24	
					3	148	10	1.61	
				1		160	5	7.74E-5	
						191	-2.5	3.06	
						221	0	1.71	
						229		2.13	
1	5	0.016	318	10	1	128.7	21.5	4.70E-3	9.36E-3
						128.3	18.5	3.35	
						129.5	18.5	3.29	
				3	1	128	10	1.26	
				1	1	123	0	4.33E-4	
					3	113	-10	1.62	
				10	1	87	-20	8.65E-4	
				3	3	132	10	1.19E-3	
					1	139	0	3.39E-4	
				1	1	158	-10	8.30E-5	
					3	185	-15	3.40	
				1	3	232	-20	1.22	

TABLE 8 (CONCLUDED)

Mode	Input Volts	Force Newtons	β_2	Zero Drive	VTVM	Freq Hz	Output db	W/S M/N	η_n
2	20	0.046	110	30	3	424.8	32	5.03E-4	8.24E-3
						426.7	29	3.53	
						423.2	29	3.58	
				10	3	424	32	5.04	
						420	20	1.29	
				3	3	412	10	4.24E-5	
				1	3	402	0	1.41	
				1	1	399	-10	4.52E-6	
				10	3	431	20	1.23E-4	
				3	3	451	10	3.54E-5	
				1	3	464	7	2.37	
3	30	0.038	—	100	3	935.1	49		1.92E-3
						935.9	46		
						934.1	46		
				100	3	936	49.5		
				30	1	930	40		
				10	1	920	30		
				3	1	895	20		
				1	1	877	10		
				100	3	937	0		
				30	1	942	40		
				10	1	956	30		
				3	1	1012	20		
				1	1	1102	10		

Mode	Input Volts	Force S (Newtons)	β_2	Zero Drive	VTVM	Freq Hz	Output db	X/S m/N	η_n
1	10	0.032	159	10	3	128.4	26	3.96E-3	1.25E-2
						127.9	23	2.83	
						129.5	23	2.76	
				3	3	128	20	2.00	
						127	15	1.14	
				1	3	125	10	6.63E-4	
						123	5	3.85	
				1	1	117	0	2.39	
						109	-5	1.55	
						97	-10	1.10	
				1	3	86	-15	7.87E-5	
						70	-20	6.68	
				10	3	130	20	1.94E-3	
				3	3	132	15	1.06	
						135	10	5.68E-4	
				1	3	139	5	3.01	
						147	0	1.52	
				1	1	164	-5	6.85E-5	
						197	-10	2.67	
						230	-13	1.39	
2	30	0.069	73.6	30	3	424.7	34	4.22E-4	1.02E-2
						427.0	31	2.96	
						422.7	31	3.02	
				30	3	425	35	4.73	
				10	3	423	30	2.68	
				3	3	417	20	8.73E-5	
				1	1	407	10	2.90	
				1	1	400	0	9.49E-6	
				1	1	398	-10	3.03	
				30	3	427	30	2.63E-4	
				10	3	436	20	7.99E-5	
				3	3	462	8	1.79	

TABLE 9

TEST RESULTS FOR BLADE ROOT IN WATER $\bar{N}$ = 10 kg (22.0 lb), CALIBRATION: 7.5 db ≡ 1 g SPRING TYPE 2, LENGTH = 63.5 mm (2.5 INCHES)

Mode	Input Volts	Force S (newtons)	β_2	Zero Drive	VTVM	Freq Hz	Output db	X/S m/N	η_n
1	10	0.032	42.3	3	3	120	18	1.81E-3	2.83E-2
						119	15	1.30	
				3	3	123	15	1.22	
						120	18	1.81	
						119	15	1.30	
				3	1	119	10	7.31E-4	
						117	5	4.25	
						114	0	2.52	
				1	1	108	-5	1.58	
						98	-10	1.08	
				1	.3	84	-15	8.25E-5	
						67	-20	7.29	
				3	3	123	15	1.22E-3	
				3	1	126	10	6.52E-4	
						130	5	3.45	
				1	1	136	0	1.77	
						148	-5	8.41E-5	
						168	-10	3.67	
				1		197	-15	1.50	
					.3	230	-20	6.19E-6	
1	5	0.016	84.7	3	3	121	15.5	2.66E-3	1.73E-2
						121	12.5	1.89	
						123	12.5	1.83	
1	20	0.064	21.2	3	3	118	18	9.34E-4	
						117	15	6.73	
				3	1	116	10	3.85	
						111	5	2.36	
				1	1	102	0	1.57	
						93	-5	1.06	
						77	-10	8.73E-5	
				1	.3	59	-15	8.36	
						48	-20	7.11	
				3	3	126	15	5.80E-4	
						127	10	3.21	
				3	1	140	5	1.49	
						156	0	6.93E-5	
				1	1	172	-5	2.87	
						209	-9	1.33	

Mode	Input Volts	Force S (Newtons)	β_2	Zero Drive	VTVM	Freq Hz	Output db	X/S m/N	η_n
1	30	0.096	14.1	3	3	117	19.5	7.53E-4	
						115	15	4.64	
				3		112	10	2.75	
					1	105	5	1.76	
				1		95	-5	1.21	
					1	81	-10	9.36E-5	
				1	3	59	-10	9.92	
				3	3	52	15	7.18	
						118	15	3.75E-4	
				3	2	134	5	1.92	
						148	5	8.86E-5	
				1	1	170	-5	3.78	
						197		1.58	
1	40	0.128	10.6	3	3	115	19.5	5.94E-4	
						113	15	3.66	
				3		109	10	2.21	
					1	100	5	1.48	
				1	1	87	0	1.10	
						75	-5	8.31E-5	
					3	56	-10	8.39	
				3	3	130	15	2.77E-4	
				1		143	10	1.29	
						159	5	5.85E-5	
				3	1	182	5	2.51	
				1		202	-3	1.44	
1	2	0.0064	212	1	3	122.5	9.2	3.36E-3	1.39E-2
						122.1	6.2	2.39	
						123.8	6.2	2.33	
						122	5	2.09	
				1	.3	120	0	1.17	
						118	-5	6.82E-4	
				1	.1	112	-15	3.97	
						104	-20	2.48	
				1		84	-25	1.61	
						63	-28	1.39	
				3	3	126	0	1.75	
				1	1	128	-5	1.10E-3	
				1	1	132	-10	5.99E-4	
				1	.3	140	-15	3.17	
						155	-20	1.58	
				1	.1	190	-25	7.27E-5	
								2.72	

TABLE 9 (CONTINUED)

Mode	Input Volts	Force Newtons	β_2	Zero Drive	VTVM	Freq Hz	Output db	W/S M/N	η_n
3	20	0.033	-	100	3	933.6	44		1.39E-3
						933.0	.41		
				100	3	934.3	41		
					1	934	43		
				100	1	933	40		
						932	35		
				30	1	930	30		
						928	25		
					1	926	20		
				10	1	916	15		
				10	1	911	10		
				3		888	5		
						877	0		
				1	1	870	5		
				100	3	934	40		
				100	1	936	35		
						939	30		
				30	1	942	25		
						949	20		
				10	1	960	15		
						983	10		
				3	1	1027	5		
						1088	0		
3	10	0.016	-	30	3	934.1	39		1.07E-3
						933.9	.36		
						934.9	36		
				30	3	934	39		
					1	933	30		
				30	1	931	25		
						929	20		
				10	1	925	15		
						918	10		
				3	1	905	5		
						891	0		
				1	1	880	-5		
						872	-10		
				30	3	936	30		
				30	1	939	25		
						942	20		
				10	1	947	15		
						957	10		
				3	1	976	5		
						1013	0		
				1	1	1060	-5		
						1100	-10		

Mode	Input Volts	Force Newtons	β_2	Zero Drive	VTVM	Freq Hz	Output db	W/S M/N	η_n
2	40	0.080	16.9	10	3	423.6	29.5	2.18E-4	2.41E-2
						421.4	26.5	1.56	
						431.6	26.5	1.49	
					3	419	20	7.46E-5	
				3		414	15	4.30	
					1	403	10	2.55	
				3		384	5	1.58	
					1	367	0	9.72E-6	
						362	-5	5.62	
				1		355	-10	3.29	
					3	352	-15	1.88	
				1	3	448	20	6.53E-5	
				10	3	476	15	3.25	
				3		512	10	1.58	
					1	564	5	7.32E-6	
				1		616	0	3.45	
2	30	0.060	22.6	10	3	425	28	2.43E-4	
						423	25	1.74	
				3	3	421	20	9.85E-5	
					3	417	15	5.65	
				1		408	10	3.32	
						392	5	2.02	
				1	1	376	0	1.24	
						366	-5	7.33E-6	
						358	-10	4.31	
2	30	0.060	22.6	1	3	354	-15	2.48E-6	
				10	3	350	-20	1.43	
						434	-25	1.65E-4	
				3	3	444	20	8.86E-5	
						462	16	5.16	
					1	471	10	4.43	
				3		490	10	2.30	
						538	5	1.07	
						596	0	4.92E-6	

106

TABLE 9 (CONCLUDED)

Mode	Input Volts	Force Newtons	β_1	Zero Drive	VTVM	Freq Hz	Output db	W/S M/N	η
3	2	0.003	—	10	3	935.8	24		1.60E-3
						935.0	.21		
					3	936.5	21		
				10		935	25		
					1	934	20		
				10		933	15		
				3	1	932	10		
						930	5		
				1	1	924	0		
						917	-5		
				1	.3	912	-10		
						891	-15		
				10	3	879	-20		
				3	3	937	20		
						938	15		
				3	1	940	10		
						943	5		
				1	1	946	0		
						960	-5		
				1	.3	971	-10		
						1024	-15		
						1081	-20		

Mode	Input Volts	Force Newtons	β_2	Zero Drive	VTVM	Freq Hz	Output db	W/S M/N	η_n
3	40	0.065	—	100	3	932.5	49		2.04E-3
						932.0	46		
					1	933.9	46		
						931	40		
				100		930	35		
					1	927	30		
				30		922	25		
					1	913	20		
				10		901	15		
					1	886	10		
				3		876	5		
				100	1	936	40		
				100	3	938	35		
				30		943	30		
					1	952	25		
						965	20		
				10	1	989	15		
				3	1	1036	10		
						1091	5		
3	30	0.049	—	100	3	932.7	47.5		1.82E-3
						932.4	44.5		
						934.1	44.5		
				100	3	933	47		
						932	40		
				100	1	931	35		
						929	30		
				30	1	924	25		
						917	20		
				10	1	907	15		
						893	10		
				3		879	5		
					1	871	0		
				100	3	935	40		
				100	1	938	35		
				30		941	30		
					1	944	25		
						957	20		
				10	1	973	15		
						1014	10		
				3	1	1065	5		

TABLE 10

TEST RESULTS FOR BLADE ROOT IN WATER; N = 17 kg (33.4 lb)
CALIBRATION: 7.5 db = 1 g; SPRING TYPE 2; LENGTH = 63.5 mm
(2.5 INCHES).

Mode	Input Volts	Force Newtons	β_2	Zero Drive	VTVM	Freq Hz	Output db	W/S M/N	η_n
1	20	0.064	36	10	3	123.5	25		3.16E-2
						122.5	22		
						126.4	72		
				10	1	123	26		
				10	1	122	20		
					1	121	15		
					1	117	10		
				3	1	111	5		
				1	1	101	0		
					1	90	-5		
					1	76	-10		
				10	3	128	20		
				10	1	132	15		
					1	138	10		
				3	1	151	0		
					1	170	-5		
				1	1	205			
1	10	0.032	72	10	3	124.4	23		1.77E-2
						126.2	20	2.96E-3	
				10	3	124	20	1.20	
				10	1	123	15	6.84E-4	
				3	.2	119	5	4.11	
						115	0	2.48	
				1	1	107	-5	1.61	
					.3	98	-10	1.08	
				1	.3	83	-15	8.45E-5	
				10	1	129	15	1.11E-3	
						131	10	1.03E-4	
				3	1	136	5	3.15E-5	
					1	138	0	1.72	
				1	1	160	-5	7.19E-5	
				1	1	186	-10	2.99	
				1	.3	223	-14	1.31	
1	2	0.0064	360	3	3	126.6	14	5.12E-3	1.11E-2
						126.3	11	3.64	
				3	1	127.7	11	3.56	
						126	5	1.83	
				1	1	125	0	1.05	
						123	-5	6.09E-4	
				1	.3	118	-10	3.72	
						113	-15	2.28	
				1	.1	102	-20	1.57	
				3	1	88	-25	1.19	
				1	1	130	5	1.72E-3	
						131	-5	9.54E-4	
				1	.3	134	-10	5.13	
						139	-15	2.68	
				1	1	149	-20	1.31	
						170	-24	5.67E-5	
						203		2.51	

Mode	Input Volts	Force Newtons	β_2	Zero Drive	VTVM	Freq Hz	Output db	W/S M/N	η_n
1	40	0.126	18.3	10	3	122.6	27		5.22E-2
						121.1	24		
				10	3	127.5	24		
				10	1	122	28		
					1	120	20		
				3	1	117	15		
						111	10		
				1	1	100	5		
						88	0		
				10	3	73	-5		
				10	1	56	-10		
					1	131	20		
				3	1	139	15		
						151	10		
						174	5		
						208	1		
1	30	0.096	24	10	3	124.0	26		4.68E-2
						121.4	23		
				10	3	127.2	23		
				10	1	123	27		
					1	121	20		
				3	1	116	15		
						105	10		
				1	1	95	5		
						81	0		
				10	3	71	-9		
				10	1	129	20		
						135	15		
				3	1	144	10		
						162	5		
				10	3	192	0		
				10	1	123	27		
						121	20		
				3	1	119	15		
						114	10		
				1	1	105	5		
						94	0		
						83	-5		
				10	3	62	-10		
				10	1	130	20		
						135	15		
				3	1	141	10		
						162	5		
						185	0		

TABLE 10 (CONCLUDED)

Mode	Input Volts	Force Newtons	β₂	Zero Drive	VTVM	Freq Hz	Output db	W/S M/N	η_n
3	2	0.003	-	10	3	935.8	24		1.60E-3
						935.0	21		
						936.5	21		
				10	3	935	25		
						934	20		
				20	1	933	15		
						932	10		
				3	1	930	5		
						924	0		
				2	1	917	-5		
						912	-10		
				1	.3	891	-15		
						879	-20		
				10	3	937	20		
				3	3	938	15		
						940	10		
					1	943	5		
				2	1	946	0		
						960	-5		
				1	.3	971	-10		
						1024	-15		
						1081	-20		

Mode	Input Volts	Force Newtons	β₂	Zero Drive	VTVM	Freq Hz	Output db	W/S M/N	η_n
2	20	0.040	34	10	3	428	25	2.54E-4	
				10	1	426	20	1.44	
				3	1	423	15	8.23E-5	
				3	1	420	10	4.70	
				1	1	406	5	2.83	
				1		389	0	1.73	
						373	-5	1.06	
				10	3	363	-10	6.29E-6	
				10	1	439	20	1.36E-4	
						449	15	7.31E-5	
				3	1	473	10	3.70	
						500	5	1.86	
				3		542	0	8.92E-6	
				1	2	601	-5	4.08	
						638	-10	2.04	
2	10	0.020	68	3	3	432.8	20.5	2.96E-4	1.53E-2
						431.1	17.5		
						437.7	17.5		
				3		433	20		
						430	15		
					1	427	10		
				3	1	420	5		
						415	0		
						393	-5		
				1	3	377	-10		
					3	365	-15		
				1		443	15		
						452	10		
				3		470	5		
						495	0		
				1		532	-5		
				1		594	-10		
				1	3	629	-15		
						682	-20		
2	2	0.004	339	1	3	441.2	9	3.79E-4	1.30E-2
				3	1	439.1	6	2.71	
					1	448.6	6	2.60	
						441	9.5	4.02	
						438	5	2.43	
				1		436	0	1.38	
						431	-5	7.93E-5	
				1	.3	422	-10	4.65	
2	2	0.004	339	1	3	409	-15	2.78E-5	
				1	1	405	-20	1.60	
				3	1	374	-25	1.05	
				3		447	5	2.33E-4	
				1		449	0	1.30	
				1		459	-5	6.99E-5	
				1		473	-10	3.70	
						500	-15	1.85	
					.3	549	-20	8.69E-6	

S = 0.032N, $\overline{N}$ = 10kg, 115.8 Hz

S = 0.128N, $\overline{N}$ = 10kg, 116.5 Hz

Figure 102. Waveforms (Water)

S = .038N, $\overline{N}$ = 10kg, 934.1 Hz

S = .096N, $\overline{N}$ = 10kg, 119.3Hz

S = .067N, $\overline{N}$ = 25kg, 665.9 Hz

S = .096N, $\overline{N}$ = 25kg, 127.5 Hz

Figure 101. Waveforms (Air)

Finally, the experiments are compared with analysis in Figures 103
to 107.

6. DIRECT MEASUREMENT OF MODAL MASS AND STIFFNESS

Section 2.3 describes the linear modal analysis of blade response
without slip (fully clamped root). From this analysis the observed
resonant peak acceleration at the point 0,0 of the blade, when excited at
the same point by a force S, is:

$$|X_1| = \frac{SL^2 \cos\alpha}{I_1 \eta_1 \omega_1^2}$$

$$I_1 = \frac{SL^2 \cos\alpha}{\eta_1 \omega_1^2 |X_1|} = \frac{SL^2 \cos\alpha}{\eta_1 |\ddot{X}_1|} \tag{127}$$

From Figures 93 to 97 for the fundamental mode, S and $|X_1|$ at low force
levels, where slip does not occur, are known. η_1 is the observed modal
damping and ω_1 is the observed resonant frequency. Table 11 gives the
collected results. It is seen that $I_1 \simeq 1.04 \times 10^{-3}$ kgm^2 and $K_1 (=I_1 \omega_1^2) =$
635 Nm/m. These values are very close to those determined from the
measured mode shapes.

7. MEASURED MODAL DAMPING

Further understanding of the test results is afforded by examining the
apparent modal damping $\eta_1' = \Delta f/f_1$, where f_1 is the resonance frequency and
Δf is the frequency 3 db below peak amplitude (3.01 db actually). Clearly,
since the system behavior is highly nonlinear, this linear system repre-
sentation is not particularly appropriate except as a crude numerical
indicator of the effect of slip. Even so, a graph of η_1' versus $1/\beta_2$ is
most informative, as Figure 108 shows. It appears that the graph of η_1'
versus $S/\mu\bar{N}$ is nearly a straight line, for each fluid, terminating with
a discontinuity at $\eta_1 = 0.01$ (the linear damping) and finite values of
$S/\mu\bar{N}$. The agreement between analysis and experiment is good.

Figure 104. Comparison of Measured and Predicted Response in Mode 1 ($\overline{N}$ = 17 kg, Air)
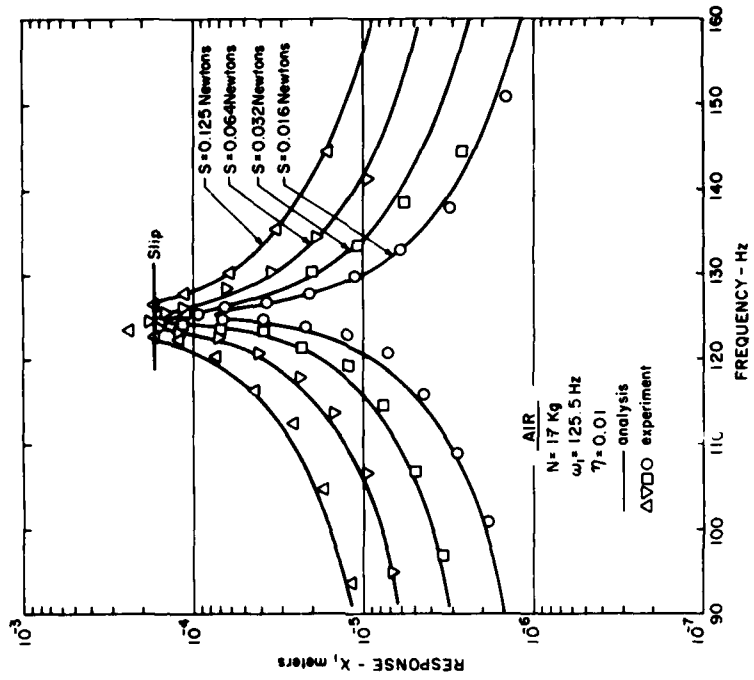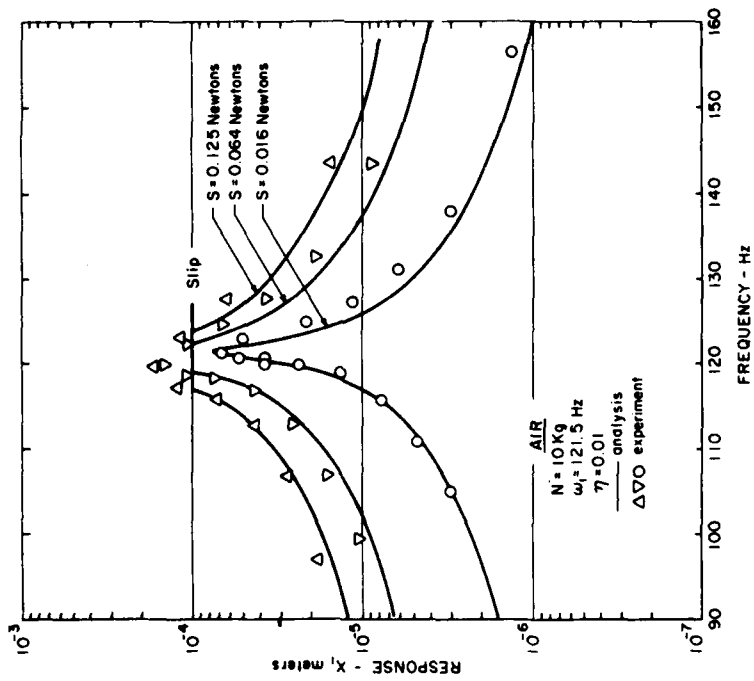
Figure 103. Comparison of Measured and Predicted Response in Mode 1 ($\overline{N}$ = 10 kg, Air)
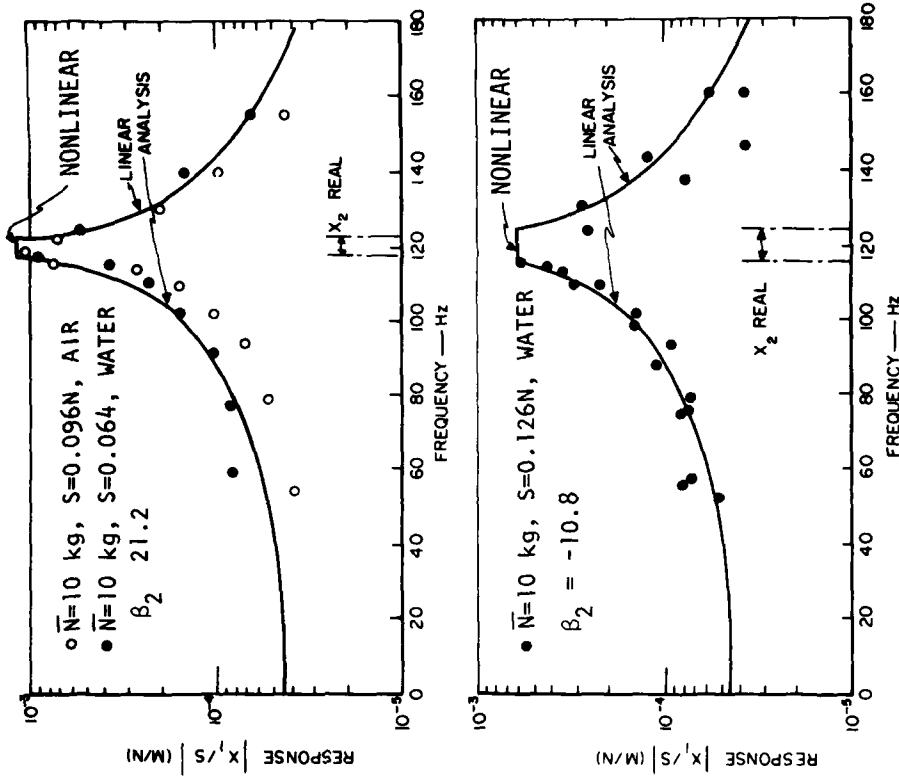
Figure 106. Measured and Predicted Response in Mode 1
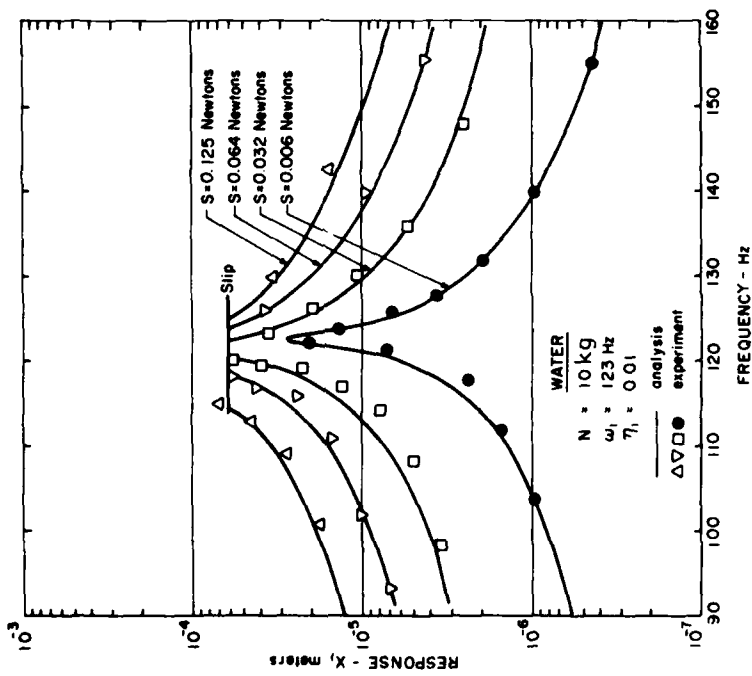
Figure 105. Comparison of Measured and Predicted Response in Mode 1 ($\overline{N}$ = 17 kg, Water)

113
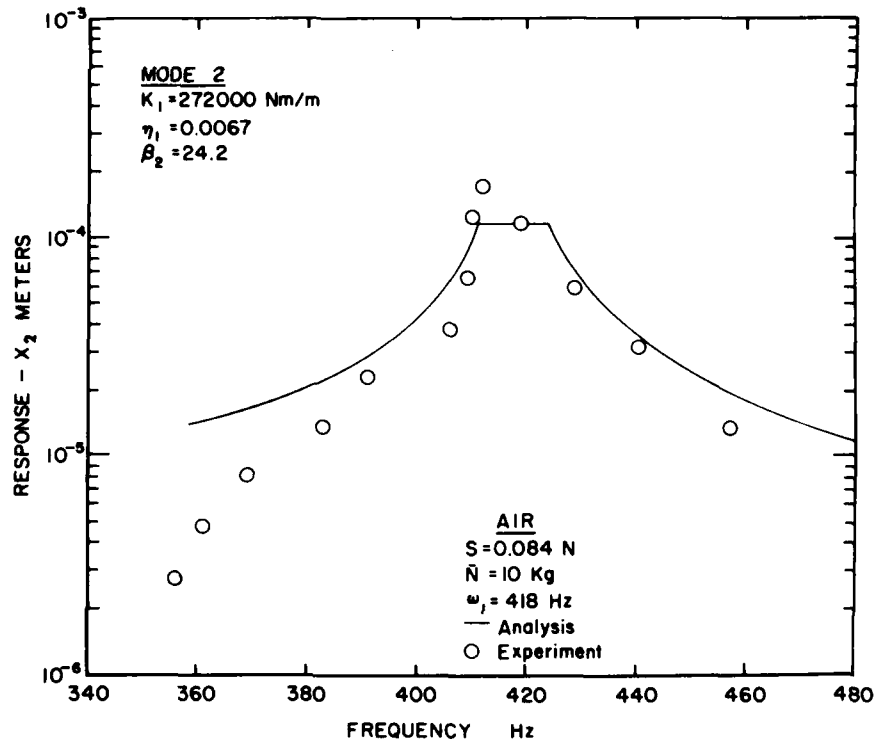
Figure 107. Measured and Predicted Response for Mode 2
(S = 0.084 Newtons, $\overline{N}$ = 10 kg, Air)

TABLE 11

MODAL PARAMETERS FOR MODE 1

FLUID AT ROOT	$\bar{N}$ (kg)	S (Newtons)	$\ddot{X}_1$ (g's)	ω_1 (Hz)	η_1	I_1 (kgm^2)	K_1 (Nm/rad)
AIR	17	0.016	5.96	125.8	6.36×10^{-3}	1.25×10^{-3}	778
	25	0.016	5.01	128.7	9.32×10^{-3}	1.01×10^{-3}	662
WATER	10	0.0064	1.216	122.5	1.32×10^{-2}	1.11×10^{-3}	663
	17	0.0064	2.114	126.6	1.11×10^{-2}	0.805×10^{-3}	510

115

Figure 108. Measured and Predicted Damping Versus $1/\beta_2$

Finally, for very low load levels the residual damping is linear and apparently hysteretic in nature, and its source is possibly the blade material itself. For the first mode $\eta_1 = 0.01$ at about 120 Hz. Further tests on the second and third modes show that $\eta_2 = 0.006$ and $\eta_3 = 0.0015$ for the second and third modes, at 420 Hz and 920 Hz, respectively. This variation of η_n with frequency is again fairly consistent with published data for such damping.
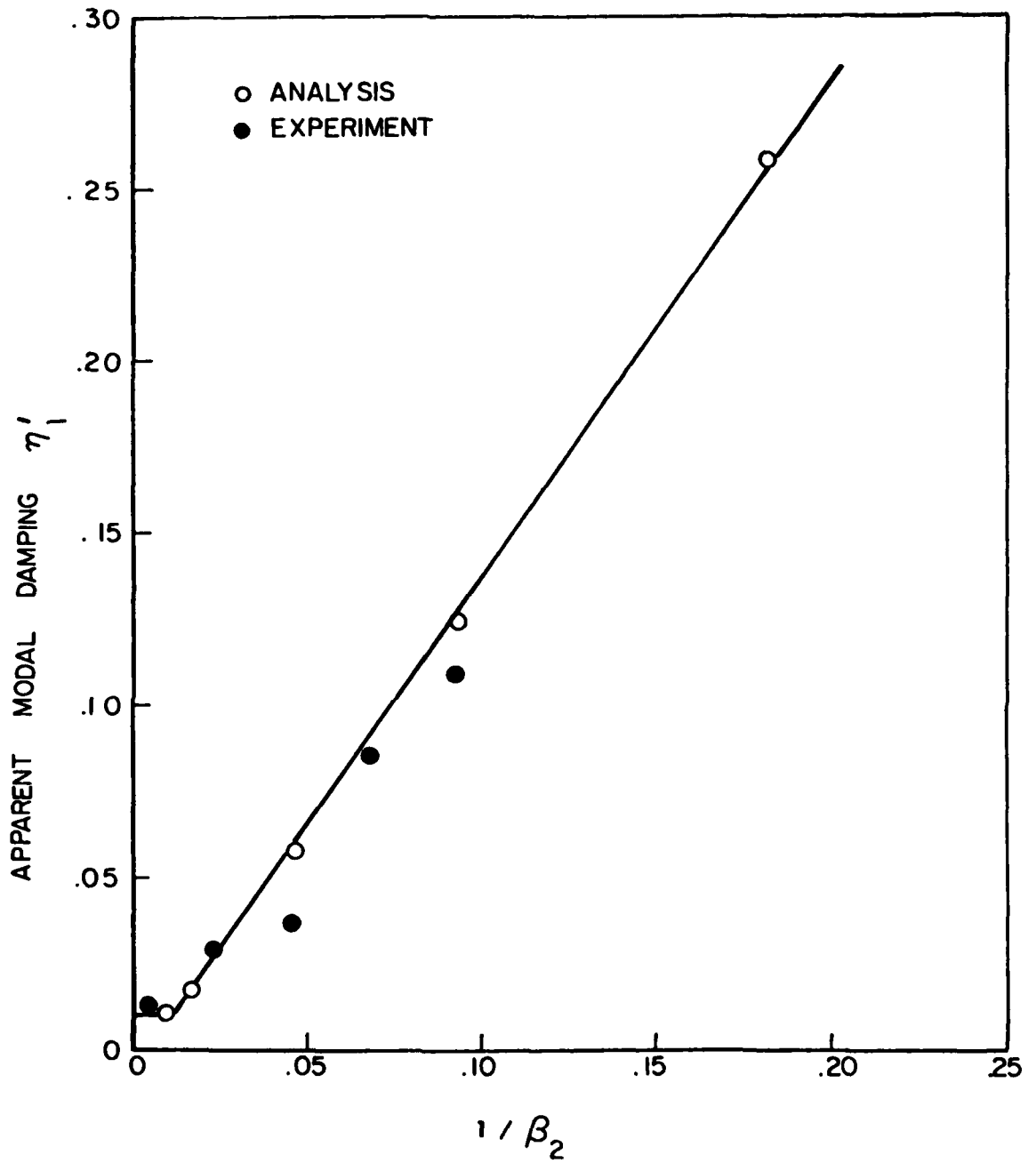
8. CALIBRATION OF TEST SYSTEM

In order to be able to conduct quantitative measurements of the response of the blade to a known harmonic force, it is necessary to calibrate the measurement and excitation systems. For example, the voltage across the fixed resistor in the exciter/oscillator system, at the load terminals, must be monitored and related in some way to the force applied to the blade. Similarily, the signal from the accelerometer, after passing through the line driver, the charge amplifier and the various cables is read at the voltmeter, and the relationship between this voltage and the actual acceleration must be determined for the particular system and components used. This is the aim of the calibration procedures, which must be conducted prior to testing and from time to time thereafter.

The accelerometer-Zero Drive-Charge Amplifier-Voltmeter measurement chain is calibrated by introducing a known harmonic acceleration at the accelerometer and simply observing the R.M.S. (root mean square) voltage registered at the voltmeter. The known acceleration is generated by a small electrodynamic shaker, having a steel ball embedded in a hollow cavity in the shaker table, as illustrated in Figure 109 (step 1). At an acceleration of just over 1 g at the table, the steel ball will separate from the floor of the cavity and impacts occur. These are easily noted as "hash" on the otherwise smooth sinusoidal trace on the oscilloscope screen. The acceleration at the shaker table is adjusted until the "hash" just appears. Hence, the accelerometer is calibrated to 1 g. For the Endevco 22 accelerometer, MB Zero Drive and Amplifier, and HP 3400A voltmeter, this calibration was:

$$1 \text{ g} = 1.91 \text{ volts (8 db)}$$

117
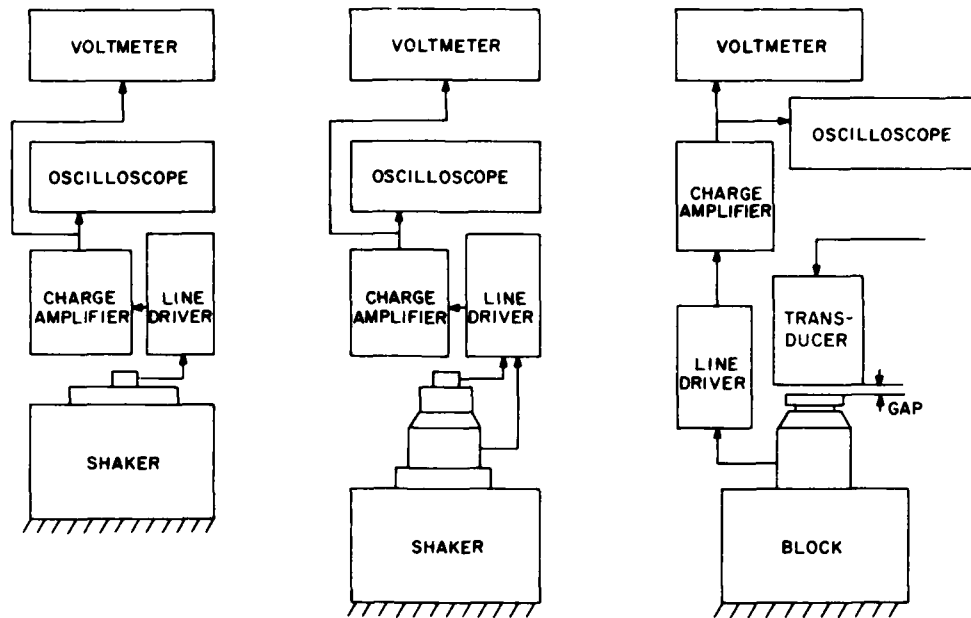
Figure 109. Calibration Setups

For the Endevco Type 2226 accelerometer used in the calibration of the transducer, the appropriate calibration was:

$$1 \text{ g} \equiv 7.60 \text{ volts } (17.6 \text{ db})$$

In order to calibrate the transducer, it was necessary to measure the force generated on a block of iron placed a distance h (the gap) from the active end of the transducer and having a certain oscillating voltage V at the output terminals, corresponding to a definite current in the circuit. A three step process is necessary, since the force cannot be measured directly. Figure 109 shows the three steps in this sequence.

The first step is to calibrate the accelerometer, as discussed already. When this step has been accomplished, one has a numerical relationship between the acceleration seen by the accelerometer and the voltage registered by the voltmeter, in volts or decibels with 0.707 volts = 0 db, because this is an R.M.S. voltmeter.

The second step was to calibrate the impedance head, so that it in turn can be used to measure force. This was accomplished by applying a known acceleration, using the results of step 1, to a shaker table supporting the impedance head. The force experienced by the crystal of the impedance head is equal to $(M_0 + \Delta M)\ddot{X}$, the d'Alembert force corresponding to the acceleration $\ddot{X}$ acting on the mass $M_0 + \Delta M$ above the crystal. M_0 is the built-in mass of the impedance head itself and ΔM is the added mass of the soft iron piece. Since M_0 may not be known, one can vary the mass ΔM and measure the output voltage V_S of the force gage, registered at the voltmeter for each case. With $\ddot{X}$ known from the corresponding accelerometer reading, we can then plot a graph of $V_S/\ddot{X}$ against Δm for the particular force gage used (Wilcoxon Z 602). The intersection of the line defined by the measured points with the negative ΔM axis corresponds to the mass M_0 of the impedance head above the crystal. With M_0 then known, any reading of $(M_0 + M)\ddot{X}$ gives the force corresponding to the acceleration $\ddot{X}$ and the voltage output V_S from the force gage, via the charge amplifier, the zero drive and the cables. It was found that $M_0 = 30$ grams. Hence one has the calibration; for example, for $V_S = 13.5$ volts, $\Delta m = 11.5$ grams, the acceleration $\ddot{X}$ was 0.168 g's. Therefore:

$$13.5 \text{ volts} \equiv \frac{(11.5 + 30)}{1000} \times 0.168 \times 9.81 \text{ Newtons}$$

or

$$1 \text{ volt} \equiv 5.08 \times 10^{-3} \text{ Newtons} \tag{128}$$

This result is dimensioned properly by converting M_0 and ΔM to kilograms and the acceleration (0.168 g's) to meters per second.

The third step is to calibrate the transducer itself, using the force gage. The force gage was placed on a rigid block and the transducer was then brought close to the iron block, with separation h as shown in Figure 109, step 3. The voltage V, corresponding to a particular level of the oscillator current in the transducer coils, is set at a particular value, such as 30 volts. The gap is set at a particular value, in this case 0.043 inches (1.092 mm), by means of a feeler gage or a metal sheet

119

of this thickness. The force gage was then connected, again through the same zero drive, charge amplifier, and cables to the voltmeter. From the force gage calibration, given in Equation 128, the force was then calculated directly from the observed voltage. The test data supports the assumption that $S \sigma V$, but only one gap setting was tested so that the other assumption, namely $S \sigma 1/h$, was not verified. However, the same gap was used in all tests, so this omission was not too important. The variation of Sh/V with frequency is shown in Figure 110. One can therefore estimate S for any given frequency and voltage for the particular gap setting.

The effective centrifugal load on the blade was provided by two springs. This force was determined by measuring the change in length of the springs under load, and this in turn was calibrated by applying known static loads to each spring in turn and measuring the corresponding length.

9. TESTS ON BLADE WITH SLIP AT A PLATFORM

With the specific blade used in the earlier experiments on blade root damping, the use of a gravity loaded rod in a guide allowed a controlled frictional load to be applied at selected points, as illustrated in Figures 111 and 112. The same magnetic transducer and pickup accelerometer were used as in the previous tests, and the gap between transducer and blade was set at 0.040 inches (1.02 mm) as before. Hence, all calibration factors were unchanged. The distance X was 2.25 inches (57.2 mm), and at this point ϕ_1 (X/L) = 0.20, as shown in Figure 90. The blade was excited at various force levels and for various normal loads as before. The results are summarized in Table 12. Figure 113 shows typical plots of response versus frequency for the undamped blade and for a normal load of 1.70 kilograms. For purposes of comparison with the analysis of Section 3, we note that the mode shape in the fundamental mode would not change too much, so that $M_1 \simeq 0.036$ kilogram as before. For the blade without the normal load, the stiffness K_e is the same as before, i.e., K_e = 22,500 N/m.

The change in resonant frequency from about 125 Hz (unloaded) to 148 Hz loaded, leads to $K_1 = 30,600$ N/m. The value $R_1 = 0.2$ corresponds to the modal amplitude $\phi_1 (5.72/20) \simeq 0.20$. It is seen that analysis and experiment agree quite well. A friction coefficient $\mu = 0.3$ was determined for slip between the rod and the blade leading edge.
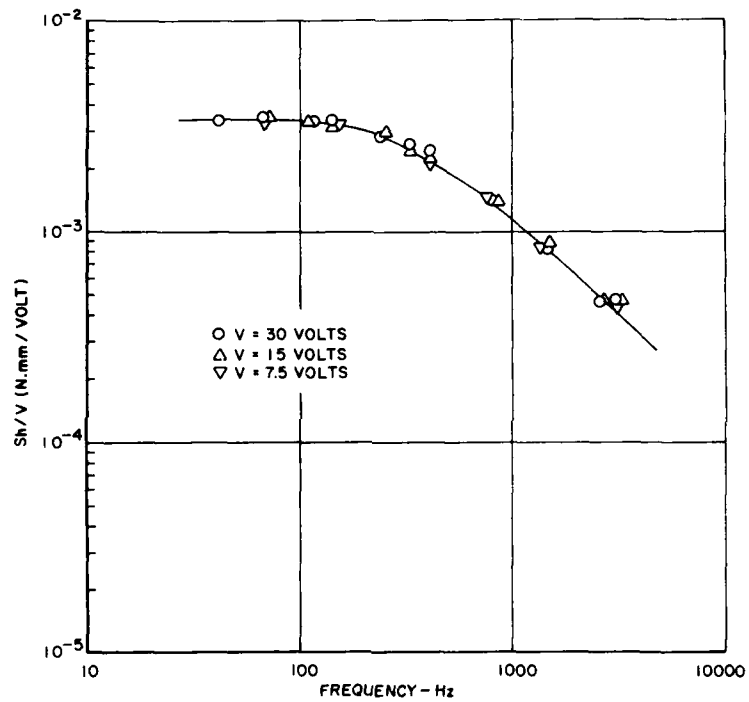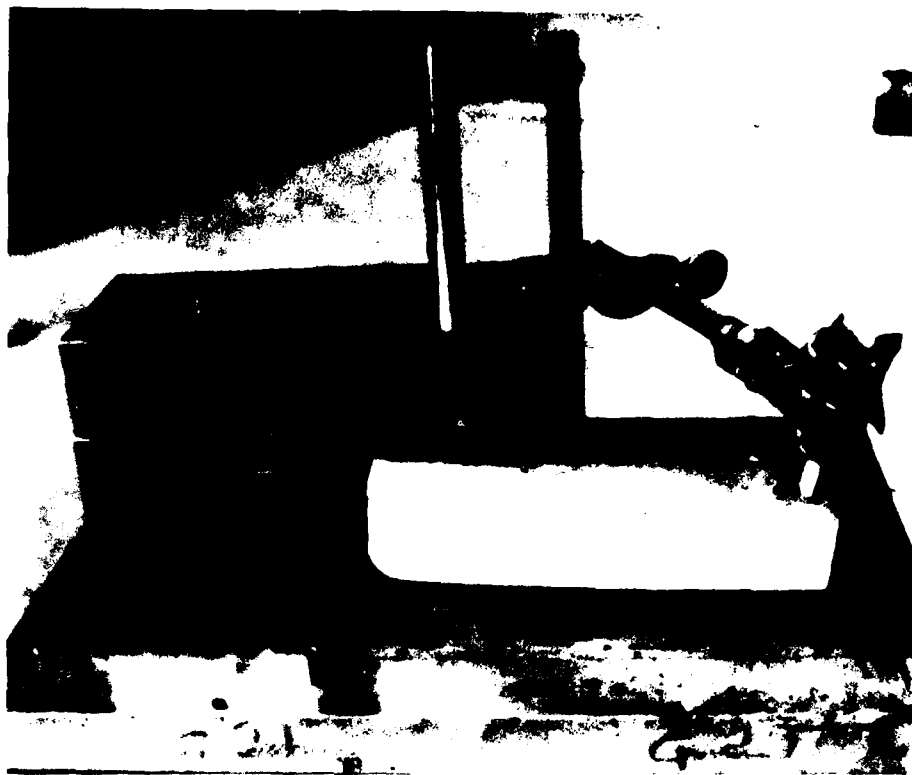

Figure 110. Calibration Curve for Transducer

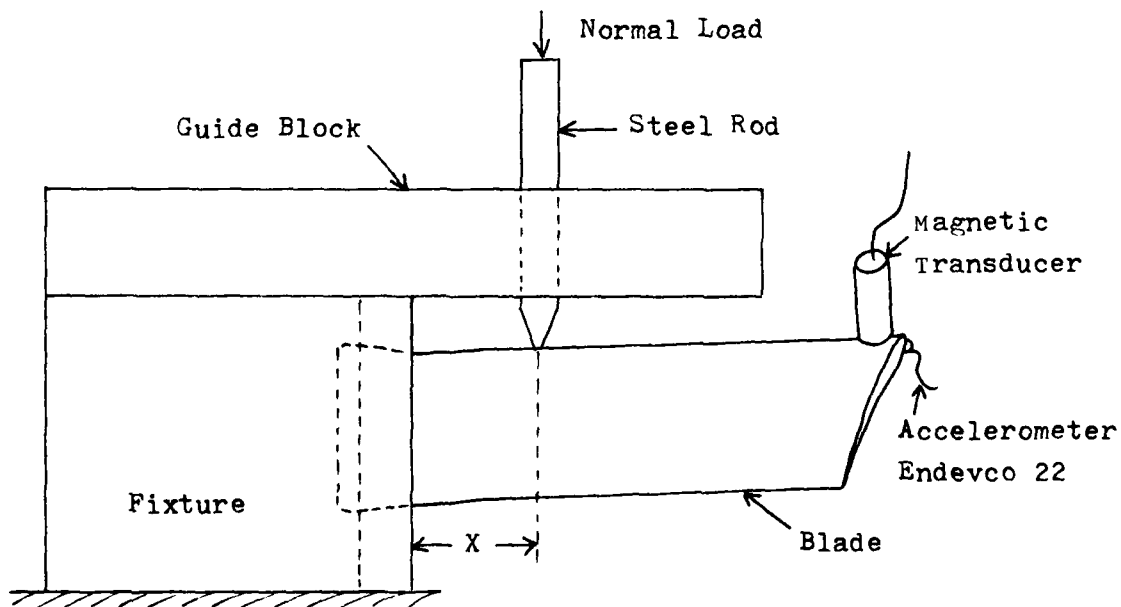Figure 111.   Blade in Test Fixture

Figure 112.   Test Fixture

122

TABLE 12

TESTS ON BLADE WITH SLIP AT "PLATFORM"

MODE 1, X = 2.25 in (57.15 mm), R_1 = 0.20

Input (volts)	$\bar{N}$ (kg)	Force S Newtons	$\frac{\alpha_1}{S}$	Freq (HZ)	Response (volts)	X_1 (metres)	η'_1
40	0	0.079	0	127	3.75	7.70E-5	0.024
				126	2.5	5.21	
				129	2.5	4.98	
				130	2.0	3.92	
				133	1.0	1.87	
				139	0.50	8.57×15^{-6}	
				159	0.20	2.62	
				194	0.10	8.80×10^{-7}	
				171	0.15	1.70×10^{-6}	
				152	0.25	3.59	
				127	4.0	8.22E-5	
				125	2.0	4.24	
				123	1.0	2.19	
				118	0.5	1.19	
				107	0.2	5.79E-6	
				95	0.1	3.67	
				74	0.05	3.03	
				48	0.023	3.31	
				20	0.017		
				40	0.02		
40	1.70	0.079	11.2	147	1.50	2.30E-5	0.0612
				143	1.05	1.70	
				152	1.05	1.51	
				153	1.00	1.42	
				162	0.50	6.31E-6	
				185	0.20	1.94	
				222	0.10	6.72E-7	
40	3.52	0.079	23.1	149	3.20	4.78E-5	0.0338
				146	2.40	3.73	
				151	2.40	3.49	
				152	2.00	2.87	
				155	1.00	1.38	
				164	0.50	6.16E-6	
				191	0.20	1.82	
				226	0.10	6.49E-7	
				147	4.00	6.13E-5	
				146	3.00	4.66	
				146	2.00	3.11	
				143	1.00	1.62	
				138	0.50	8.70E-6	
				123	0.20	4.38	
				103	0.10	3.12	
				82	0.05	2.46	
				43	0.02	3.58	

TABLE 12 (CONCLUDED)

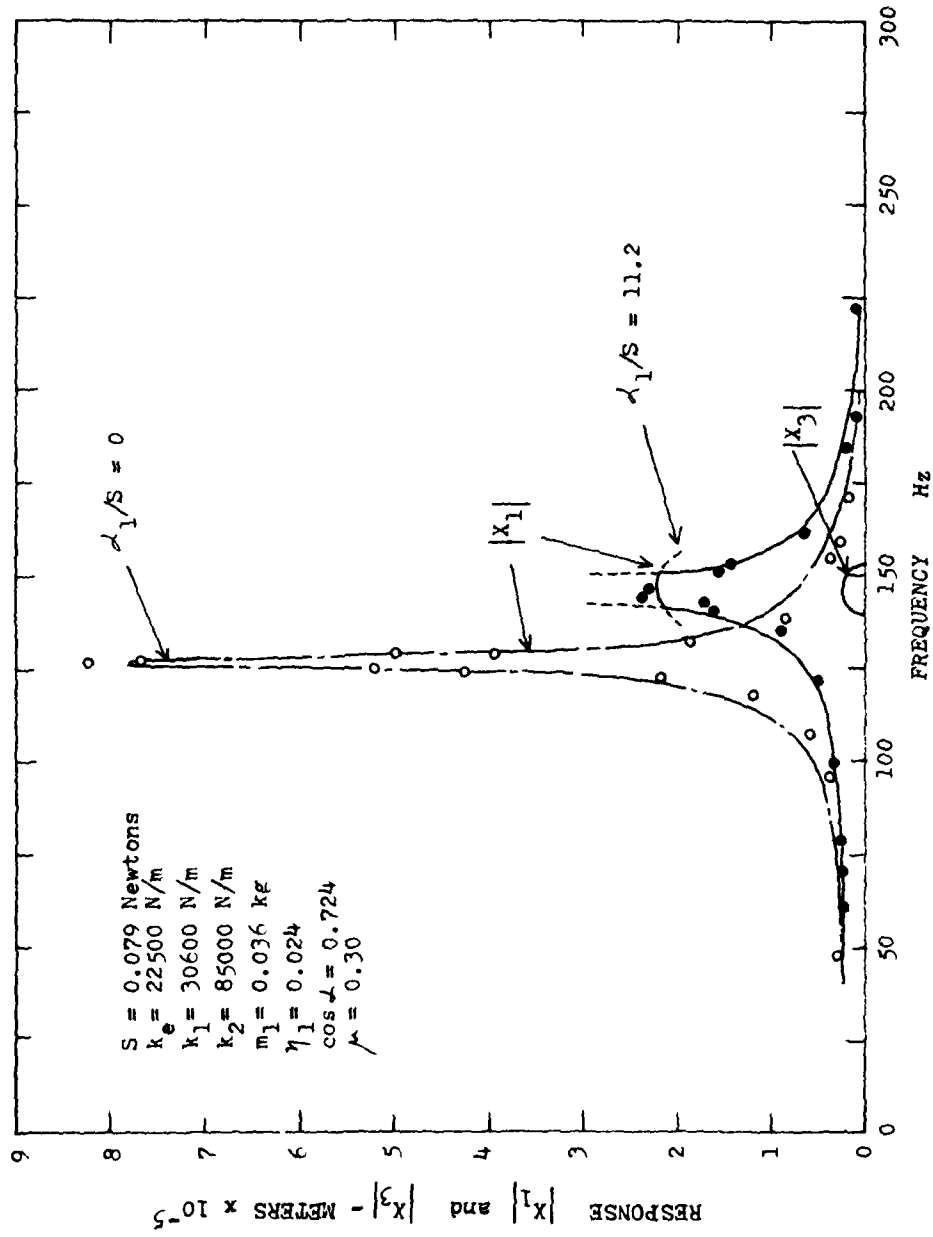| Input (volts)	$\bar{N}$ kg	Force S N	$\frac{\alpha_1}{S}$	Freq (HZ)	Response (volts)	X_1 (m)	η_1'
40	2.61	0.079	17.1	148	2.50	3.78E-5	0.0405
				145	1.75	2.76	
				151	1.75	2.54	
				156	1.00	1.36	
				164	0.50	6.16E-6	
				194	0.20	1.76	
				226	0.10	6.49E-7	
				147	2.60	3.99E-5	
				145	1.50	2.36E-5	
				142	1.00	1.64	
				137	0.50	8.83E-6	
				122	0.20	4.45	
				100	0.10	3.31	
				79	0.05	2.65	
				63	0.03	2.50	
				143	1.00	1.62E-5	
				137	0.50	8.83E-6	
				123	0.20	4.38	
				104	0.10	3.06	
				83	0.05	2.40	
				65	0.03	2.35	
40	1.35	0.079	8.84	145	2.10	3.31E-5	0.0483
				143	1.50	2.43	
				150	1.50	2.21	
				154	1.00	1.40	
				163	0.50	6.24E-6	
				189	0.20	1.86	
				225	0.10	6.54E-7	
				146	2.20	3.42	
				142	1.00	1.64	
				136	0.50	8.96E-6	
				121	0.20	4.53	
				102	0.10	3.18	
				81	0.05	2.52	
				62	0.03	2.59	
40	1.70	0.079	11.2	145	1.50	2.35E-5	
				142	1.00	1.64	
				137	0.50	8.83E-6	
				122	0.20	4.45	
				100	0.10	3.31	
				79	0.05	2.65	
				63	0.03	2.50	

Figure 113. Response of Blade with Slip at Platform

SECTION VI

CONCLUSIONS

The analytical and experimental investigations described in this report have shown that the apparent modal damping in a simple dovetail blade can be predicted on the basis of assumed gross slip at the blade root-disc interface, provided that the exciting force exceeds a certain threshold amplitude. For driving forces below this level, the damping arises from other sources such as hysteresis in the blade material or non-slip interaction at the blade root-disc interface. The investigation has been restricted to a relatively simple problem, and much more effort is needed if one is to design and build blades which are optimized with respect to slip damping at high rotation speeds. However, the basic analytical techniques and physical modelization remain the same.

It has also been shown that a specific configuration of compressor or turbine blade root geometry, in which part of the root contacts the disk only at high rotational speeds, can provide high levels of slip damping, provided that the relevant stiffnesses are properly selected. The analysis can provide the basis for preliminary design investigations, but laboratory and spin pit testing will be necessary to establish the accuracy of the approach and to develop the specific configurations most appropriate for practical application. The changes in blade geometry needed to optimize this type of damping do not represent very large departures from current practice, nor need they represent any weight increases over current blades.

Apart from experimental and spin pit testing, a logical follow on effort would investigate the effects of finite disk compliance, and hence of multiple blade systems, on the dynamic behavior. However, one would expect high levels of slip damping to still be attainable. It is hoped that this report will stimulate or encourage such investigations, since the need for high damping in rotating blades is becoming ever more urgent.

REFERENCES

1. L. E. Goodman and J. H. Klumpp, "Analysis of Slip Damping with Reference to Turbine-Blade Vibration", J. Appl, Mechanics, pp. 421-629, 1956.

2. J. P. Hanson, A. J. Meyer, and S. S. Manson, "A Method of Evaluating Loose-Blade Mounting as a Means of Suppressing Turbine and Compressor Blade Vibration", Proc. S.E.S.A., Vol. 10, No. 2, p. 103, 1958.

3. E. J. Williams and S. W. E. Earles, "Optimization of the Response of Frictionally Damped Beam Type Structures with Reference to Gas Turbine Compressor Blading", J. Eng. for Industry, Trans. A.S.M.E., Paper No. 73-DET-108, 1973.

4. S. S. Manson, "Stress Investigation in Gas Turbine Discs and Blades", SAE Quarterly Trans., Vol. 3, No. 2, p. 229, 1969.

5. R. C. F. Dye and T. A. Henry, "Vibration Amplitudes of Compressor Blades Resulting from Scatter in Blade Natural Frequencies", J. Eng. for Power, July 1969.

6. V. P. Ivanov, "Nekotorie voprosy kolebanyi lopatochnikh ventozov i drugikh uprugikh tel obladajushchikh cikli-checkoi simetriel (Vibration Problems of Blade Discs and Other Elastic Bodies Having Cyclic Symmetry)", Sbornik Statici No. 6, Moskva 1971.

7. V. O. Bauer, "Vliania rastroiki chastot lopatok na resonan-snyie kolebania (Influence of Mistuning of Blade Frequency on Resonant Vibrations)", Cbornik Statici, 6, Moskva, 1971.

8. P. O. Shimov, "Issledovania vliania dinamicheskoi niednoro-dnosti koltzevoi reshotki na resonansynie kolebania ieio profilei (Analysis of the Influence of Dynamic Inhomogeneity of the Ring Net on Resonant Vibration of its Profile)", Sbornik Statici, 6, 1971.

9. D. S. Whitehead, "Effect of Mistuning on the Vibration of Turbomachine Blades Induced by Wakes", J. Mech. Eng. Sci., V. S., No. 1, 1966.

10. A. L. Eshleman, Jr., and J. D. Van Dyke, Jr., "A Rational Method of Analysis by Matrix Methods of Acoustically Loaded Structure for Prediction of Sonic Fatigue Strength", in Acoustical Fatigue in Aerospace Structures, p. 723, eds. W. J. Trapp and D. M. Forney, Jr., Syracuse University Press, New York, 1965.

11. R. L. Bielawa, "An Analytic Study of the Energy Dissipation of Turbomachinery Bladed-Disc Assemblies Due to Intershroud Rubbing", Trans. ASME, J. Mech. Design, ASME paper No. 77-DET-73, 1977.

REFERENCES (CONTINUED)

12. A. V. Srinivasan (ed.), Structural Dynamic Aspects of Bladed Disk Assemblies, ASME Publication, papers presented at Winter Annual Meeting, New York, December 1976.

13. M. P. Hanson, "Vibration Damper for Axial-Flow Compressor Blading," Proc. S.E.S.A., Vol. XIV, No. 1, 1955.

14. S. B. Chubb, "Evaluation of Wire Lacing for the Control of Gas Turbine Blade Vibration," ASME Paper 67-VIBR-47, presented at ASME Vibration Conference, Boston, March 1967.

15. D. I. G. Jones and A. Muszyńska, "Effect of Slip on Response of a Vibrating Compressor Blade," presented at ASME Gas Turbine Conference, Atlanta, Georgia, November 1977 (ASME Paper No. 77-WA/GT-3).

16. D. I. G. Jones and A. Muszyńska, "Harmonic Response of a Damped Two-Degree of Freedom System with Gaps," Nonlinear Vibration Problems - Zagadnienia Drgan Nieliniowych, Vol. 19, Warszawa, 1978.

17. D. I. G. Jones and A. Muszyńska, "Vibration of a Compressor Blade with Slip at the Root," Shock and Vibration Bulletin, 48, 1978, U. S. Naval Research Laboratory.

18. D. I. G. Jones and A. Muszyńska, "Nonlinear Modelization of Non-Conservative Blade Vibration Response," Proc. ICNO Conference on Non-linear Oscillations, Prague, Czechoslovakia, September 1978.

19. J. S. Rao, Turbine Blading Excitation and Vibration," J. Sound and Vibration, Vol. 9, No. 3, pp. 15-22, 1977.

20. D. J. Ewins, "An Experimental Investigation of the Forced Vibration of Bladed Discs Due to Aerodynamic Excitation," in Structural Dynamic Aspects of Bladed Disk Assemblies, ASME publication of papers presented at ASME Winter Annual Meeting, New York, December 1976.

21. R. B. Kolb, "Measured Vibratory Motions of Turbine Blades," ASME Paper 67-VIBR-66, presented at ASME Vibrations Conference, Boston, March 1967.

22. B. A. Squires, "Forces on Blades in a Rotor Stage when the Air Flow Is Distorted," Rolls Royce Internal Report, MCR 90157, 1969.

REFERENCES (CONCLUDED)

23. T. J. Barber and H. D. Weingold, "Vibratory Forcing Functions Produced by Nonuniform Cascades," J. Eng. for Power, Trans. ASME, 100 (1), pp. 82-88, 1978.

24. J. F. Traexler, "Turbomachinery Vibration," Shock and Vibration Digest, Vol. 9, No. 8, August 1977.

25. R. E. Beckett and K. C. Pan, "Effects of Looseness on Dynamic Behavior," Shock and Vibration Bulletin, 41, Part 6, 1970.